December 2020

Artificial Intelligence for Resilience in Smart Grid Operations

Randeniya Vidanage Iroshani Jayawardene
Clemson University, rjayawa@clemson.edu

Artificial Intelligence for Resilience in Smart Grid Operations

A Dissertation
Presented to
the Graduate School of
Clemson University

In Partial Fulfillment
of the Requirements for the Degree
Doctor of Philosophy
Computer Engineering

by
Iroshani Jayawardene
November 2020

Accepted by:
Dr. G. Kumar Venayagamoorthy, Committee Chair
Dr. Richard R. Brooks
Dr. Kuang-Ching Wang
Dr. Shuangshuang Jin

Abstract

Today, the electric power grid is transforming into a highly interconnected network of advanced technologies, equipment, and controls to enable a smarter grid. The growing complexity of smart grid requires resilient operation and control. Power system resilience is defined as the ability to harden the system against and quickly recover from high-impact, low-frequency events. The introduction of two-way flows of information and electricity in the smart grid raises concerns of cyber-physical attacks. Proliferated penetration of renewable energy sources such as solar photovoltaic (PV) and wind power introduce challenges due to the high variability and uncertainty in generation. Unintentional disruptions and power system component outages have become a threat to real-time power system operations. Recent extreme weather events and natural disasters such as hurricanes, storms, and wildfires demonstrate the importance of resilience in the power system. It is essential to find solutions to overcome these challenges in maintaining resilience in smart grid.

In this dissertation, artificial intelligence (AI) based approaches have been developed to enhance resilience in smart grid. Methods for optimal automatic generation control (AGC) have been developed for multi-area multi-machine power systems. Reliable AI models have been developed for predicting solar irradiance, PV power generation, and power system frequencies. The proposed short-horizon AI prediction models ranging from few seconds to a minute plus, outperform the state-of-art persistence models. The AI prediction models have been applied to provide situational intelligence for power system operations. An enhanced tie-line bias control in a multi-area power system for variable and uncertain environments has been developed with predicted PV power and bus frequencies. A distributed and parallel security-constrained optimal power flow (SCOPF) algorithm has been developed to overcome the challenges in solving SCOPF problem for large power networks. The methods have been developed and tested on an experimental laboratory platform consisting of real-time digital simulators, hardware/software phasor measurement units, and a real-time weather station.

Acknowledgments

I would like to express my sincere gratitude to my advisor Dr. Kumar Venayagamoorthy for the continuous support of my PhD research, for his patience, motivation, and immense knowledge. His guidance helped me in all the time of research and writing of this dissertation.

Besides my advisor, I would like to thank the rest of my dissertation committee: Dr. Richard R. Brooks, Dr. Kuang-Ching Wang, and Dr. Shuangshuang Jin, for their insightful comments and encouragement.

I must also thank the Real-Time Power and Intelligent Systems (RTPIS) Laboratory for providing facilities to carry out this research.

I thank my colleagues for their continuous support and encouragement.

Last but not least, I would like to thank my family: my parents, my sister and brother, and my husband for supporting me spiritually throughout my life.

Table of Contents

List of Tables

List of Figures

Chapter 1

Introduction

1.1 Electricity Infrastructure and Resilience

The electric power system is one of the most critical infrastructures and has become the backbone for many other critical infrastructures such as communication, water and gas distribution, and transportation [15, 16]. The power system is evolving into a smart grid, with the introduction of two-way flows of electricity and information, and many other intelligent technologies. As a developing network of intelligent communications, computing, controls, automations and new technologies with many inter-dependencies, the smart grid is vulnerable to many natural and human risks [17]. The grid operation and control is more challenging in the presence of uncertain and extreme events such natural disasters, unprecedented outages, aging power grids, high proliferation of variable renewable generation, and cyber-attacks [18, 19, 20].

Recent extreme weather events such as hurricanes Irma (2017), the longest blackout recorded in US history hurricane Maria (2017), and hurricane Sandy (2012) have demonstrated the importance of having a resilient power grid. Large wildfires throughout California have destroyed electric infrastructure that causes billions of dollars of damage [21]. The Northeast blackout of 2003 which is recognized as the second most widespread blackout in history, still causes fear for future power grid. The blackout affected about 55 million people [22] due to the inadequate situational awareness. The power grid has become a prime target for cyber-criminals in the last decade, indicating increased recorded cyber-attacks throughout the world [23].

The power grid is evolving with proliferated penetration of renewable energy sources, such as wind and solar photovoltaic (PV) power [24, 25]. According to the solar energy industries association (SEIA), United States have installed 3.6 GW of solar PV capacity in Q1 2020, reaching more than 81 GW of total installed capacity, capable of powering up to 15.7 million homes. During the last decade, solar power has experienced annual average growth rate of 49% [26]. The use of solar PV is rapidly increasing worldwide due to the strong policies, rapidly declining costs, and increasing demand across the private and public sector for clean electricity [27]. However, the uncertainty and variability of solar PV generation pose challenges in maintaining resilience of the power system [28, 29, 30]. Higher penetration levels of PV power in the power system introduce power and frequency fluctuations, causing frequency stability and regulation issues. PV power generation and corresponding system frequency observed during the solar eclipse of August 21st 2017 is shown in Fig. 1.1. A greater flexibility in the system and its control is needed to accommodate supply-side variability and balance generation and load demands. The situation is more challenging under extreme weather conditions.
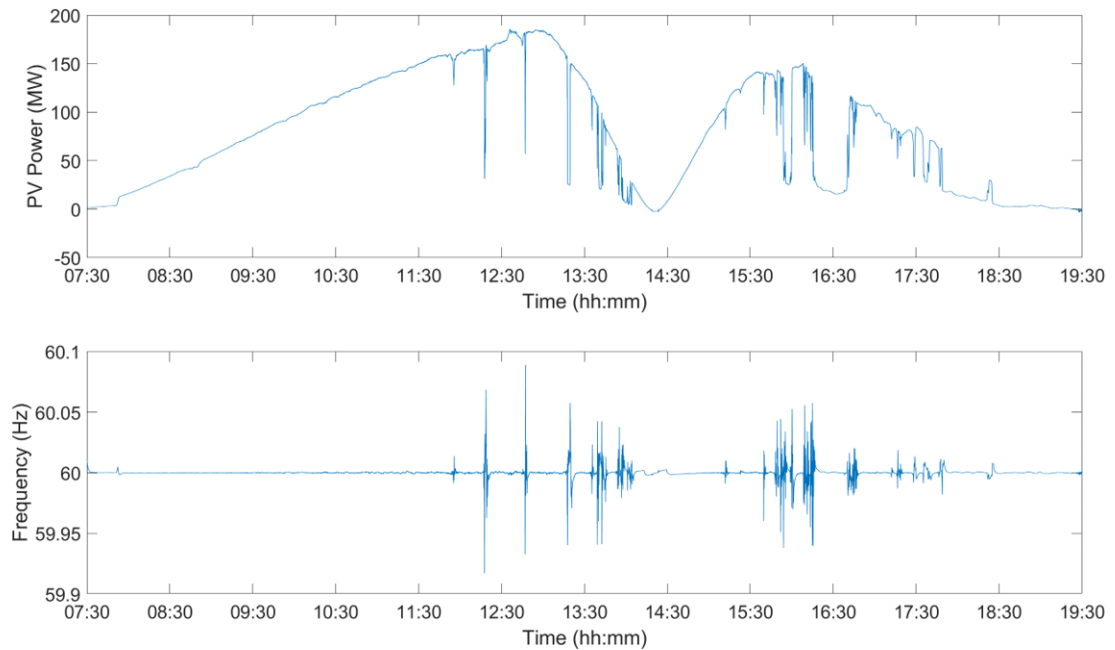
Figure 1.1: PV power generation in a 210 MW plant and frequency in a PV plant integrated Power system observed on the solar eclipse of August 21^{st}2017.

Grid resilience is necessary to allow a continuous and reliable energy supply during abnormal and extreme conditions. The National Infrastructure Advisory Council defines resilience with four dimensions [17]:

- Robustness - the ability to absorb shocks and continue operating;

- Resourcefulness – the ability to skillfully manage a crisis as it unfolds;

- Rapid Recovery – the ability to get services back as quickly as possible;

- Adaptability – the ability to incorporate lessons learned from past events to improve resilience;

Proper control and operation is the key to maintain the resilience in smart grid. Balancing authorities (BAs) maintain the operating conditions of the power system to ensure the balance of electricity supply and demand while managing electric power transfers with other BAs. Additionally, BAs are responsible for maintaining operating conditions under reliability standards issued by the North American Electric Reliability Corporation (NERC) [31, 32]. Today, these goals are achieved through traditional energy management systems (EMSs), which include several applications such as generation and dispatch control (automatic generation control (AGC), generation dispatch, reserve monitoring, load forecasting, load balancing), the economic factors in generation and transmission, and transmission security management (state estimation, security constraint optimal power flow (SCOPF)). The system operators at energy control centers monitor the grid to identify potential problems before a situation becomes critical and maintain the system resilience. However, current EMSs still lack intelligent technologies to manage the challenges introduced by uncertainties and variabilities.

Situational awareness (SA) is an imperative factor in smart grid operation and control. Proper perception of real-time system, comprehension of real-time situation, and projection or prediction of near future states are crucial for SA. The prediction of near future states also known as situational intelligence (SI) is critical for maintaining resilience of the system under abnormal and extreme conditions. An accurate prediction system with adaptability, having faster response times and multiple time scales is required to achieve the SI [13]. Data analytics and artificial intelligence (AI) play a significant role to develop intelligent prediction models and strategies for navigating through variable and uncertain conditions in smart grid operations.
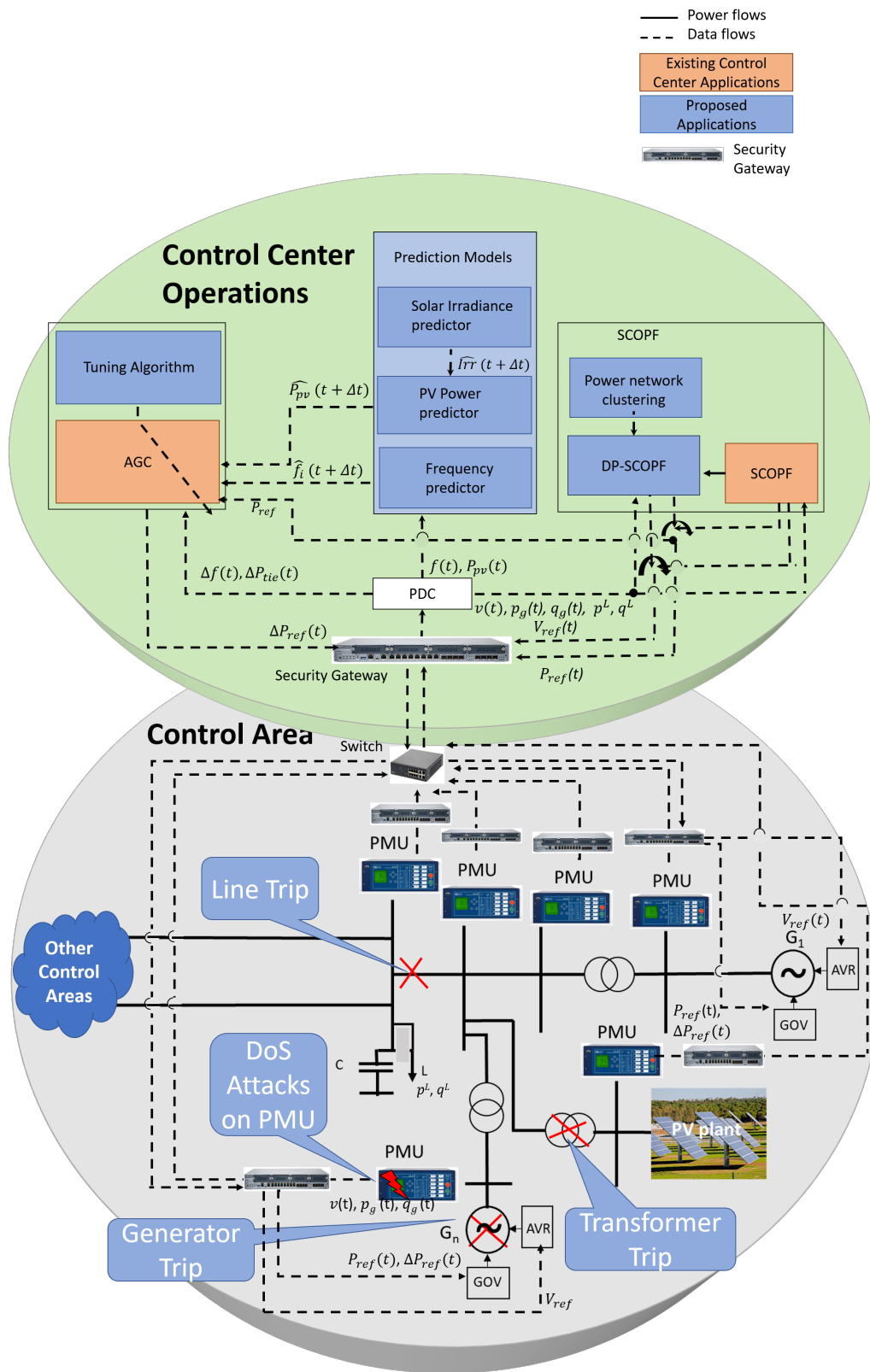
Figure 1.2: Objectives addressed in this dissertation

In this dissertation, the challenges introduced by variable generation, denial of service (DoS) attacks, and unintentional disruptions are addressed for AGC and SCOPF problem with the introduction of SI and/or faster computing approaches. The objectives of this dissertation are illustrated in Fig. 1.2.

1.2 Research Objectives

The goal of this dissertation is to improve smart grid resilience by addressing following objectives.

1.2.1 Optimize AGC operation

According to the reliability standards issued by NERC, frequency in an interconnection needs to be maintained under a standard frequency, typically 60Hz. Frequency depends on the balance between generation and load demand within the interconnection [31, 32]. BAs are interconnected to neighboring BAs via high voltage transmission lines, also known as tie-lines. The control of interchange error, which is the net inflow/outflow compared to scheduled tie-line power flow and the frequency bias, which is the frequency deviation from stabilizing frequency is controlled by AGC within each BA. This is also known as tie-line bias control. The process has become a challenging problem in the presence of variable and uncertain conditions [33]. The performance of the traditional AGC depends on the pre-tuned control parameters. Periodic/adaptive tuning of parameters to manage the high fluctuation of PV power generation can improve the optimal performance of the AGC.

1.2.2 Create situational intelligence for smart grid

Having foresight of PV power generation and power system frequencies can be applied to enhance the resilience of the power system. The state-of-art forecasting methods for predicting solar irradiance and PV power over short time horizons, ranging from few seconds to a minute plus are based on the persistence models, which are incapable of identifying dynamic variabilities of the system. The dynamic behaviour of spatially distributed utility-scale PV plants can be predicted by taking advantage of their neighbourhood information. Similarly, power system frequencies can be predicted by using their network topology.

The deployment of new measurement and metering smart grid technologies generate thousands of terabytes of data, that is rich in system dynamics. Phasor measurement units (PMUs) collect system wide high-resolution electrical measurements. The instantaneous voltage, current, and frequency measurements at specific locations in an electricity transmission system represent the health of the power system. Weather sensors and geographic information systems (GIS) monitor the status of the intermittent renewable energy generation. More accurate and intelligent prediction models can be developed by innovative AI methods from vast amounts of dynamic data.

1.2.3 Integrate situational intelligence to achieve resilient and sustainable power system operations

With PV power and bus frequency predictions included in AGC operations, a resilient and sustainable tie-line bias control can be achieved under uncertain environments, including changing generation, load, and weather conditions.

Although the deployment PMUs and phasor data concentrators (PDCs) enable smooth power system operations overcoming the challenges of variable and uncertain renewable energy [34, 35], the use of PMUs in power system control creates vulnerabilities for cyber-attacks that could jeopardize the power system operations. Delayed or missing measurements from PMUs in real-time power system applications lead to power system frequency instability. Although, the use of virtual private networks (VPNs) eliminate many security vulnerabilities, VPNs are still vulnerable to denial of service (DoS) attacks that exploits side-channels [36]. Application of predicted PMU measurements can mitigate the impact(s) introduced by DoS attacks.

1.2.4 Develop a faster method to solve Security-Constrained Optimal Power Flow Problem (SCOPF)

Minimizing power system operational cost whilst maintaining reliability and quality of power delivery without violating the line and transformer ratings is a challenging task in the presence of variable renewable energy. This has become harder with the increased scale of power systems and requirements of addressing contingencies (loss or failures of the power system components) [37]. Solving the SCOPF problem is an effective tool for online operation and offline planning of power system. The traditional methods of solving SCOPF problem are incapable of addressing

challenges introduced in the smart grid [38, 39]. To overcome this shortcoming the modern parallel and distributed computing power can be utilized. Distributed and parallel properties can be enabled by applying power network clustering methods.

1.3 Contributions

The large amount of data generated in the smart grid can be utilized to analyze the grid behaviour in forms of descriptive analytics (what has happened?), predictive analytics (what could happen?) and perspective analytics (what actions should take?). With the assistance of AI, new approaches have been introduced to extract insights and foresights from data on the electric grid and take automated actions, with the goal of ensuring greater resilience.The contributions of this dissertation are listed as follows:

1.3.1 Optimal AGC for multi-area power systems [1, 2, 3]

Multiple AGC parameter tuning approaches have been studied for AGC operation of multi-area systems. As the first approach, a particle swarm optimization (PSO) based sequential parameter tuning approach is developed. The method is tested on a modified IEEE 68 bus power system with five inter-connected areas under variable load change conditions. Second, a two-step optimization method is developed, where the first step is a global tuning approach and the second step is a local tuning method. The method is tested on a five-area multi-machine power system, which is equipped with two utility-scale PV plants with dynamic PV power generation. Finally, a distributed co-learning tuning approach is implemented with distributed gradient descent (DGD) method and the performance is analyzed on Western Electricity Coordinating Council (WECC)-240 bus system.

1.3.2 Situational intelligence for power system resilience [4, 5, 6, 7, 8]

A short term solar irradiance prediction method is developed for a utilit-scale PV plant using the concept of cellular computational network (CCN). Three PV power prediction models have been developed with the application of solar irradiance, temperature and PV power data. The methods include, reservoir computing networks (echo state network (ESN) and extreme learning machine (ELM)), adaptive neuro-fuzzy systems (ANFIS). The method performance were compared with each other and it was found that the ESN prediction model can provide the best enhanced

prediction results for very short term PV power predictions. A virtual synchrophasor network (VSN) based on a cellular computational echo state network (CCESN) and a cellular computational extreme learning machine (ELM) has been developed to predict power system bus frequencies. The VSN provides resiliency to the physical synchrophasor network. These models are adaptable to uncertain and variable conditions, capable of predicting multiple time steps ahead in real-time and more accurate compared to persistence models.

1.3.3 Resilient and sustainable tie-line bias control for a power system in uncertain environments [9, 10]

With PV power and frequency predictions included in AGC operations, a resilient and sustainable tie-line bias control is achievable under uncertain environments, including changing generation, load and weather conditions. The VSN based on CCESN can mitigate the impact(s) of denial of service attacks (DoS) on physical synchrophasor network.

1.3.4 A distributed and parallel approach based on clustering for Security-Constrained Optimal Power Flow (SCOPF) problem [11, 12]

A robust power network clustering method for SCOPF is developed. The method creates clusters with highly connected power system buses and few boundary branches as possible to assure less complexity and less computational time. The distributed and parallel SCOPF (DP-SCOPF) method provides more accurate solutions during normal and contingency operations. The DP-SCOPF method is capable of providing solutions for online and offline operations on real-world power systems.

1.4   Summary

Extreme weather events, natural disasters, cyber-physical attacks and outages introduce challenges in power system resilience. Moreover, increased integration of variable generation introduces uncertainties and variabilities in the grid, which effects the resilience of the grid. In this dissertation, the challenges introduced by variable generation, denial of service (DoS) attacks, and contingency operations are addressed by providing enhanced methods for AGC and SCOPF problem.

AI based approaches including evolutionary computing, neural networks, fuzzy systems and graph theory based clustering have been applied with the benefit of large PMU and weather data and parallel and distributed computing capabilities. The studies and results presented in this dissertation demonstrate improved resilience in smart grid operations.

Chapter 2

Optimal Automatic Generation Control (AGC)

2.1 Introduction

The power system frequency deviates from its nominal value if the power grid encounters a change in generation and/or load [40, 41]. High penetration levels of renewable energy sources introduces variability and uncertainty in the grid, which causes system frequency and power flow fluctuations. If frequency oscillations are not damped out quickly, the stability and efficiency of the power system is detrimental to subsequent shedding and generator trips [42]. To avoid these situations, optimally designed automatic generation control (AGC) is required.

AGC plays a vital role in power system control centers, maintaining desired system frequency and tie-line power interchange in control areas [42]. AGC minimizes area control error (ACE) of the control area, by providing control signals to the generators in the system. According to the reliability standards issued by the North American Electric Reliability Cooperation (NERC), the North American power grid needs to maintain the system frequency at 60 Hz to ensure grid stability [31]. It is important to have a optimal multi-area AGC system in maintaining resiliency and reliability of large-scale power systems with distributed energy sources and variable generation.
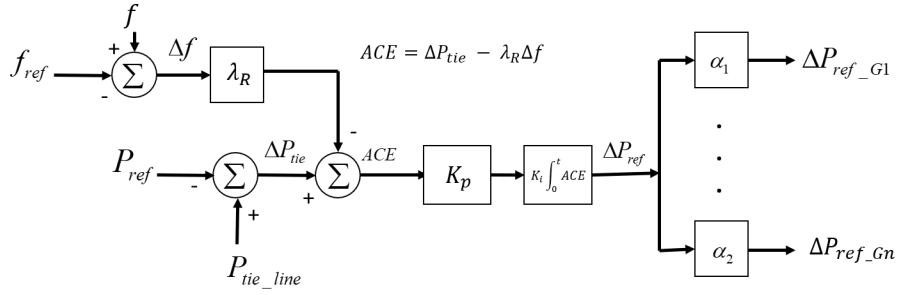
Figure 2.1: AGC Diagram

2.2 Automatic Generation Control (AGC)

In a multi-area power system, AGC performs tie-line bias control, which regulates both area frequency f_i and net power interchange ΔP_{tie}. Area control error (ACE), which is a linear combination of frequency deviation Δf_i and tie-line power deviation ΔP_{tie} is minimized by the AGC to perform tie-line bias control. ACE is defined in (2.1). A diagram of AGC is given in Fig. 2.1.

$$ACE_i = \Delta P_{tie,i} - \lambda_R \Delta f_i \tag{2.1}$$

where λ_R is the balancing authority's bias factor measured in MW/0.1Hz [31].

A proper AGC parameter tuning approach is required in obtaining initial AGC parameters, where the AGC performance (tie-line bias control between areas) depends on the pre-tuned AGC parameters. Conventional PI controller tuning methods include Ziegler Nichols' trial, reaction curve methods, frequency domain methods and multi-objective optimization methods [43]. Although these methods are widely used as the classical control techniques, the proper tuning of multi-area AGCs in the presence of variable generation is difficult with such methods [44]. Recently, new solutions have been introduced to improve the multi-area AGC performance. These solutions include, a fractional-order proportional integral derivative (FOPID) method, a sliding control method and a H_2/H_∞ method [45, 46]. These methods restructure the grid control topology in achieving better performance, which is both economically and timely expensive [2].

However, the identification of optimal parameter combinations for AGC is a challenging task for multi-area power systems in the presence of uncertain and variable conditions. When the power system is interconnected and with more penetration levels of renewable energy, the optimization of one area can lead to degrade the performance of other area. In this study, three tuning approaches

are studied and their performance, advantages and disadvantages are discussed in detail.

2.3 Sequential Tuning with Particle Swarm Optimization (PSO)

2.3.1 Particle Swarm Optimization (PSO)

PSO is a swarm based optimization algorithm, which is an an evolutionary computing algorithm [47]. The method is developed based on the social behavior of birds flocking. The basic idea behind the PSO is that N number of particles traverse through a d dimensional parameter space searching for an optimal solution to a function. Each particle is a potential solution, which is given a random velocity in traversing through the problem space. The particles have memory, which keep track of the previous best position and the corresponding fitness value. In each iteration, each particle moves through the space by updating its' velocity using a combination of its current position, previous best position and the position of the neighborhood's best particle. When a particle obtains an optimal solution, it attracts the other particles in the swarm towards that position. This process is continued until it reaches the stopping criterion. The velocity update equation for $i^t h$ particle in d dimensional space at the $k + 1^{th}$ iteration is given in (2.2)

$$V_{id}(k+1) = wV_{id}(k) + c_1 rand_1(P_{bestid}(k) - X_{id}(k)) + c_2 rand_2(G_{bestid}(k) - X_{id}(k)) \qquad (2.2)$$

where X_{id} and V_{id} are the position and velocity of the ith particle in a d dimensional space. P_{bestid} and G_{bestid} are the particles' previous best and neighbourhoods' best positions. Initially, particle positions and velocities are randomly generated with predefined upper and lower boundaries. k is the iteration number and w is the inertia weight; c_1 and c_2 are cognition and social acceleration constants; $rand_1$ and $rand_2$ are random values between the range of $[0, 1]$. The new particle position at the $k + 1^{th}$ iteration is updated according to (2.3)

$$X_{id}(k+1) = X_{id}(k) + V_{id}(k+1) \qquad (2.3)$$

2.3.2 PSO based Sequential Tuning Method

The flowchart of the PSO based AGC tuning method is given in Fig. 2.2. The lower and upper bounds for the AGC parameters are summarized in (2.4).

$$0.01 \leq K_p \leq 2.5 \ \ and \ \ 0.01 \leq K_i \leq 0.5 \tag{2.4}$$

The objective function used in PSO is given by (2.5). The objective is to minimize the ACE in each area when the load is changed.

$$\min_{K_{p_i}, K_{i_i} \cdots, K_{p_n}, K_{i_n} \in \mathbb{R}} \ \sum_{i=1}^{n} \sum_{t=t_0}^{\frac{t_1}{\Delta t}} |ACE_i| A_i(t - t_0) \Delta t \tag{2.5}$$

$$A = \begin{bmatrix} 1 & 0.5 & 0.5 & 0.5 & 0.5 \\ 0.5 & 1 & 0.5 & 0.5 & 0.5 \\ 1 & 1 & 1 & 1 & 1 \\ 1 & 1 & 1 & 1 & 1 \\ 1 & 1 & 1 & 1 & 1 \end{bmatrix} \tag{2.6}$$

where i is the Area number, n is the number of areas, t is the time in seconds, Δt is the sampling time step in seconds, $_0$ is the time at which the disturbance occurred, t_1 is the simulation end time and A is the area contribution factor given in (2.6). ACEs are calculated by changing loads in each area. An example curve used in fitness function calculation is displayed in Fig. 2.3.

2.3.3 Multi-Area power system with multiple AGCs - Modified IEEE 68 Bus System

The algorithm is tested on a five-area multi-machine power system with with utility-scale PV plants and a synchrophasor-based monitoring system. The power system is described in detail in this section.

The five-area power system model include three types of conventional generators and two utility-scale PV plants. A diagram of the power system is given in Fig. 2.4. The system is a modification model of the IEEE New England (NE)–New York (NY) power systems [48]. The NE grid is named as Area 1, consists of generators G1-G9. the NY grid is named as Area 2, consists
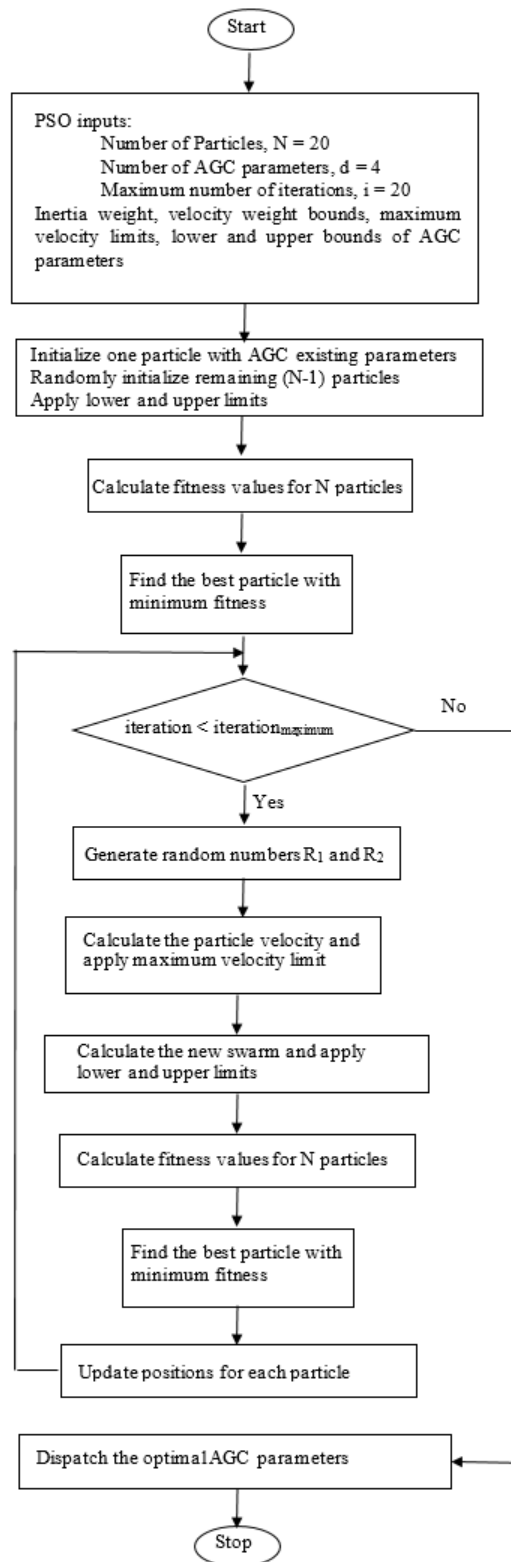
Figure 2.2: Flow chart for the PSO based sequential AGC parameter tuning method

14
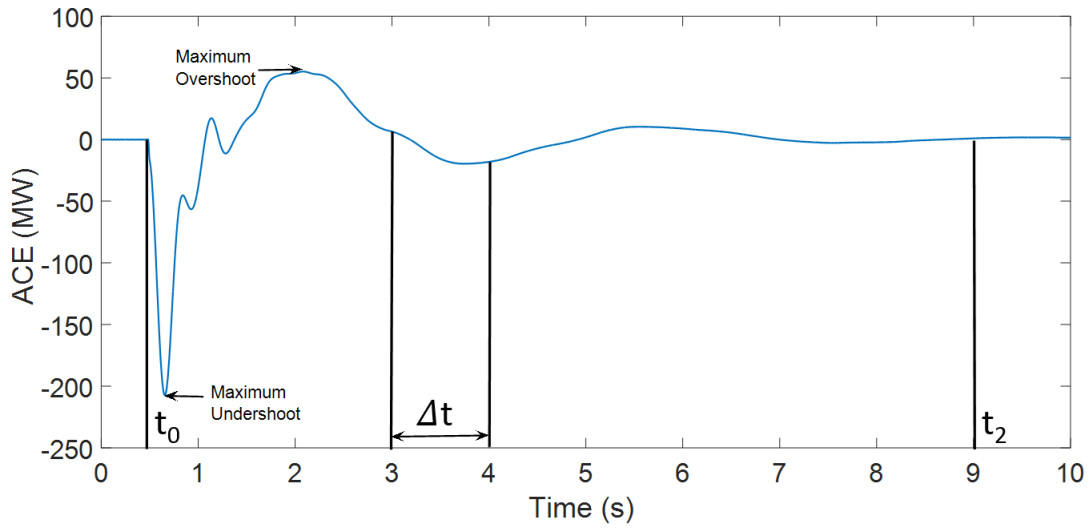
Figure 2.3: An example curve used in fitness value calculation
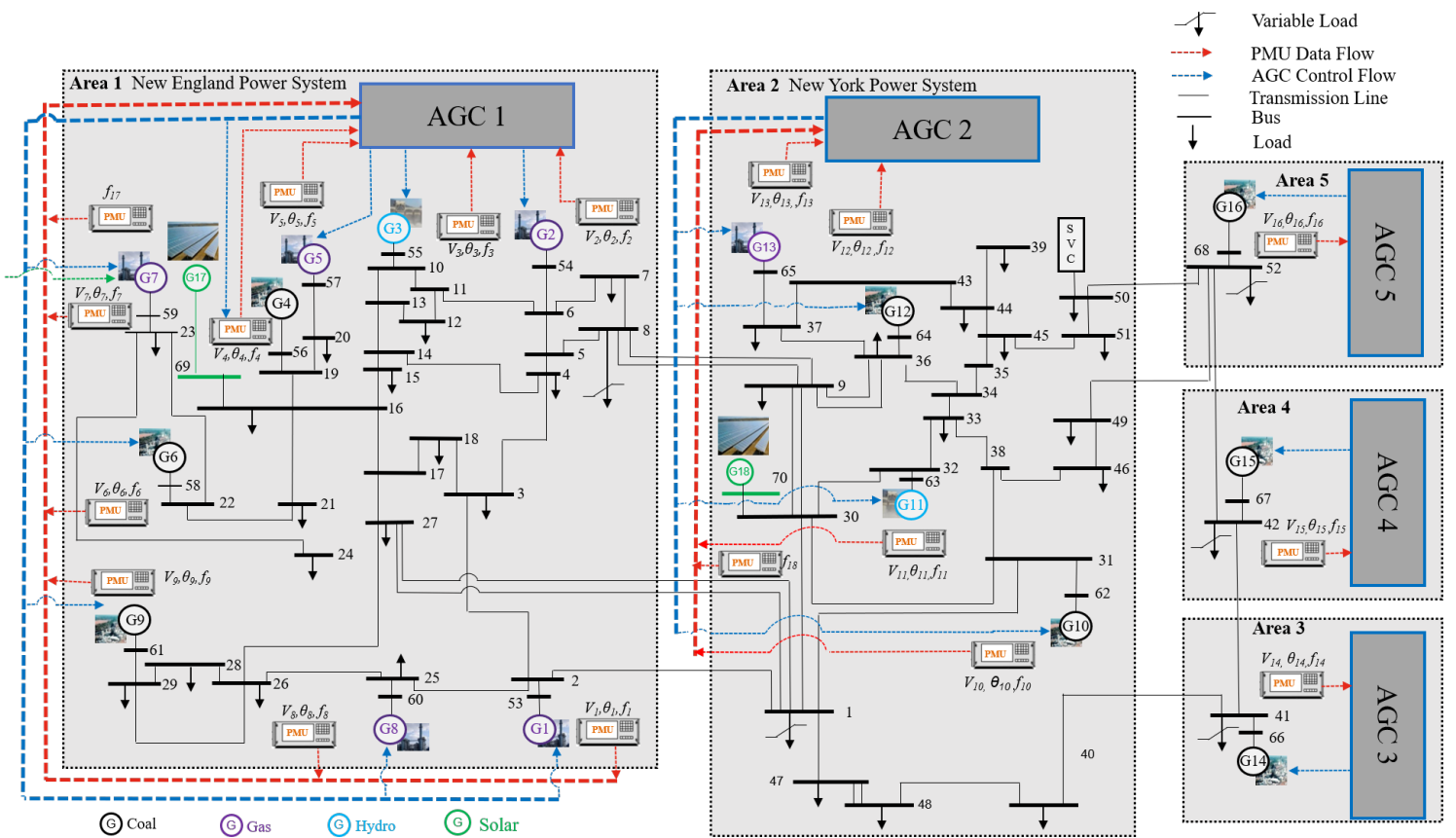
Figure 2.4: Multi-Area power system with multiple AGCs - Modified IEEE 68 Bus System

of generators G10 to G13. Other than Areas 1 and 2, Areas 3–5 are aggregated systems including generators G14 to G16. Two utility-scale PV plants are integrated to the NE and NY components of the system as given in Fig. 2.4. Synchronous generators, automatic voltage regulators (AVRs), power system stabilizers (PSSs) and speed governors are included for all units. Phasor measurement units (PMUs) are equipped at all generator terminal Buses for measuring frequency. Moreover, PMUs are installed at all interconnection Buses for measuring tie-line power flows. All PMU parameters are configured uniformly based on the U.S. standard: 30 frame/sec sampling rate.

During the tuning process, the load at the tie-line Bus 8 is increased in obtaining fitness value for the AGC-1. Similarly, the load at the tie-line Bus 1 is changed for the AGC-2, the load at the tie-line Bus 42 is changed for the AGC-3 and the load at the tie-line Bus 52 is changed for the AGC-4 and AGC-5. The load-increasing amount is set to 200 MW in all five areas.

2.3.4   Results and Discussion

As described above, the AGC tuning is processed sequentially. The order of processing includes six stages, as listed below. The following order is selected based on the ascending order of area priorities.

- Stage 1 – All five AGCs are in initial stage.

- Stage 2 – AGC-5 tuning is completed.

- Stage 3 – AGC-5 and AGC-4 tuning is completed.

- Stage 4 – AGC-5, AGC-4 and AGC-3 tuning is completed.

- Stage 5 – AGC-5, AGC-4, AGC-3 and AGC-2 tuning is completed.

- Stage 6 – All five AGCs tuning is completed.

AGC responses obtained during stages 1-6 for Area-1 and 2 are given in Figs. 2.5 and 2.6. Responses observed for Areas-3, 4 and 5 are given in Fig. A.1, A.2 and A.3. ACEs obtained for initial and all five stages of PSO tuned parameters are compared. It is observed that all five AGCs have improved their performance from the initial stage (Stage 1) to the final stage (Stage 6).

Obtaining optimized AGCs for all five areas is a challenging task with the connectivity between areas. Maximum overshoot, maximum undershoot and settling times observed at the each

16
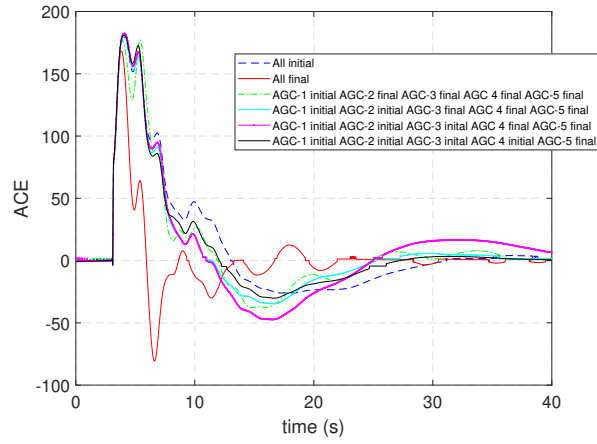
Figure 2.5: AGC-1 response with initial and tuned parameters for 200 MW load increase at the Bus 8 (Area 1).
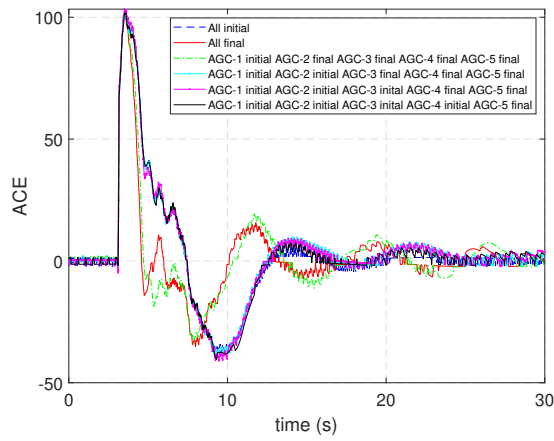
Figure 2.6: AGC-2 response with initial and tuned parameters for 200 MW load increase at the Bus 1 (Area 2).

17

stage of tuning are presented in Table A.1. Few AGCs have obtained their best performance during intermediate tuning stages. For example, AGC-5 obtains its maximum undershoot and settling time at the Stage 2 (only AGC-5 is tuned). AGC-5 performance is degraded at the final stage (Stage 6 – when all five AGCs tuning is completed). Similarly, AGC-4 obtains minimum settling time at the Stage 2; AGC-3 obtains maximum undershoot at the Stage 5 (when AGC-2, AGC-3, AGC-4 and AGC-5 tuning is completed).

As explained above, the AGCs are tuned in descending order of area priorities due to the dependencies between areas. The Area which is tuned during the last step (Stage 6) will have the optimal parameters for that area. Obtained Stage6 (Final) and Stage1 (Initial) AGC parameters are presented in Table.A.2.

Application of a hybrid tuning approach of sequential and global optimization can further improve the performance of AGCs. Therefore, a two-step tuning methods have been studied.

2.4 Two Step Tuning

To improve the performance observed in sequential tuning a two-step tuning approach is studied [2]. During the first step, entire system ACEs are optimized (global optimization) and during the second step local ACEs are optimized. The first step focus on the simultaneous consideration of stability, disturbance tracking, and PV penetration of the system and the second step focus on narrowing of the search space into sub optimal spaces. The approach proved improved results by achieving the system-wide optimal value to satisfy the new emerging challenges of renewable energy source.

Although the method enhances the AGC performance under high penetration levels of variable PV power generation, the method is still inefficient for large interconnected power systems and in distributed operation environments which require minimum information exchanges between operation stations. Moreover, a decentralized concurrent learning method can overcome the performance degradation in consecutive steps observed during the sequential learning process. Therefore, it is necessary to have a cellular cooperative co-learning optimization algorithm, which can optimize all the control areas. A cellular cooperative co-learning is studied to solve the issues identified in this method.

2.5 Cellular Tuning

In this study, the Western Area Coordinating Council (WECC) 240-bus system bus system [49] with four control areas is studied to analyze the motivation to implement a cellular cooperative co-learning tuning algorithm.

2.5.1 Western Electricity Coordinating Council (WECC) 240 Bus System

The 240 bus WECC system developed in national renewable energy laboratory (NREL) given in [50] is used in this study. The system has 291 GWs of total capacity and total IBR capacity of 59 GW, including utility PV, wind and DPV power which compromise 20% of the total capacity. The distribution of PV and wind energy sources throughout the system is visualized in Fig. 2.7.

The system includes 146 generators with an average capacity of 1,800 MW, most of the generators are aggregated with smaller generators of the same fuel type. Each synchronous generator is modeled with a generator model, a turbine-governor model, and an excitation system model. System dynamic models are designed and simulated on PSSE software.

The system is designed with four balancing authority areas, South, California, North and Mexico. A diagram of the connectivity between four areas is given in Fig. 2.8. Four AGCs are implemented in purpose of tie-line bias control. The AGC models used in this study are given in Figs. 2.9 - 2.12. AGCs update ΔP_{tie} and Δf_i every 4s and computes ACEs. Area 1 (South) AGC sends reference signals ($\Delta P_{ref_1 333}$) to generators at bus 1333, which has maximum capacity of 9852 MWs. Area 2 (California) AGC sends reference signals ($\Delta P_{ref_3 933}$) to generators at bus 3933, that has maximum capacity of 7934 MWs. Area 3 (North) AGC sends reference signals ($\Delta P_{ref_4 035}$) to generators at bus 4035 including maximum generation capacity 8448 MWs. Area 4 (Mexico) AGC sends reference signals ($\Delta P_{ref_2 030}$) to generators at bus 2030 that has maximum capacity of 2839 MWs. PV power generation observed with variable weather conditions over one 30 minutes time period is given in Fig. 2.13. Corresponding area frequency deviations, tie-line power flows and ACEs observed are given in Figs. 2.14, 2.15 and 2.16.

2.5.2 Problem Formulation

In this study, it is assumed that the AGC is designed with a proportional-integral (PI) controller (in Fig. 2.1) including two parameters integral gain K_i and proportional gain K_p. PI

19

Figure 2.7: Distribution of renewable energy sources in WECC 240 bus system
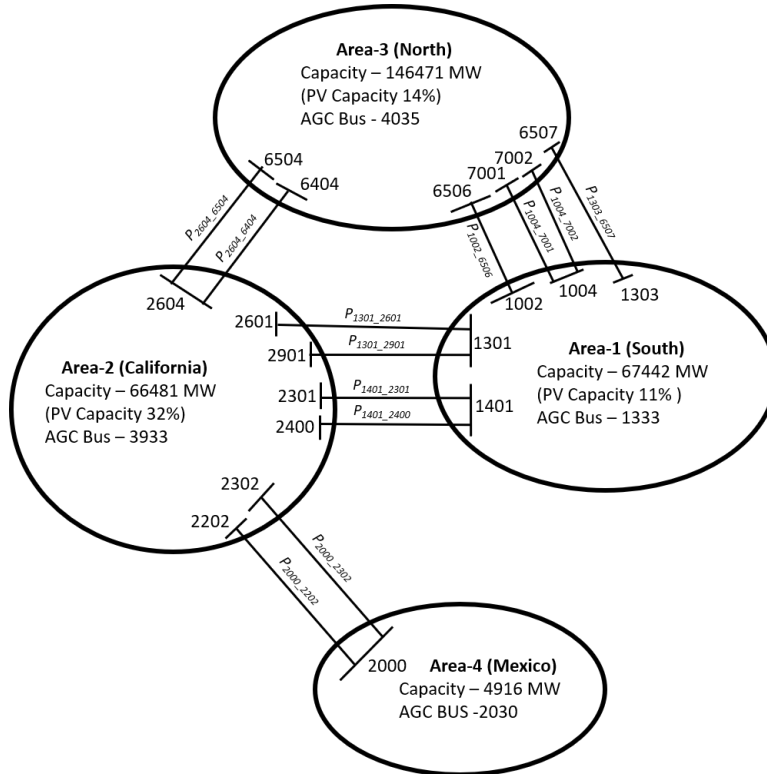
Figure 2.8: Connectivity between four control areas in WECC 240 bus system
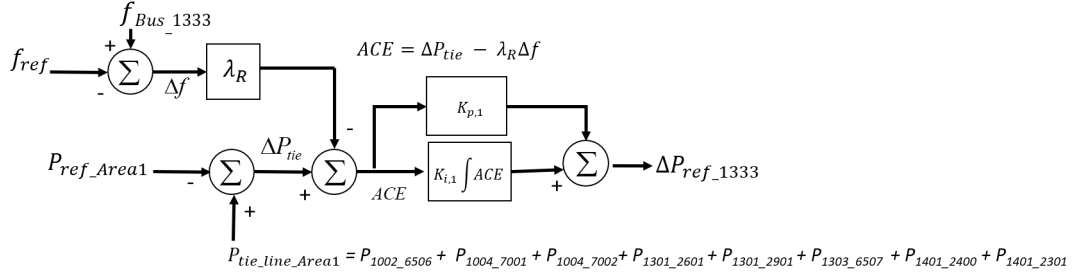
Figure 2.9: Area-1 AGC in WECC 240 bus system

$$P_{tie\_line\_Area1} = P_{1002\_6506} + P_{1004\_7001} + P_{1004\_7002} + P_{1301\_2601} + P_{1301\_2901} + P_{1303\_6507} + P_{1401\_2400} + P_{1401\_2301}$$
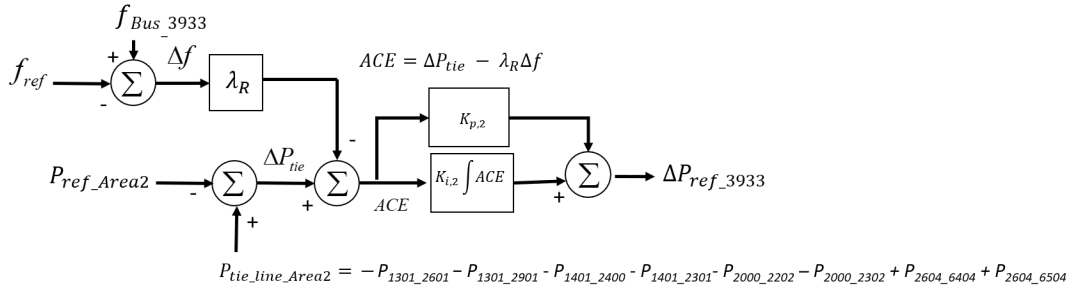
Figure 2.10: Area-2 AGC in WECC 240 bus system

$$P_{tie\_line\_Area2} = -P_{1301\_2601} - P_{1301\_2901} - P_{1401\_2400} - P_{1401\_2301} - P_{2000\_2202} - P_{2000\_2302} + P_{2604\_6404} + P_{2604\_6504}$$
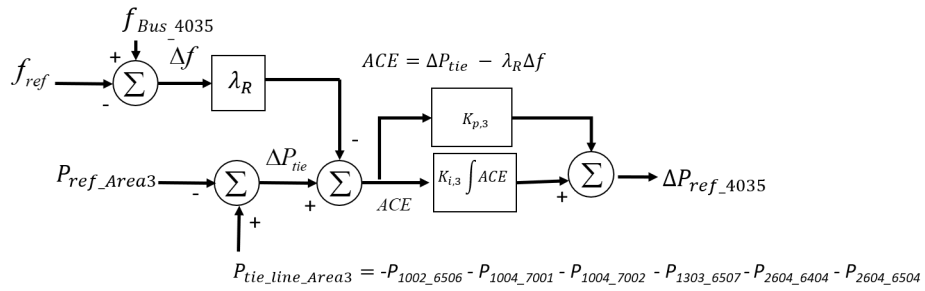
Figure 2.11: Area-3 AGC in WECC 240 bus system

$$P_{tie\_line\_Area3} = -P_{1002\_6506} - P_{1004\_7001} - P_{1004\_7002} - P_{1303\_6507} - P_{2604\_6404} - P_{2604\_6504}$$
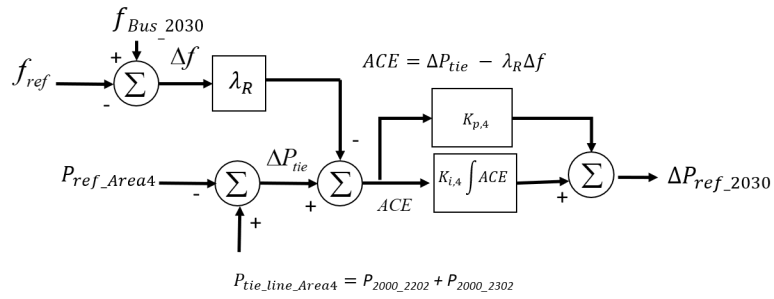
Figure 2.12: Area-4 AGC in WECC 240 bus system
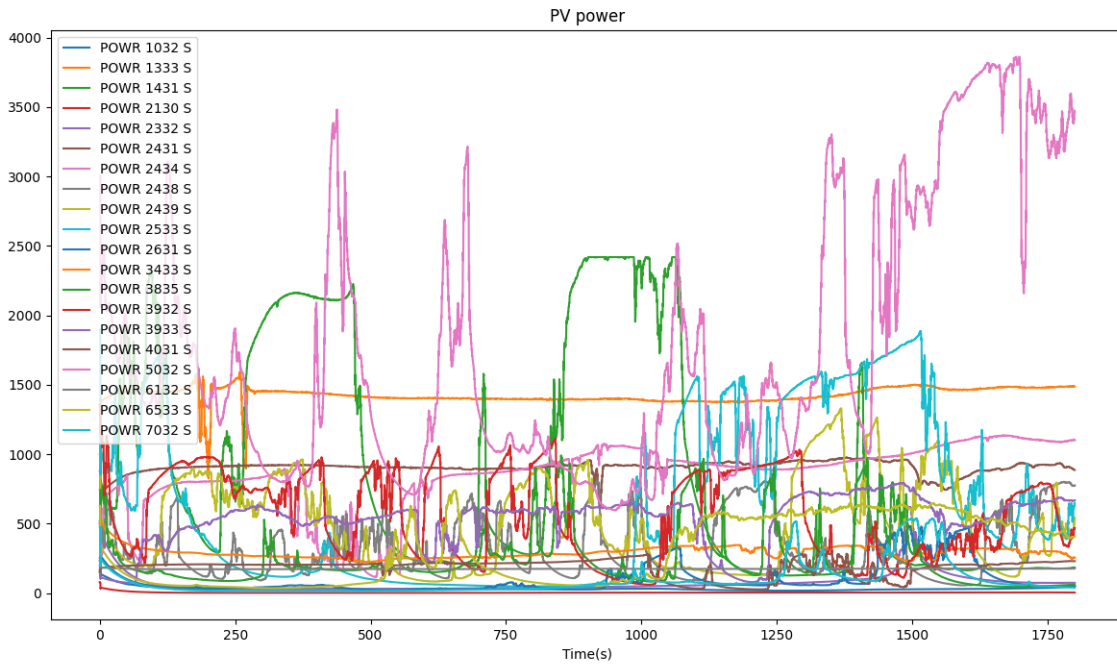
Figure 2.13: PV Power Generation in WECC 240 bus system

22
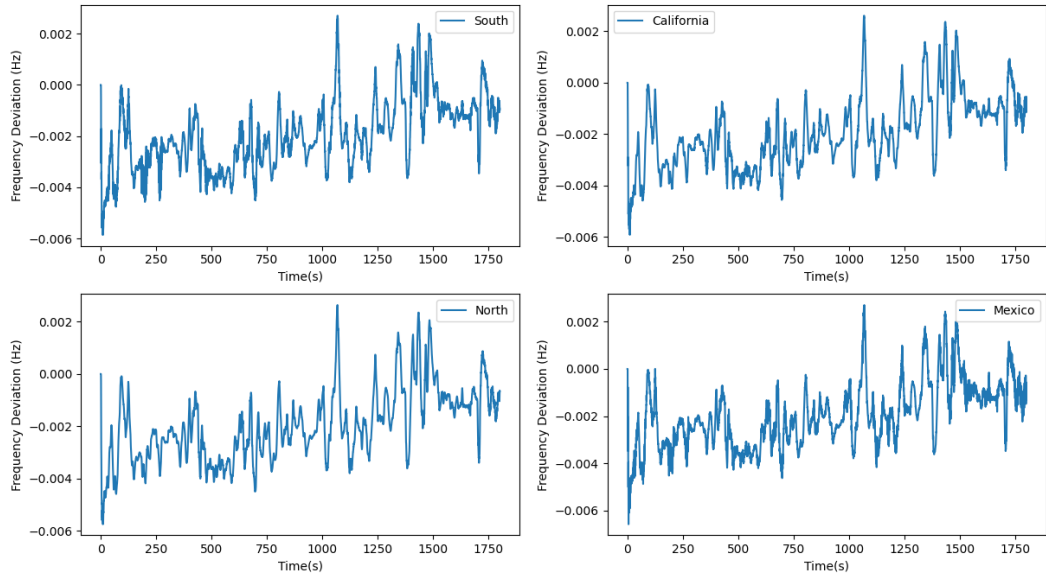
Figure 2.14: Frequency deviations in WECC 240 bus system
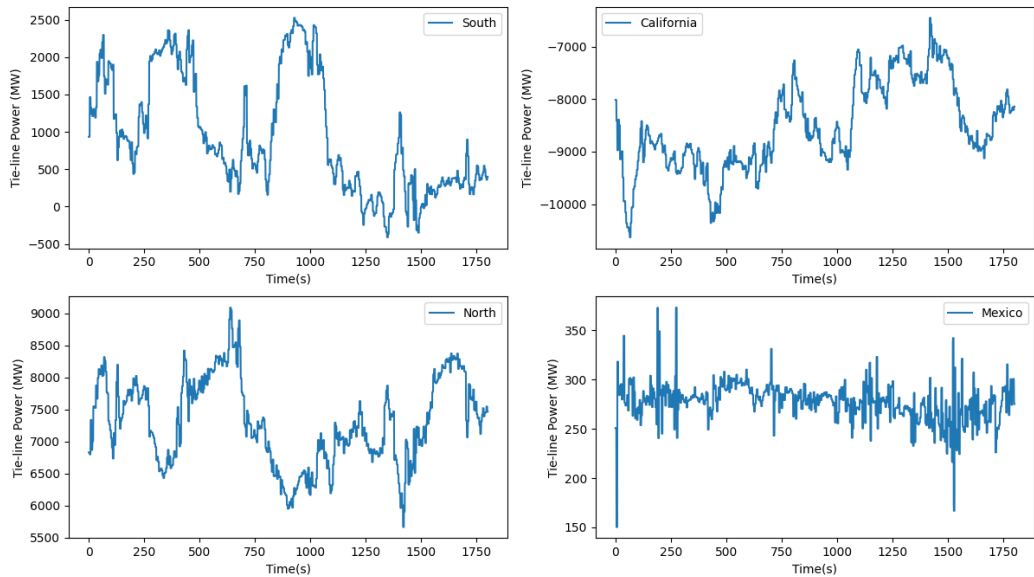
Figure 2.15: Tie-line power flows in WECC 240 bus system
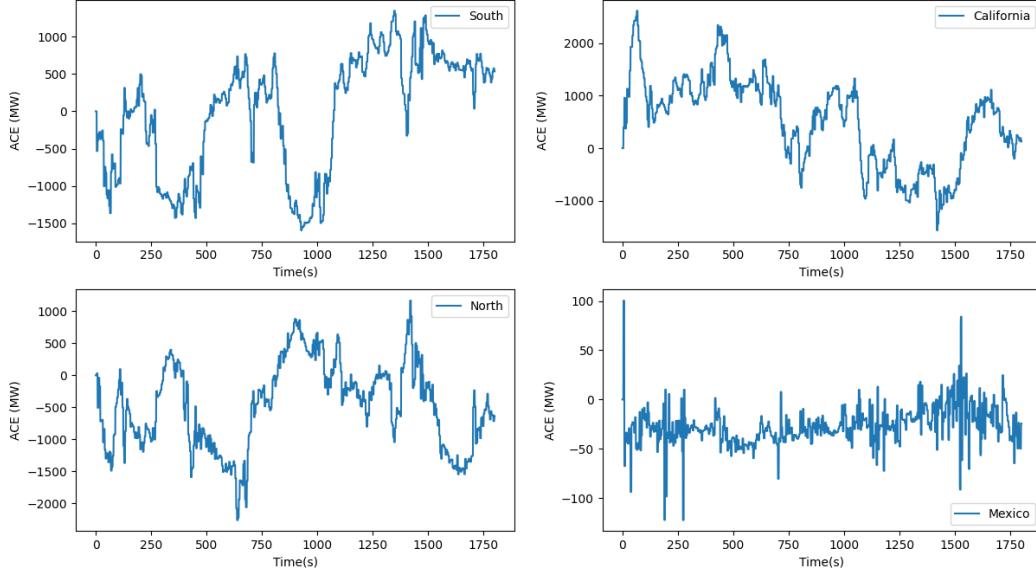
Figure 2.16: Area control errors in WECC 240 bus system

controller based AGC control signal ($u(t)$) is expressed in the time domain t as given in (2.7)

$$u(t) = K_p \cdot ACE(t) + K_i \cdot \int ACE(t)dt \qquad (2.7)$$

Consider a large-scale power system with n balancing areas. A simple diagram of a n interconnected areas is given in Fig. 2.17, where the cost function of each area is a function of AGC parameters (K_i and K_p) in each area.

$$J_i(x_i) = \min_{K_{p_i}, K_{i_i}} \sum_{t=1}^{60} |ACE_i(t)| \;\; s.t \;\; x_i \in (K_{p_i}, K_{i_i}) \qquad (2.8)$$

$$\min_{x \in \mathbb{R}} \sum_{i=1}^{n} J_i(x_i) \qquad (2.9)$$

In this study, the cost function J_i is the ACE_i which is calculated according to (2.8), the area under the curve for 1 minute time period (as given in Fig.2.3). The goal is to minimize the aggregate sum of the costs (ACEs) (given in (2.9)) of the entire system subject to some constraints. Solving (2.9) is a challenging task for multi-area power systems with the high penetration levels of variable

24
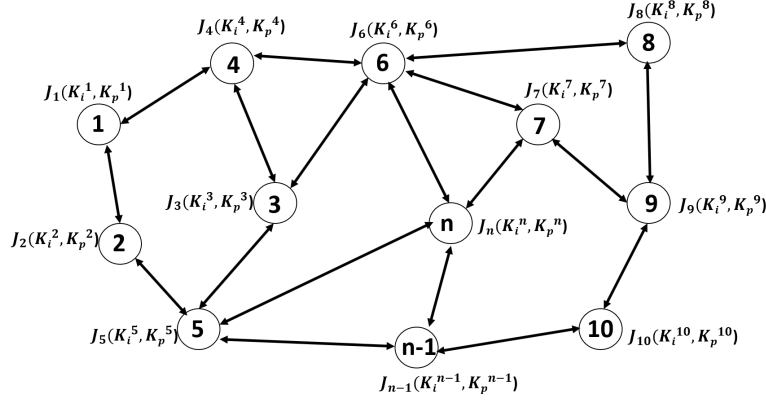
Figure 2.17: A connected network of areas of size n. The cost function of each area is a function of AGC parameters in each area

renewable energy. Local cost function ACE_i can depend on its own AGC parameters and also on the neighbouring area AGC parameters (as observed in Sections 2.3 and 2.4). These dependencies between interconnected areas can contradict the minimization of local cost functions when the problem is solved as a global problem. In other words, minimizing local cost in area n can negatively influence on the local costs in areas 6, 7, 5 and n-1 (in Fig. 3.10) and this can be adversarial on the local costs of their neighbors.

The global cost function minimization and changing ACEs for the WECC 240 bus system are given in Figs. 2.18 - 2.19. Although the ACEs of South and California areas are minimized with the minimization of global cost function, ACEs of the remaining two areas North and Mexico is increasing. Additionally, the minimization of centralized optimization is not practical since the information communication between all the balancing authorities of the power system is not possible. Solving global cost function results handling all the parameters from a single algorithm, which is a complex problem for large scale power systems, where the number of parameters increases exponentially with the size of the power system. This can lead to degraded convergence performance.

This situation motivates to study the problem of parameter tuning of multi-area AGCs in a cellular co-operative co-learning manner, where all the local costs obtain its optimal solution, hence the entire network performance is increased.
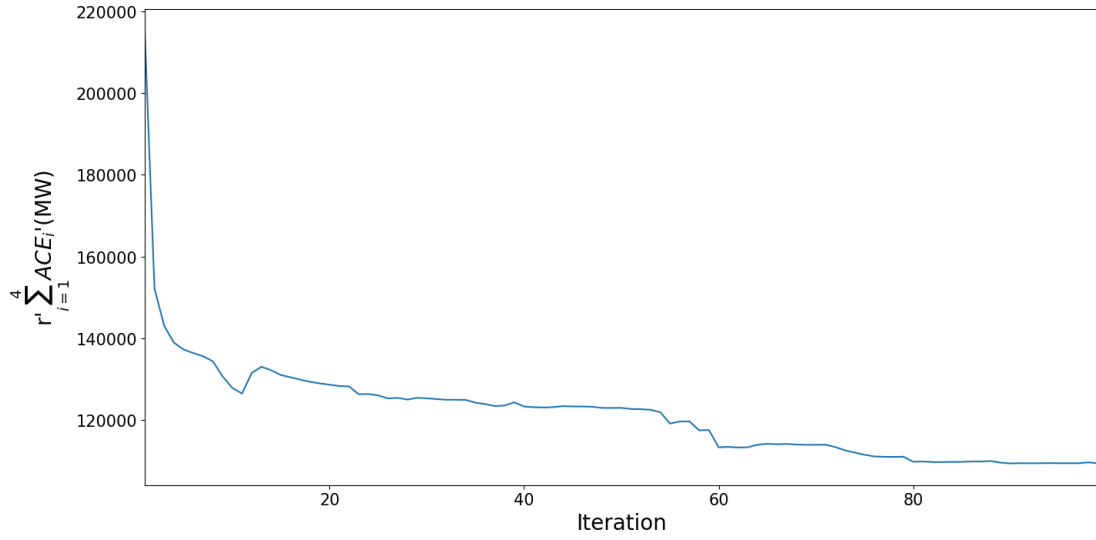
Figure 2.18: Global cost function minimization with iterations
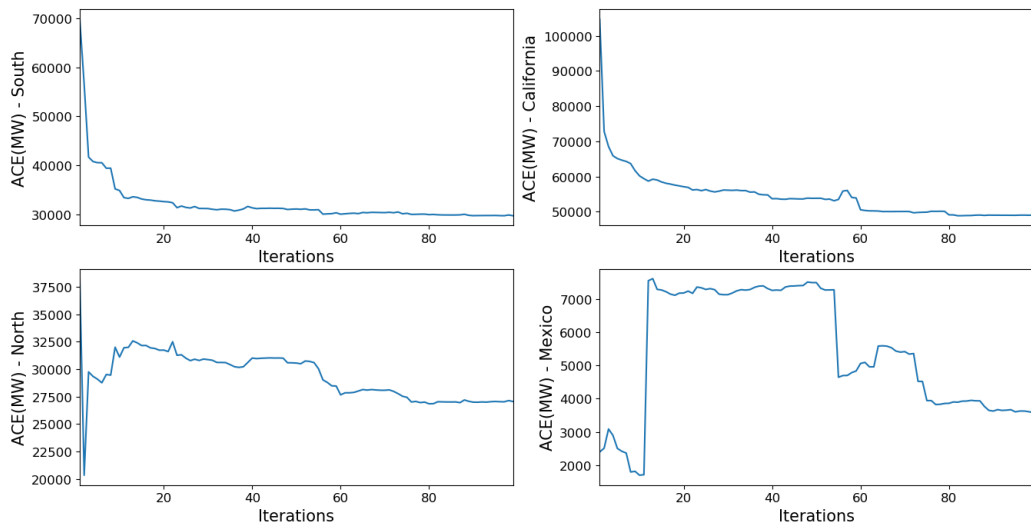
Figure 2.19: Local cost (ACE_i) with the minimization of global cost

2.5.3 Decentralized gradient descent (DGD) based Tuning

The objective is to tune the parameters, K_i and K_p, while optimizing the performance of all four areas under variable generation of PV and wind conditions and other disturbances. In decentralized settings, (2.9) is equivalent to (2.10), where N_i is the set of neighboring areas of area i, x_i is the local copy of x at area i.

$$\min_{x_1,\cdots,x_n \in \mathbb{R}} \sum_{i=1}^{n} J_i(x_i) \ \ s.t \ \ x_i \in [0,1] \ \ x_i = x_j \ \ \forall i,j \in N_i \tag{2.10}$$

The variables x_i are defined within lower and upper bounds ([0, 1]). The constraint $x_i = x_j$ enforces the local copy at each area is equal to those of its neighbors. Each area minimizes its local cost function while ensuring that it's local decision variables are equal to its neighbors local decisions variables [2, 43, 51, 52, 49, 53]. The areas cooperatively communicate with neighboring areas in satisfying this constraint. Problem (2.10) is solved using decentralized gradient decent algorithm (DGD) explained below. The consensus matrix W defined for the WECC 240 bus system is given in (2.11).

$$W = \begin{bmatrix} 0.5 & 0.15 & 0.35 & 0 \\ 0.15 & 0.5 & 0.15 & 0.2 \\ 0.35 & 0.15 & 0.5 & 0 \\ 0 & 0.2 & 0 & 0.8 \end{bmatrix}_{4\times 4} \tag{2.11}$$
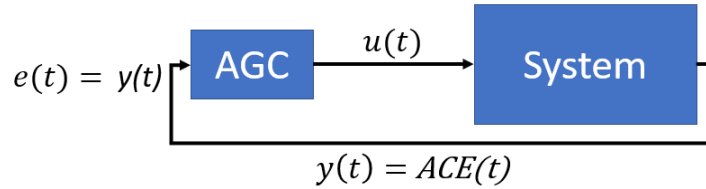
Figure 2.20: AGC function

A diagram of AGC system is given in Fig. 2.20. In this study, ACEs obtained for 1 minute (60 seconds) time period are used for fitness calculation. Here, $y(t)_{1\times 60}$ is the output from the system, which is also the error signal $e(t)_{1\times 60}$ sent into the PI controller based AGC. $e(t)_{1\times 60}$ is a vector of size 1×60. X defines the AGC parameters and $u(t)_{1\times 60}$ is a vector of size 1×60, AGC

27

command output which is sent back to the system to minimize the ACE. Required derivative terms are calculated from [51]. The partial derivatives of the system error with respect to AGC parameters ($\frac{de}{dX}$) are calculated as given in (2.12) - (2.20).

$$e(t)_{1\times60} = |ACE(t)_{1\times60}| \tag{2.12}$$

$$X = [K_p, K_i] \tag{2.13}$$

The partial derivative of the AGC command $u(t)$ with respect to AGC parameters X can be calculated from (2.7), given in (2.14) - (2.15).

$$\frac{du}{dK_p} = |ACE(t)_{1\times60}| \tag{2.14}$$

$$\frac{du}{dK_i} = \int |ACE(t)_{1\times60}|dt = sum\_ACE(t)_{1\times60} \tag{2.15}$$

$|ACE(t)_{1\times60}|$ is a vector of discrete values, therefore the integral is equal to the vector of accumulated sum ($sum\_ACE(t)_{1\times60}$) which is calculated according to (2.16).

$$sum\_ACE(t)[k] = \sum_{j=1}^{k} ACE(t)[j] \quad \forall k = 1, 2, \cdots, 60 \tag{2.16}$$

The partial derivative of the error $e(t)$ with respect to AGC command $u(t)$ is calculated by taking the difference between previous $(t-1)$ and current (t) time step values.

$$\frac{de}{du} = \frac{e(t)_{1\times60} - e(t-1)_{1\times60}}{u(t)_{1\times60} - u(t-1)_{1\times60}} \tag{2.17}$$

Finally, the partial derivative of the system error with respect to AGC parameters ($\frac{de}{dX}$) is calculated as given in (2.18).

$$\frac{de}{dX} = \frac{de}{du} \cdot \frac{du}{dX} \tag{2.18}$$

$$\frac{de}{dK_p} = \frac{de}{du} \cdot |ACE(t)|_{1\times60} \tag{2.19}$$

$$\frac{de}{dK_i} = \frac{de}{du} \cdot sum\_ACE(t)_{1 \times 60} \tag{2.20}$$

Algorithm 1: Decentralized Gradient Decent (DGD)

Initialization;
1. set k=1
2. choose learning rate α
3. choose initial decision variables $x_{1,1}, \cdots, x_{n,1}$
while *termination criteria is met* **do**
  4. calculate partial derivative terms of cost function with respect to decision variables $\frac{dJ_i}{dx_{i,k}}$
  5. update decision variables for $(k+1)^{th}$ iteration
  $x_{i,k+1} = \sum_{i,j \in N_i} W_{ij} x_{j,k} - \alpha \frac{dJ_i}{dx_{i,k}}$
  6. k= k+1
end

The DGD algorithm is given in Algorithm 1. In Algorithm 1, decision variable update step is given in (2.21)

$$x_{i,k+1} = \sum_{i,j \in N_i} W_{ij} x_{j,k} - \alpha \frac{dJ_i}{dx_{i,k}} \tag{2.21}$$

where $W \in \mathbb{R}^{N \times N}$ is the consensus matrix which satisfies following conditions to satisfy the constraint $x_i = x_j$.

- W is doubly stochastic, that is

  $\sum_{i=1}^{n} W_{ij} = \sum_{j=1}^{n} W_{ji} = 1$

- W follows the adjacency matrix of the network topology, where $W_{ij} > 0 \; \forall (i,j)$ in connection between two areas and $Wij = 0$ otherwise.

- W is symmetric.

N_i is the set of neighboring areas of area i All the variables of the optimization are defined within a lower and upper bounds ([0, 1]). Therefore, the decision variable update equation ((2.21)) for four areas is modified with gradient projection based box constrains as given in (2.22), where lb and ub are lower bound and upper bound respectively. Decision variables for each area are listed in Table 2.1.

$$x_{i,k+1} = \max([lb, \min([ub, \sum_{j \in N_i} W_{ij} x_{j,k} - \alpha \frac{dJ_i}{dx_{i,k}}])]) \tag{2.22}$$

Table 2.1: DECISION VARIABLES FOR WECC 240 SYSTEM AREAS

Area	Variables
South	$x_1 = [K_{i,1},\ K_{p,1},\ K_{i,2},\ K_{p,2},\ K_{i,3},\ K_{p,3}\ ]$
California	$x_2 = [\ K_{i,1},\ K_{p,1},\ K_{i,2},\ K_{p,2},\ K_{i,3},\ K_{p,3},\ K_{i,4},\ K_{p,4}\ ]$
North	$x_3 = [\ K_{i,1},\ K_{p,1},\ K_{i,2},\ K_{p,2},\ K_{i,3},\ K_{p,3}\ ]$
Mexico	$x_4 = [\ K_{i,2},\ K_{p,2},\ K_{i,4},\ K_{p,4}]$

2.5.4 Results and Discussion
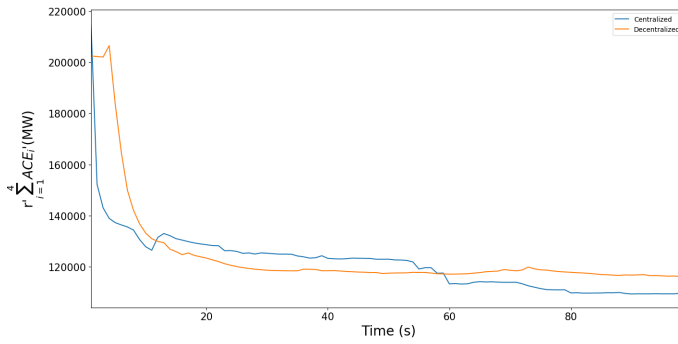
Figure 2.21: Global cost observed with iterations in centralized and decentralized optimization algorithms

As explained in previous sections, local cost function for each area is calculated by (2.8). Global cost observed with iterations in centralized and decentralized optimization algorithms (given in (2.9) and (2.10)) are shown in Fig. 2.21. According to the figure, centralized optimization method has obtained the optimal global cost. However, when the local costs (individual absolute ACEs $j_i(x_i)$ are observed, the centralized approach has improved the areas South and California, but worsen the other two areas North and Mexico.

Decentralized method has improved the local costs of all four areas. Local costs observed

Table 2.2: OPTIMIZED ABSOLUTE SUM OF AREA CONTROL ERRORS WITH VARIABLE GENERATION GIVEN IN FIG. 2.13

Area	$\sum_{i=1}^{1800} |ACE|$		
	Initial	Centralized	Decentralized
South	1216752.59	1158965.28	**852923.48**
California	1508409.37	1314266.22	**1260986.80**
North	1195149.07	1100514.41	**1065754.76**
Mexico	56746.97	45839.34	**44682.71**
$\sum_{i=1}^{4} ACE_i$	3977057.99	3619585.26	**3224347.75**

30
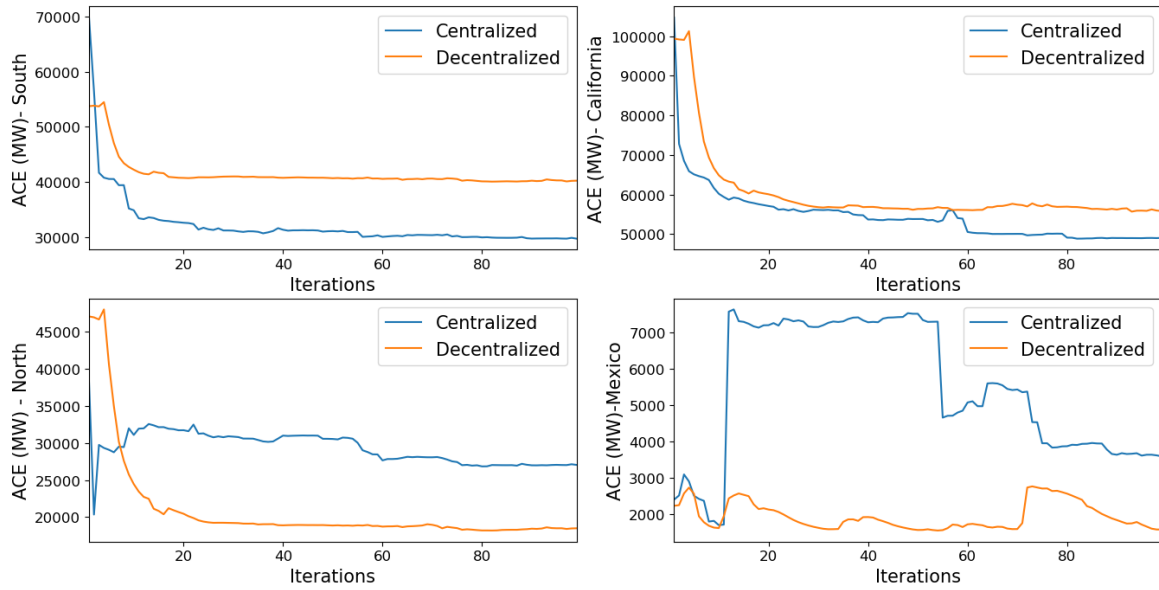
Figure 2.22: Local costs ($|ACE_i|$) observed with iterations in centralized and decentralized optimization algorithms
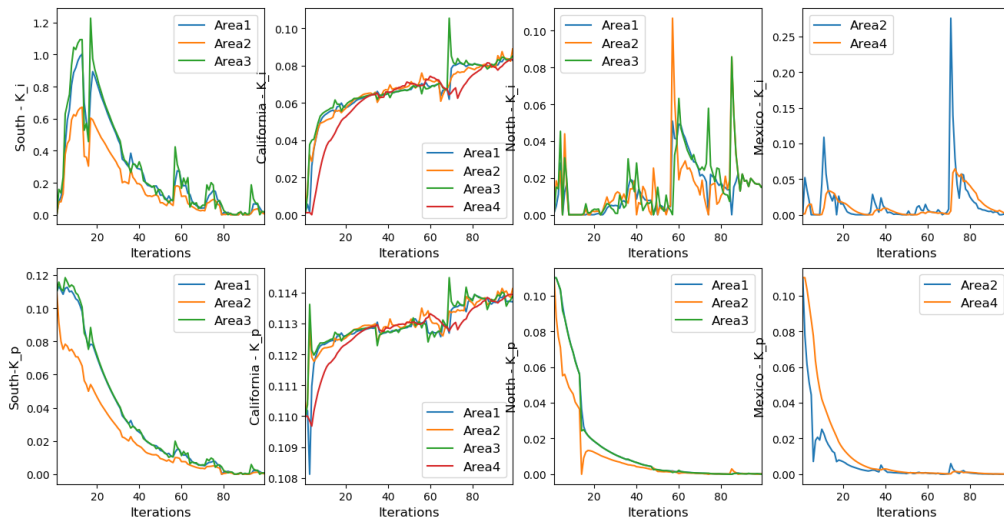
Figure 2.23: Local copy values of decision variables in decentralized gradient decent algorithm
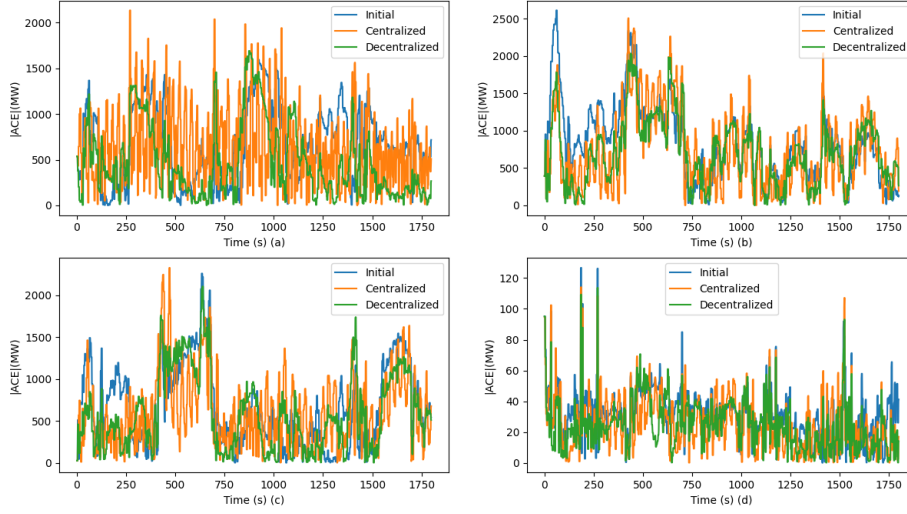
Figure 2.24: Absolute ACEs observed from initial, centralized and decentralized optimization AGC parameters with variable generation given in Fig. 2.13 (a) Area-1, (b) Area-2, (c) Area-3 and (d) Area-4

Table 2.3: OPTIMIZED AREA CONTROL PARAMETERS

Area	Initial		Centralized		Decentralized	
	K_i	K_p	K_i	K_p	K_i	K_p
South	0.001	0.1	0.588031487	0.622380855	0.012848426	0.000530722
California	0.001	0.1	0.748039783	0.289331356	0.082270896	0.113844047
North	0.001	0.1	0.030114677	0.022292356	0.016658888	0.000125401
Mexico	0.001	0.1	0.04224694	0.001535763	0.002612252	0.000173822

32

in centralized and decentralized methods are shown in Fig. 2.22. Absolute ACEs observed during variable PV power generation given in Fig. 2.13 for each area are shown in Fig. 2.24. Corresponding summation of absolute ACEs within this 30 minutes time period (1800 seconds) are given in Table 2.2. The results show improved performance with decentralized optimization method.

In decentralized optimization algorithm, local copies of decision variables must be equal at the end of the optimization process, according to the (2.10) and (2.21). The values of the decision variables with iterations are given in Fig. 2.23. According to the figure, all the local copies of eight parameters have converged. Final AGC parameters observed are tabulated in Table 2.3.

2.6   Summary

Automatic generation control maintains the desired system frequency and scheduled tie-line power flows within balancing authority areas. In this study, proportional-integral (PI) controller based AGC systems are studied for two multi-area power systems. A sequential tuning, two step tuning and a cellular co-operative co-learning AGC parameter tuning methods are studied to obtain the optimal control parameters for entire system. Typical results indicate that cellular co-operative co-learning AGC parameter tuning approach can provide minimal area control errors with improved system performance. AGC performance under uncertain environments can be enhanced by introducing situational intelligence (SI). The proposed methods to obtain SI are described in next section.

Chapter 3

Situational Intelligence for Smart Grid Resilience

3.1 Introduction

Situational awareness (SA) is critical and necessary to control center operators for resilient smart grid operation. Situational awareness systems provide an understanding of the spatial and temporal dynamics of an interconnected and geographical distributed power system [13]. A diagram of the situational awareness in a control center is given in Fig. 3.1. Situational intelligence (SI) is the integration of historical and real-time data to implement near-future situational awareness, which is very important in maintaining resilience in the system. In this study, artificial intelligence based prediction models have been presented to predict short term solar irradiance, photovoltaic power, and bus frequencies.

Cellular computational network is an architecture, that can model complex dynamical systems such as the electric power system. In this study, the capabilities of CCNs are exploited to achieve SI by predicting the near future states of the power system. The prediction models studied include reservoir based neural networks (echo state network , extreme learning machine) and adaptive neuro fuzzy systems. In the following subsections, these architectures are described further.
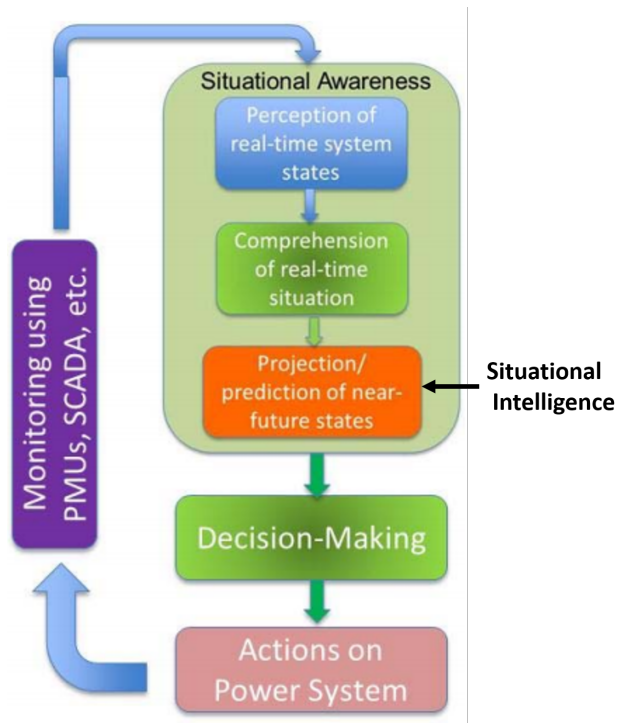
Figure 3.1: Situational Awareness (SA) in a Control Center [13]

3.2 Cellular Computational Network (CCN)

CCN is a distributed scalable architecture for dynamic learning of systems [54]. CCN consists of a collection of cells, which are connected based on the topology of the system. A generic CCN cell consist of a computational unit, learning unit and a communication unit. Theses internal units of a CCN cell is given in Fig. 3.2. The computational unit produces an output based on the information available to the cell. It is implemented based on the requirement of the application. A function approximation or different neural network paradigms are more suitable to implement the computational unit. The learning unit allows a cell to learn by experience in which the computational units performance is improved with time (adaptation). The learning can be attained though supervised, unsupervised or through reinforcement learning approaches. Finally, the communication unit interacts with the neighboring or interconnected cells and utilizes that information in the computational process. This allows each cell to be updated about the surrounding components and use the information to determine it's own output. Communication unit and component measurements create dynamic input-output data into a cell.
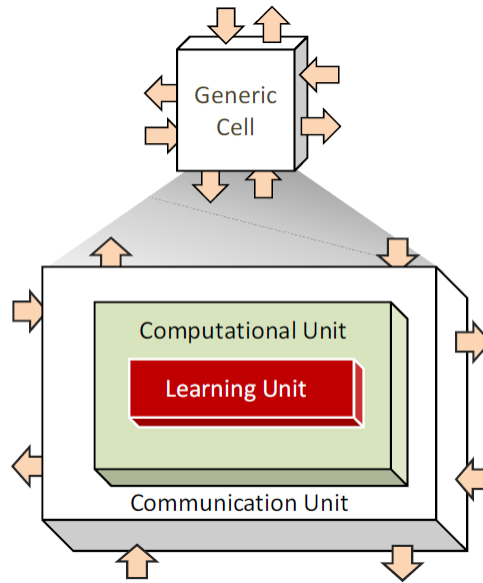
Figure 3.2: Internal units of a CCN cell [14].

3.2.0.1 Computational Unit

The computational unit selection should be done to suit the application. It uses an intelligent algorithm to utilize the available input data to give a final output. For example, selection of a neural networks architecture for the computational unit can be done considering the dynamics of the system modeled. A recurrent neural network (RNN) architecture would be better for a system with inputs that have temporal dynamics. An MLP feed-forward neural network would be a better fit for a system with less temporal dynamics. Variants of CCN include, MLP[55] , ELMAN [56], ELM [8], generalized neuron [57], ESN [7],etc.

3.2.0.2 Learning Unit

The learning unit includes learning and adaptation. The learning process of the cells can be executed concurrently while synchronizing with time (synchronous) or the learning process of individual cells can be independent (asynchronous). Asynchronous structure can be used in applications where cells have different frequency outputs. The learning and adaptation method varies based on the computational unit of a cell. CCN learning methods include, back-propagation, particle swarm optimization(PSO), cooperative PSO, etc.
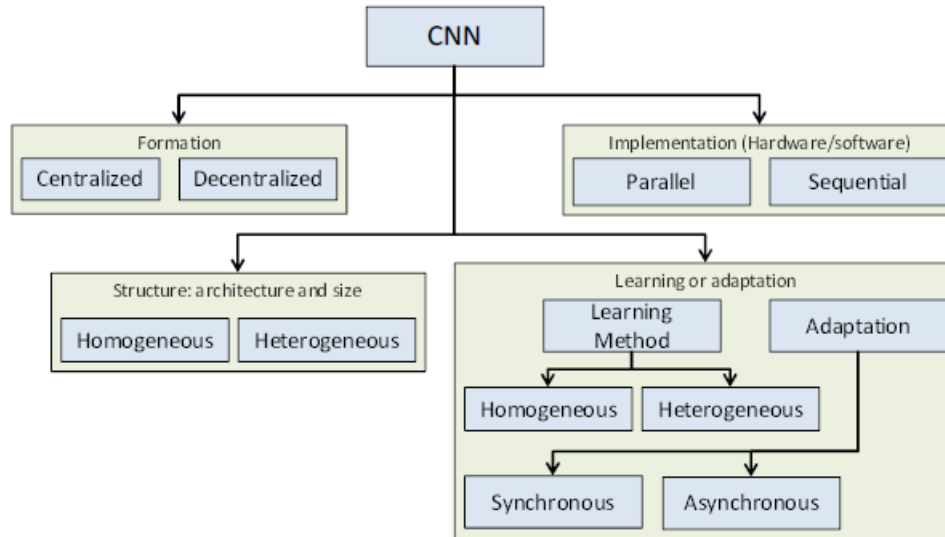
Figure 3.3: CCN classification based on the structure [14]

3.2.0.3 Communication Unit

Communication unit defines the relationship between a cell and the remaining cells in the network, which is decided based on the application. In general, communications are defined based on the systems topological design.

3.2.1 CCN Structures

The CCN is categorized into different levels based on its cells internal structure and the implementation criteria. These categorization criteria are illustrated in Fig 3.3.

The CCN can be implemented in various structures. The structure selection is done according to the data flow requirement of the application. CCN structures are categorized as follows:

3.2.1.1 Centralized vs. decentralized

The physical distribution of the cells in CCN could be located at one physical location (centralized) or spatially distributed across multiple physical locations (decentralized). Power system applications are generally decentralized as the system is distributed across a large geographical region.

37

3.2.1.2 Homogeneous vs. heterogeneous

The internal structure of all the cells in the CCN could be identical (Homogenous) or they can have different internal structures (heterogeneous) based on the computational model, learning method, learning unit, etc. If the system have cells with different complexities, a heterogeneous CCN would model the system better.

3.2.1.3 Synchronous vs. asynchronous

The learning process of the cells can be executed concurrently while synchronizing with time (synchronous) or the learning process of individual cells can be independent (asynchronous). Asynchronous structure can be used in applications where cells have different frequency outputs.

3.2.1.4 Sequential vs. parallel

The CCN can be implemented in a sequential platform or in a parallel platform, by providing parallelism among the cells. The speed of the computation can be enhanced if the implementation is done in parallel.

3.2.2 Application of graph theory in CCN

Let $G = (V, E)$ denote a directed graph with set of vertices $V = [1, \ldots, N]$ and set of edges $E \subset V \times V$. A directed edge from vertex i to j is denoted by $(i, j) \in E$. A directed graph is undirected if and only if $(i, j) \in E$ implies $(j, i) \in E$. Let $A = [a_{ij}] \in \mathbb{R}^{(N \times N)}$ be the adjacency matrix associated with the graph G, where $a_{ij} \geq 0$ is the weight of edge $(j, i) \in E$ and $a_{ij} = 0$ otherwise. For a undirected graph G , the degree $D = [d_i] \in N$ of vertex $i \in V$ is the number of edges $(i, j) \in E$ that are incident to the vertex i. Two types of degrees are defined for directed graphs which are in degree and out degree based on the direction of the edge incident to vertex i [58].

In CCN, the connectivity between cells is decided based on the topology of the system. The CCN can be represented in form of different network typologies, such as grid, ring, mesh, star, line, tree or fully connected. However, this selection of topology can be decided based on the graph theory concepts introduced above. For example, if there is a network with large number of nodes and interconnections and a CCN needs to be implemented on top of the network by considering
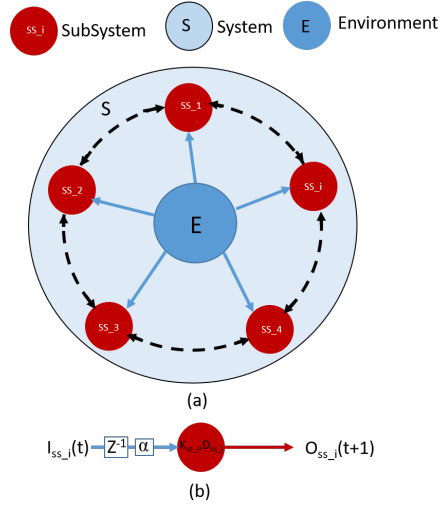
Figure 3.4: A graphical representation of a CCN (a) System of subsystems (b)Single subsystem [14]

most important nodes of the network. In this situation, the nodes with highest degree can be selected as the most important nodes. Similarly if the number of communication links in the CCN needs be limited, then the edges with highest weights (that is strongly connected edges) can be selected. Additionally graph theory centrality measures such as betweenness, closeness, highest eigen vector, highest degree and concepts such as shortest path, hubs, minimum cut, modules, etc can be considered when deciding the best topology for the CCN application.

Consider a generic graphical representation of a CCN given in Fig. 3.4. The graph includes a system of interconnected subsystems/nodes (SS_i). The output (O_{ss_i}) of SS_i node is connected to N neighboring nodes. The output can be represented in mathematical form as given in (3.19).

$$O_{ss\_i}(t+1) = f(\alpha_i O_{ss\_i}(t), \alpha_1 O_{ss\_i}(t), \cdots, \alpha_N O_{ss\_N}(t), K_{ss\_i}, D_{ss\_i}) \qquad (3.1)$$

where α is the discount factor associated with each subsystem. For any subsystem, the discount factor affects the extent of influence of its own past experience $O_{ss\_i}(t)$ and the knowledge of its neighbors $O_{ss\_i}(t), \cdots, O_{ss\_N}(t)$ in its output $O_{ss\_i}(t+1)$. The output of each subsystem also be governed by other static and dynamic parameters associated with the subsystem, which are represented in K_{ss_i}, D_{ss_i}. This is also known as a learning of learning systems (LOLS).
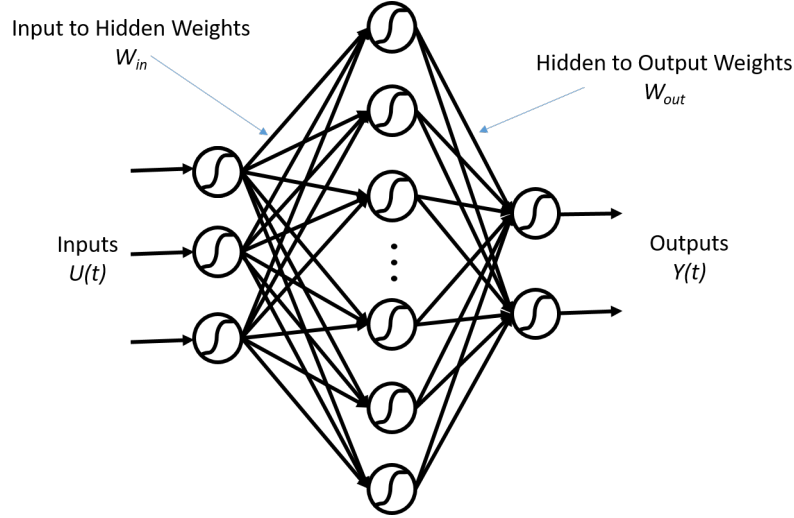
Figure 3.5: An ELM Architecture.

3.3 Extreme Learning Machine (ELM)

ELM is a type of single layer FFNN [5, 4]. A diagram of an ELM architecture is given in Fig. 3.5. ELM is based on the concept of reservoir computing, an extended framework of neural networks. In reservoir computing input signals are fed into a fixed random network of reservoir which can map the inputs to a higher dimensional space [59]. The reservoir is the hidden layer of the single perception FFNN, which is fixed during the learning process. Therefore, input to hidden weights W_{in} are randomly initialized and kept fixed and only the readout weights (hidden to output weights) W_{out} are trained [60]. The hidden to output weights are learned with simple approaches such as linear regression, which provides faster learning. This provides a solution to challenges in training traditional FFNNs, conventional FFNN learning process is slow, which requires iterative learning as explained under FFNNs section. ELM is capable of providing good generalization performance with high learning speed, more suitable for analyzing big data. Thus, ESN is a highly used regression approach among smart grid big data analytics community.

The hidden layer (reservoir) of ELM is calculated according to (3.2).

$$H = \begin{bmatrix} g(W_{in_1} \times U(1) + b_1) & \dots & g(W_{in_N} \times U(1) + b_N) \\ \vdots & \ddots & \vdots \\ g(W_{in_n} \times U(n) + b_1) & \dots & g(W_{in_N} \times U(n) + b_N) \end{bmatrix} \tag{3.2}$$

where W_{in_1} is the input to hidden weight with i^{th} hidden layer node, b_i is the bias to the ith node, $U(i)$ is the ith input set, n is the learning data size, N is the number of hidden layer nodes and $g(.)$ is the hidden layer activation function. After calculation of hidden layer matrix H, hidden to output weights W_{out} can be calculated using offline or online learning approaches.

Simplest approach of learning ELM is simple linear regression with pseudo-inverse method. Where W_{out} is calculated as given below in (3.3).

$$W_{out} = pinv(H) \times T \tag{3.3}$$

where T is the desired output and $pinv$ is the pseudo inverse function. Here the output layer is treated with a linear activation function. The reservoir matrix should be considerably large in obtaining best performance.

Dynamic learning of variable patterns require online sequential learning algorithm over a batch-learning algorithm, as most of the smart grid data require dynamic learning with time and current time step output is depending on time-delayed predicted values. In [61] a fast, accurate sequential learning algorithm for single layer feed-forward network is presented. The algorithm is referred as online sequential extreme learning machine (OS-ELM), which originates from basic ELM batch learning method explained previously. This method is capable of learning the network using data as one-by-one or chunk-by-chunk.

3.3.0.1 Online Sequential-ELM (OS-ELM)

The OS-ELM algorithm includes of two phases, initialization and sequential learning. Consider n arbitrary distinct input and target samples $U(i), T(i)$ activation function g and N number of hidden nodes. n_0 is the initial input and target sample size where $n_0 \leq N$

- Initialize the learning phase.

    - Randomly assign input weights W_{in}^0 and bias b.

    - Calculate the initial hidden layer matrix H_0 using (3.19).

    - Calculate the initial output weights W_{out}^0 using (3.2).

- Sequential learning phase

41

- Now consider the $t+1^{th}$ input-target sample of data, where n_{t+1} is the sample size. Here, $n_{t+1} \leq 1$.

- Calculate the partial hidden layer matrix H_{t+1} of size $(n_{t+1} \times N)$ using (3.19).

- Calculate W_{out}^{t+1} as follows.

$$P_{(t+1)} = P_t H_t^T [I + H_{(t+1)} P_t H_{(t+1)}^T]^{(-1)} H_{(t+1)} P_t \tag{3.4}$$

$$W_{out}^{(t+1)} = W_{out}^t + P_t H_{(t+1)}^T [T_{(t+1)} - H_{(t+1)} W_{out}^t] \tag{3.5}$$

- Now set $t = t+1$ and go back to first step of sequential learning while $t \leq n_{t+1}$

  Where

$$P_{(t+1)} = \frac{P_t - (P_t h_{(t+1)} h_{(t+1)}^T P_t)}{(1 + h_{(t+1)}^T P_t h_{(t+1)})} \tag{3.6}$$

$$h_{k+1} = [g(W_{in}^1 U(k+1) + b_1 \cdots g(W_{in}^N U(k+1) + b_N] \tag{3.7}$$

- Output is calculated as below.

$$Y(t) = H \times W_{out} \tag{3.8}$$

3.4   Echo State Network (ESN)

ESN is a reservoir based RNN which relies on supervised learning method [62]. An architecture of an echo state network is given in Fig. 3.6. $U(t)$, $Y(t)$ and $X(t)$ are the input, output and hidden signals respectively. Similar to ELM, ESN has a large random fixed hidden layer, known as "reservoir". The neurons in the hidden layer has sparse connection weights. The reservoir neurons produce nonlinear responses of the input signals, which are sent through an activation function in obtaining outputs. ESN input to hidden layer weights (W_{in}), hidden to hidden layer weights W and output to hidden layer weights W_{fb} are randomly generated and kept fixed through the entire learning process. Only the hidden to output layer weights W_{out} are learned during the learning process. Therefore, ESN learning is computationally efficient, simple and faster compared to most of
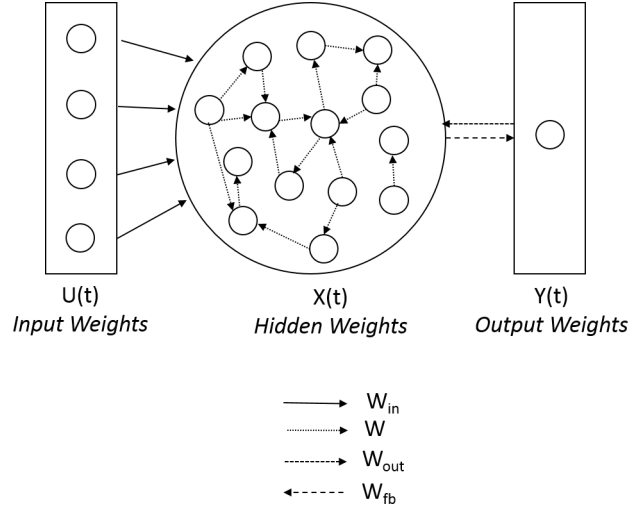
Figure 3.6: An Echo State Network Architecture.

the traditional RNN learning approaches. Thus, ESN are more suitable for handling large amounts of data. ESN can generate more accurate answers for dynamic and non-linear systems such as smart grid operation dynamics, variable renewable generation.

ESN, hidden layer units are updated every time step when an input is fed into the network. The hidden layer update at $(t+1)_{th}$ time-step is determined as expressed in (3.10).

$$X(t+1) = f(W_{in} \times U(t) + W \times X(t) + W_{fb} \times Y(t)) \tag{3.9}$$

where $U(t)$, $X(t)$ and $Y(t)$ are the input, hidden-layer state and output at time t. W is the hidden to hidden weights with W_{ij} is the weight between neurons i and j. W_{in} and W_{fb} are input and feedback weights respectively. f is the activation function. The hidden layer weight is updated with time, which can memorize the dynamics of the system with time. Similar to ELM, ESN has both online and offline learning methods. The simplest approach is linear regression using pseudo inverse function as in (3.3).

It is more suitable to apply an online learning method for maintaining the non-linearity and the dynamic behaviors smart grid data. ESN is conjoined with recursive least squares (RLS) learning algorithm which is a fast online adaptation method, resulting RLS-ESN in [63].

3.4.1 Recursive Least Squares - ESN (RLS-ESN)

RLS-ESN has the capabilities in learning non-linear systems with high convergence rate and low residual error.

ESN hidden layer state is computed according to (3.10). Output is calculated as below.

$$Y(t) = f_{out}(W_{out}[U(t), X(t)]) \tag{3.10}$$

where f_{out} is the output layer activation function.

Similar to basic ESN algorithm, reservoir states are calculated for some time and initial initial "washout" activities are thrown away to maintain the ESN property of the network. After the initial "washout" steps, output weights are updated for each time step as follows,

$$P(t) = \frac{(P(t-1) - [k(t) \times v(t)^T \times P(t-1)])}{\lambda} \tag{3.11}$$

$$W_{out}^t = W_{out}^{(t-1)} + k(t)(Y(t) - T(t)) \tag{3.12}$$

Where $k(t)$ is the innovation vector, $P(t)$ is the covariance matrix initialized with large diagonal values, $v(t)$ is the concatenated matrix for input and hidden unit activation at the t time step, λ is the forgetting factor (≤ 1) and $T(t)$ is the target output at t time step.

The random initialization of weights must satisfy few properties in obtaining better learning performance. The echo state property, which maintains the excitation of reservoir dynamics must be satisfied by the proper selection of parameters such as settling time, spectral radius and input, output scaling parameters [62].

3.5 Adaptive Neuro Fuzzy Inference Systems (ANFIS)

ANFIS is a hybrid system of both NNs and fuzzy systems [6]. ANFIS performs by applying neural network learning to identify and tune the parameters and structure of the Fuzzy inference system (FIS). The ANFISs are easy to implement, have fast and accurate learning ability, have strong generalization abilities and easy to incorporate both linguistic and numeric knowledge for problem solving. In ANFIS, a neural network is designed to implement the fuzzy system, so that the

structure and parameters of the knowledge base are obtained by defining, adapting and optimizing the topology and the parameters of the corresponding neuro-fuzzy network, based on the available data. This include two types of learning methods, structural learning to find fuzzy logic rules and parameter learning to tune fuzzy membership functions and neural network weights. A flow chart of the ANFIS learning process is given in Fig. **??**.

The ANFIS model implemented in this dissertation uses a Takagi-Sugeno type fuzzy inference system which is available in MATLAB fuzzy logic tool box. The parameter learning algorithm uses a hybrid model of the least-squares and back-propagation gradient decent learning methods.

3.6 Accuracy Measures

Accuracies of the predictions are measured using several accuracy measures. Accuracy measures are defined in this section.

3.6.0.1 Absolute Percentage Error (APE)

$$APE = \mid \frac{A_t - P_t}{A_t} \mid \times 100\% \tag{3.13}$$

where A_t and P_t are corresponding actual and predicted outputs.

3.6.0.2 Mean Absolute Percentage Error (MAPE)

$$MAPE = \frac{1}{n} \sum_{t=1}^{n} \mid \frac{A_t - P_t}{A_t} \mid \times 100\% \tag{3.14}$$

where A_t and P_t are corresponding actual and predicted outputs and n is the number of sampled data used for the calculation.

3.6.0.3 Correlation Coefficient

$$\rho = \frac{\sum_{i=1}^{n}(P_t - \bar{P})(A_t - \bar{A})}{\sqrt{\sum_{i=1}^{n}(P_t - \bar{P})^2}\sqrt{\sum_{i=1}^{n}(A_t - \bar{A})^2}} \tag{3.15}$$

where A_t and P_t are corresponding actual and predicted outputs and n is the number of sampled data used for the calculation. $\bar{A}$ and $\bar{P}$ are mean values of actual and predicted output. The importance of CCELMN frequency prediction model is, this is a scalable architecture for adaptive learning of frequency prediction outputs. Results are compared with those obtained with independent ELM models and persistence model and shown to outperform. The CCELMN prediction performance is compared with an independent ELM frequency predictor. These ELMs are implemented to predict the frequency at each Bus, only considering direct PMU data measured at the corresponding Bus. Both the approaches are compared with the persistence model performance. Persistence model, as the name implies is defined as applying current time step value for the next time step value.

3.6.0.4 Standard Deviation (STD)

$$STD = \frac{1}{n-1} \sum_{t=1}^{n} (APE - MAPE)^2 \tag{3.16}$$

3.6.0.5 Root Mean Square Error (RMSE)

$$RSME = \sqrt{\frac{1}{n-1} \sum_{t=1}^{n} (A_t - P_t)^2} \tag{3.17}$$

3.6.0.6 Skill Factor (S)

$$S = (1 - \frac{RSME}{RSME_p}) \times \% \tag{3.18}$$

where $RMSE$ is the prediction model RMSE and $RSME_p$ is the persistence model RMSE.

3.7 Solar Irradiance Predictions

As the traditional electric power grid is modernizing towards the "smart grid", the integration of PV power into the grid has been increasing. It is essential to increase the penetration levels of PV power in the grid, with the requirement of providing sustainable and clean energy. Although PV power provides many advantages, the uncertain and intermittent renewable energy generation introduces challenges in power system operation and control. Uncertain generation introduces power
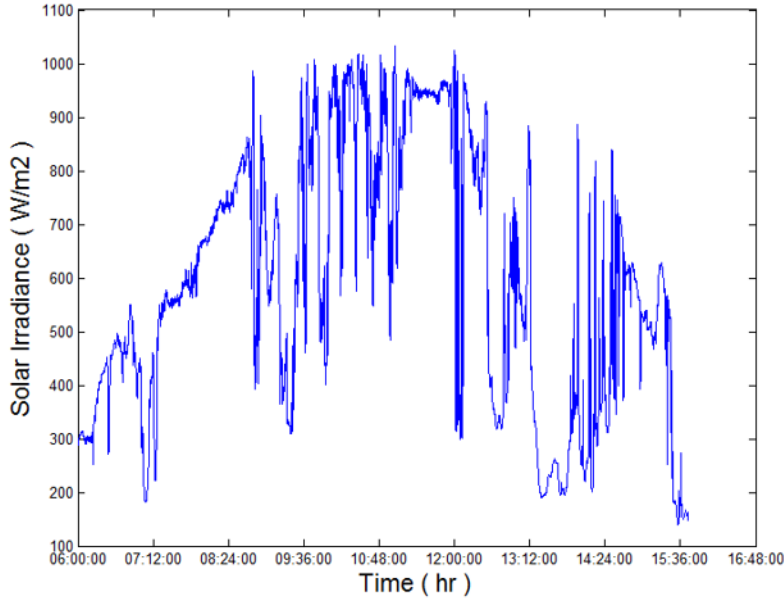
Figure 3.7: Solar irradiance observed on June 5, 2014

and frequency fluctuations in the power grid. Predicting variability of generation in short term intervals has become an interesting area of study, which can provide an insight of variability before it occurs. Predictive analytics can improve the accuracy of the control actions, hence obtain the SI in the power system. PV power generation is highly dependent on the weather changes such as solar irradiance. A variation of solar irradiance and corresponding PV power generation obtained from a 200MW PV plant are given in Figs. 3.7 and 3.8. Predicting solar irradiance can utilize the PV power prediction process.

According to the literature, there are several studies have been done on predicting solar irradiance. The proposed methods for solar irradiance and PV power predictions include artificial neural networks (ANN) [64], [65], auto-regressive (AR) [66], support vector machine (SVM), decision/regression tree [67], moving average (MVA), auto-regressive moving average (ARMA), auto-regressive integrated moving average (ARIMA), ANFIS [68], random forests [69]. However, accurate predictions for very small time steps (1s-15min) is still remains as a challenge.

In this study, spatially distributed location information is utilized to predict the solar irradiance. A diagram of the prediction framework is given in Fig. 3.9. A CCN is implemented on top of the distributed PV plant topology, where each cell is a PV plant. In this study different CCN

47
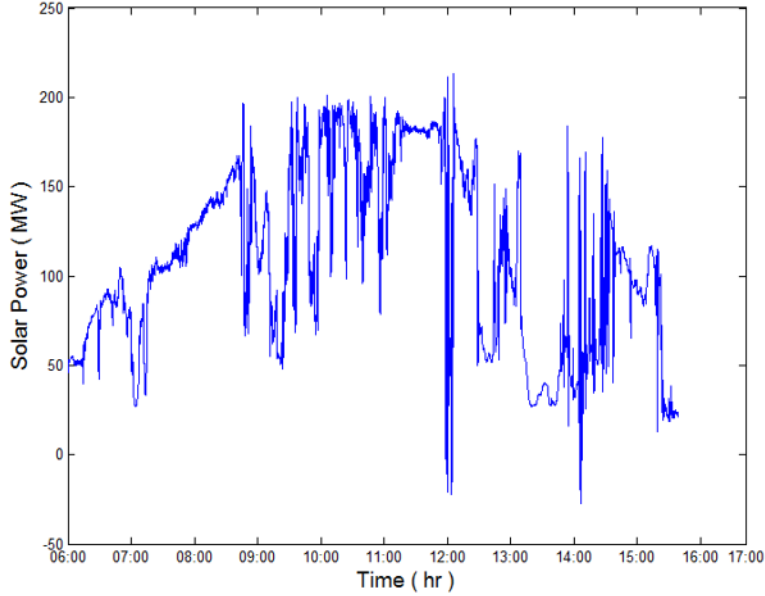
Figure 3.8: PV power observed on June 5, 2014

configurations are studied based on the number of locations and connectivity between locations. CCN cells are implemented using ESN computational units, which are more suitable for dynamic behavior of the solar irradiance.

The framework is tested on data observed from Oahu, Hawaii. Solar irradiance measurements observed at the Oahu solar measurement grid, National Renewable Energy Laboratory (NREL) is used to simulate the distributed PV plants [70]. A satellite map of the measurement grid is shown in Fig. 3.10. Solar irradiance sensor locations are indicated by purple color. Global horizontal solar irradiance data archived from March 2010 - October 2011 are applied for learning and testing CCN.

Three CCN configurations are studied based on the number of cells used. A diagram of the configurations studied are given in Fig. 3.11. The cell configurations are changed from 2, 3 and 4. The prediction output of each cell $(Irr_i(t + \Delta t))$ is a function of the location solar irradiance at time $t, ((Irr_i(t))$, neighboring location's solar irradiance at time $t, (Irr_j(t))$, location predicted solar irradiance at time $t - 1, (\hat{I}rr_i(t - 1 + \Delta t))$ and the neighboring location's predicted solar irradiance

48
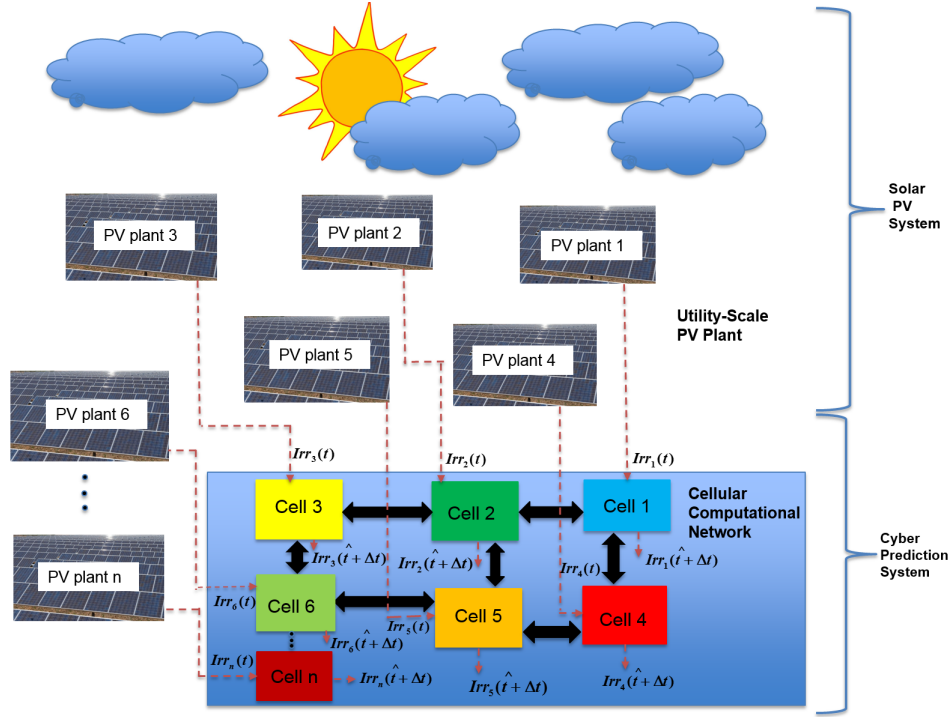
Figure 3.9: Solar irradiance prediction CCN architecture for a utilit-scale PV plant

at time $t-1, (\hat{I}rr_j(t-1+\Delta t))$ is given by (3.19)

$$\hat{I}rr_i(t+\Delta t) = f(Irr_i(t), Irr_j(t), \hat{I}rr_i(t-1+\Delta t), \hat{I}rr_j(t-1+\Delta t)) \qquad (3.19)$$

where i is the current location cell and j is the neighboring location cells, j. j can be 1 cell, 2 cells or 3 cells based on the CCN configuration. According to (3.19) the number of inputs for three CCN configurations are 4, 6 and 8 respectively. f is the CCN computational unit learning algorithm.

3.7.1 Results and Discussion

The CCN configurations are trained and tested on the data at the locations shown in Fig. 3.11. Solar irradiance variations observed on January 4th 2011 at the location "DHHL9" is given in Fig. 3.12. Extremely changing weather conditions are observed between 10.30 am - 1.30 pm time period. For the learning process, the data observed on January 4th are utilized. The location "DHHL9" is compared for all the configurations. The predictions are done for 35s ahead using 1s window data points. MAPEs obtained at the location "DHHL9" is given in Table 3.1.

49
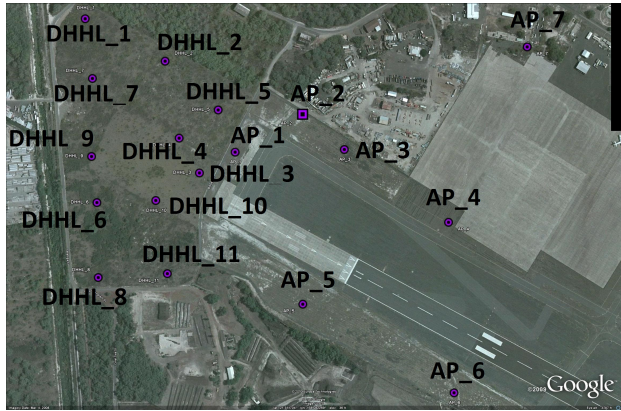
Figure 3.10: Satellite map of the Oahu solar measurement grid, NREL
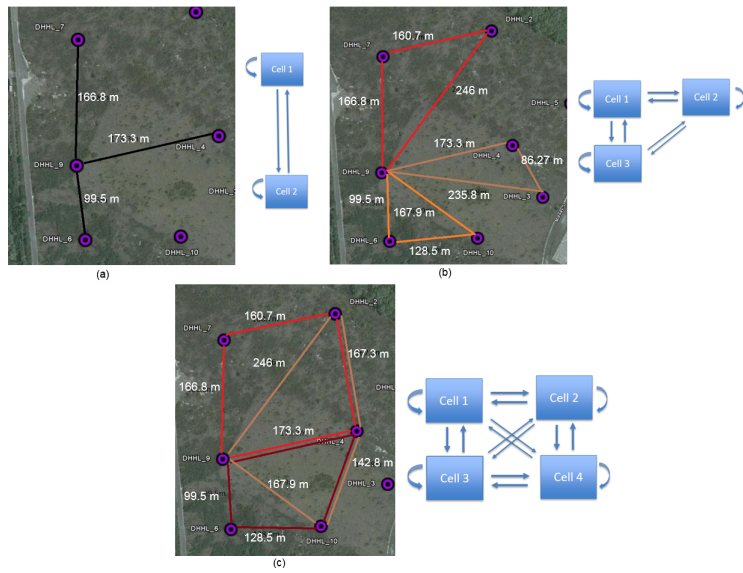
Figure 3.11: CCN Architectures in detail (a) 2 cells, (b) 3 cells and (c) 4 cell

50
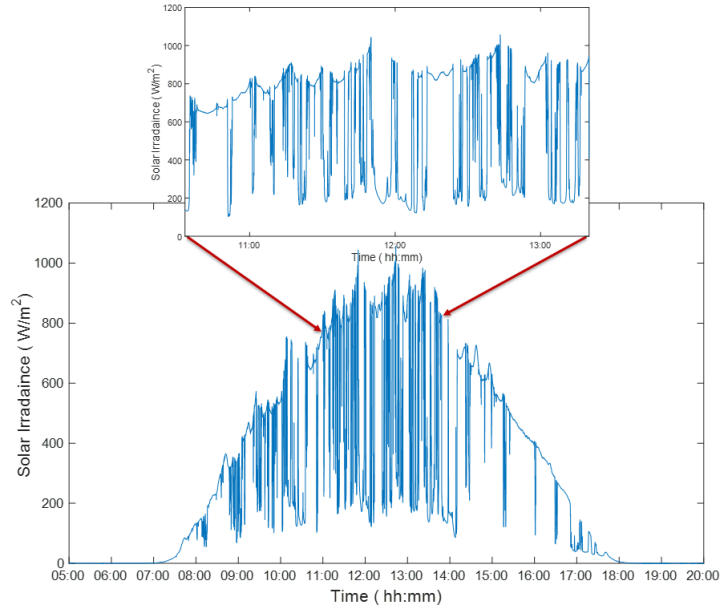
Figure 3.12: Solar irradiance variation observed on January 4th 2011, at location DHHL9

Table 3.1: MAPES OBTAINED FOR CCN BASED SOLAR IRRADIANCE PREDICTION MODEL

CCN Architecture	Name	Spatial group	MAPE %	
			Training	Testing
1 cell	1	DHHL9	21.86	23.58
2 cells	2 -1	DHHL9,DHHL7	20.26	23.20
	2 -2	DHHL9,DHHL6	20.30	23.08
	2 -3	DHHL9,DHHL4	**11.45**	**15.36**
3 cells	3 -1	DHHL9,DHHL7,DHHL2	17.11	19.43
	3 -2	DHHL9,DHHL4,DHHL3	**8.75**	**14.71**
	3 -3	DHHL9,DHHL10,DHHL6	13.88	19.82
4 cells	4 -1	DHHL9,DHHL7,DHHL2,DHHL4	11.53	15.34
	4 -2	DHHL9,DHHL4,DHHL10,DHHL6	10.58	16.12
	4 -3	DHHL9,DHHL2,DHHL4,DHHL10	**10.65**	**15.93**

According the results observed in Table 3.1, CCN configurations 2-3, 3-2 and 4-3 prediction accuracies are higher compared to single unit prediction model (cell1). However, obtaining the best spatial group CCN configuration is a challenging task with uncertain weather changes occur at neighboring locations during different time duration of the day. CCN is capable of using neighboring location data (as remote virtual sensors) to predict the information. This allows CCN to learn the solar irradiance variability around the location, thus more intelligent compared to an isolated predictor (single ESN predictor). However, the prediction accuracy is totally depending on the distance between each cells ,the number of cells and the connectivity between the cells. An accurate CCN based solar irradiance predictor can be designed by intelligently analyzing available neighbor information.
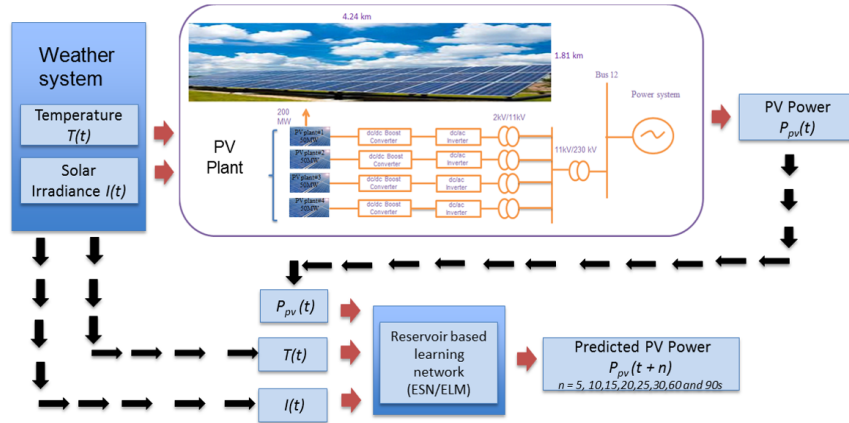
Figure 3.13: Schematic diagram of a real-time simulation of a large PV plant consisting of four 50 MW PV plants with actual weather (Clemson, SC) on RTDS.

3.8 PV Power Predictions

In literature, numerous methodologies have been proposed for long term and short term forecasting of PV power. These methods include mathematical equations, regression analysis and linear time series models. These methods are not optimal for PV power prediction, since the PV power generation is non-linear and stochastic. Artificial neural networks (ANNs) have been used widely for nonlinear stochastic predictions. Recent research in PV power predictions uses ANNs including feed-forward neural networks (FFNN) and recurrent neural networks (RNN). However, these networks are difficult to train using complex input signals to provide sufficient prediction accuracy. In this research reservoir based neural networks ESN and ELM prediction models [5] are implemented to predict the PV power generation. Reservoir networks are easy to implement and provide faster learning rate. Additionally an ANFIS model is used to predict the PV power [6]. These models are explained in detail in rest of this section.

PV power $(P_{pv}(t))$ data used for the model implementations are taken from a simulated PV plant. A 200 MW PV plant is simulated on real-time digital simulator (RTDS) given in Fig. 3.13. The Real-time Power and Intelligent Systems (RTPIS) lab at Clemson university archives weather data parameters on a second basis. These weather parameters include temperature $(T(t))$, solar irradiance $(I(t))$, wind speed and wind direction.

3.8.1   Echo State Network (ESN) based PV Power Predictions

Inputs to the ESN model are current time temperature $(T(t))$, solar irradiance $(I(t))$ and PV power $(P_{pv}(t))$. PV power predictions done for multiple time steps, time steps are very short, in order of few seconds to a minute plus. A single dynamic reservoir is exploited to provide multiple predictions (8 time steps) at different time instances with the same input and reservoir. The 8 prediction time steps are 5s, 10s, 15s, 20s, 25s, 30s, 60s and 90s. The created ESN is tested with different parameter values, the most performing ESN has 100 reservoir neurons. Reservoir weights are populated in a manner that guaranteed the echo state property. It is populated by setting 1% of the matrix in to a randomly generated values between [-1, 1] and spectral radius is set to 0.8. Input weights are populated based on the number of inputs and reservoir neurons. Feedback weights (Wfb) are populated using randomly selected values from a uniform distribution ranging [0,1] and the settling time of the reservoir is set to be within the first 100 samples. A comparison of ESN and improved versions with several versions of RNNs is given in [71]. ESNs show lowest computation time and better accuracy compared to RNNs.

3.8.2   Extreme Learning Machine (ELM) based PV Power Predictions

Similar to ESN, ELM is developed to predict 8 time step ahead using a single hidden layer matrix. he 8 prediction time steps are 5s, 10s, 15s, 20s, 25s, 30s, 60s and 90s. ELM is tested with different number of hidden layer neurons, the most performing ELM has 100 hidden neurons. Input weights are populated based on the number of inputs and hidden layer neurons.

3.8.3   Adaptive Neuro Fuzzy Inference System (ANFIS) based PV Power Predictions

Fuzzy systems are useful in modeling uncertainties and handling vagueness in data. Combination of neural networks adaptive capabilities and fuzzy logic uncertainty modeling capabilities results in robust information processing systems. ANFIS is an integration of neural networks to develop fuzzy inference systems from input-output data sets. ANFIS is a suitable approach for weather and PV power output predictions [6], which requires uncertainty modeling and previous behavior adaptation for more accurate predictions.

ANFIS maps inputs through input membership functions and related parameters, outputs
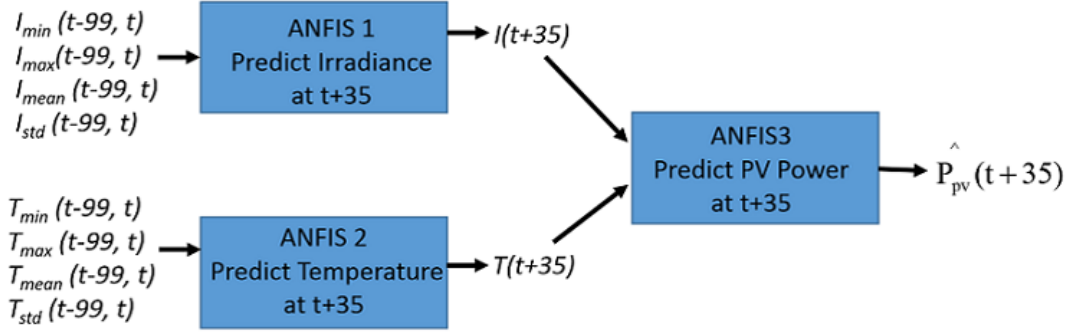
Figure 3.14: Schematic diagram of adaptive neuro-fuzzy inference systems for PV power prediction.

through output membership functions and related parameters to construct the input-output mapping. ANFIS system is implemented using Matlab fuzzy logic tool box, which uses a hybrid learning algorithm to tune the membership functions. Algorithm includes a combination of the least-squares and back-propagation gradient descent methods. A Schematic diagram of the ANIFS implemented for PV power prediction is given in Fig. 3.14. The system includes three prediction models, Temperature prediction model uses minimum, maximum, mean and standard deviation temperature values observed during past 100s as inputs to the model in predicting 35s ahead temperature. The Inference system uses 16 rules for this prediction. Similarly solar irradiance model uses minimum, maximum, mean and standard deviations observed during past 100s to predict the solar irradiance in 35s ahead. Finally, these two predicted outputs are fed into the PV power prediction model to predict the 35s ahead PV power.

3.8.4   Results and Discussion

Learning and Testing PV power variations observed for $90s$ ahead predictions are given in Figs, 3.15 and 3.16. APEs are calculated for each data point in the data set. Then the APE values are sorted in ascending order and 95% of the data points are selected to calculate mean absolute percentage error (MAPE). Remaining 5% of data set is neglected by assuming those points are outliers. Maximum APE values of 95% of data points for eight time steps are given in Table 3.2. According to the Table 3.2, maximum APEs for ELM are better than that of ESN for time steps t+30, t+60 and t+90 for both learning and testing phases. The difference between maximum
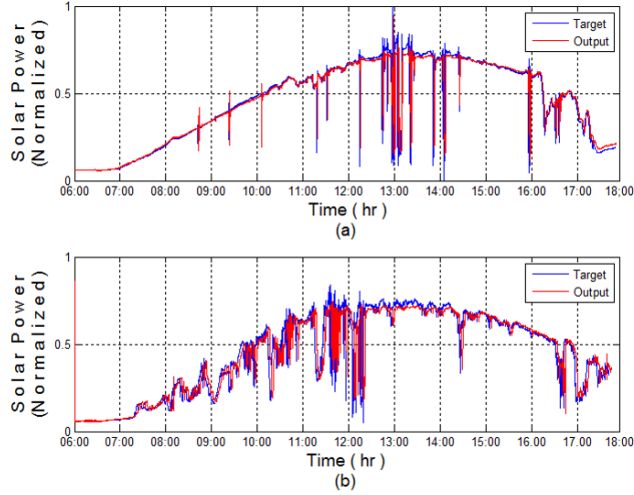
Figure 3.15: (a) Learning target and output data distribution for prediction time step 90s obtained by ESN and (b) Testing target and output data distribution for prediction time step 90s obtained by ESN.

APE of ESN and ELM is large for training phase compared to testing phase for these time steps. It is harder to train ESN to predict large time step values due to its complex, highly non-linear reservoir. During the testing phase, the values are approximately equal. ESN reservoir retains better performance during testing. However, about 90% of ESN APEs are less then APEs with ELM. This implies that ESN performs well than ELM for most time steps.

Table 3.2: MAXIMUM APE FOR 95% OF DATA

Prediction at time t	Learning APE%		Testing APE %	
for time instant	ESN	ELM	ESN	ELM
t+5	4.0510	28.5779	7.1648	28.6682
t+10	6.5555	22.5250	12.2297	22.5588
t+15	6.6136	19.6154	12.8436	19.9516
t+20	8.4515	17.1191	15.0058	17.9940
t+25	10.4764	12.7942	17.4259	17.3319
t+30	12.9866	11.1254	19.7346	19.2508
t+60	25.4340	16.3513	30.8825	29.7368
t+90	32.0149	26.6144	37.7495	37.6847

Both the ESN and ELM models are executed for 20 trials and the mean of APEs for 95% of the data set (5% of outliers are removed) are obtained for eight time step predictions. In Table 3.3, the MAPEs obtained for ESN and ELM for all eight time step predictions are compared.

Table 3.4 shows the correlation coefficients for target versus predictions obtained for ESN and ELM for all the time steps (100% of data set).
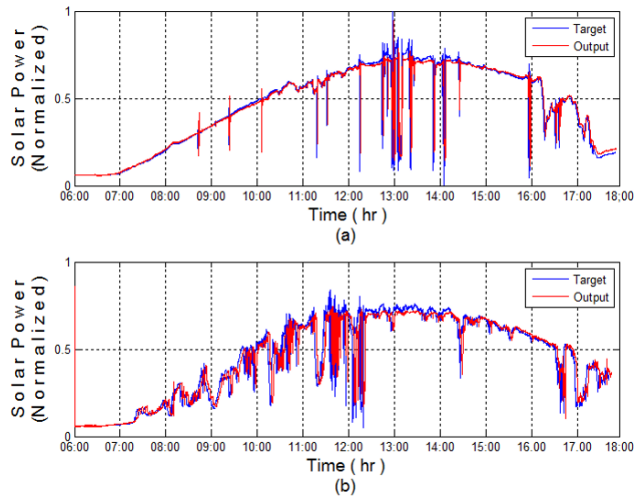
Figure 3.16: (a) Learning target and output data distribution for prediction time step 90s obtained by ELM and (b) Testing target and output data distribution for prediction time step 90s obtained by ELM.

Table 3.3: MAPE for learning and testing data

Prediction at time t for time instant	Learning MAPE%		Testing MAPE %	
	ESN	ELM	ESN	ELM
t+5	0.7221	3.8587	1.1954	4.4389
t+10	1.3590	3.7714	2.3811	4.5701
t+15	1.5381	3.6587	2.5328	4.6934
t+20	1.8416	3.5934	3.0215	4.7822
t+25	2.2709	3.3998	3.6592	4.5902
t+30	2.5613	3.1314	3.9442	4.3882
t+60	4.2741	4.4787	6.0993	6.3959
t+90	5.4328	6.2039	7.6080	8.6509

Training and testing results observed for PV power predictions using ANFIS and ESN methods are shown in Figs. 3.17 and 3.18.

MAPEs obtained for solar irradiance, temperature and PV power predictions are given in Table 3.5. According to the Table 3.5, solar irradiance and temperature predictors have higher accuracy in training and testing stages compared to the final PV power estimation. Combination of two predictors reduce the accuracy of the integrated PV power predictor system.

MAPEs obtained for training and testing stages of the ANFIS and ESN are given in Table 3.6. According to the Table 3.6 (showing PV power prediction measures), ESN performs well in both training and testing stages compared to ANFIS during night and day times. It is clear from these results that ESNs are able to perform well on complex time series predictions. Daytime measures
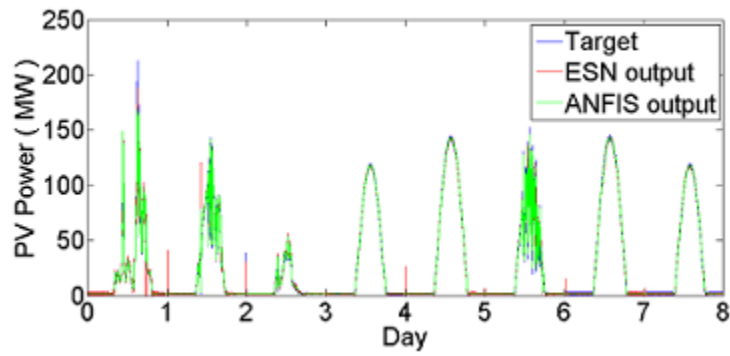
Figure 3.17: Target, ESN predictor output and ANFIS predictor output for training phase
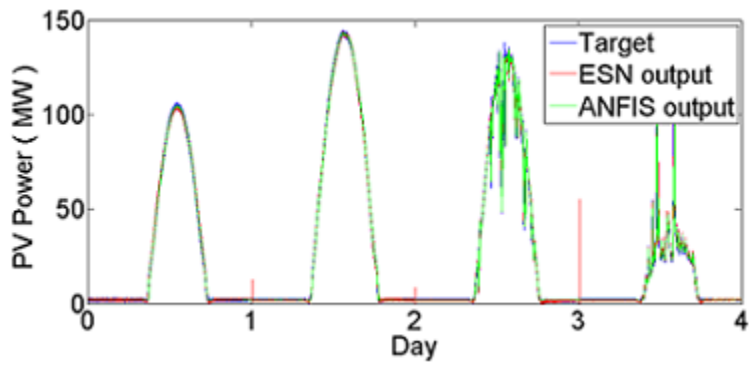
Figure 3.18: Target and ESN predictor output and ANFIS predictor output for testing phase

57

Table 3.4: CORRELATION COEFFICIENT FOR LEARNING AND TESTING DATA

Prediction at time t for time instant	Learning MAPE%		Testing MAPE %	
	ESN	ELM	ESN	ELM
$t+5$	0.9874	0.9846	0.9907	0.9883
$t+10$	0.9781	0.9765	0.9843	0.9827
$t+15$	0.9662	0.9636	0.9777	0.9764
$t+20$	0.9566	0.9534	0.9727	0.9714
$t+25$	0.9484	0.9448	0.9691	0.9677
$t+30$	0.9430	0.9381	0.9650	0.9630
$t+60$	0.9245	0.9152	0.9451	0.9429
$t+90$	0.9153	0.9040	0.9277	0.9242

Table 3.5: MAPEs OBTAINED FOR ANFIS APROACHE

ANFIS	MAPE	
	Training	Testing
Solar Irradiance predictor	6.9603	7.4378
Temperature predictor	2.9525	1.0681
PV power predictor (combined)	26.0899	25.8076

reveal better accuracies compared to night time measures.

Table 3.7 compare and contrasts the two approaches used in this study. ANFIS is developed in this study using the Matlab fuzzy toolbox where as ESN is developed using code written in Matlab. Therefore, knowledge of ESN is required. Thus, higher development complexity with ESNs compared to ANFIS. ANFIS predictor system (three ANFISs) is computationally more complex compared to the ESN. It is also to be noted that ANFIS system is developed in iterative manner compared to the one-shot training approach with ESNs. Thus, convergence with ANFIS requires more epochs and time. Data requirements for the systems developed in this study for decision-making by ANFIS is higher than with the ESN. On other hand, ANFIS is a fuzzy system and has the capability to handle vagueness and uncertainty compared to a neural network. It is expected that the performance of the ANFIS predictor can be improved with more development time.

Table 3.6: MAPEs OBTAINED FOR ANFIS AND ESN APPROACHES ON PV POWER

Method	MAPE					
	Training			Testing		
	Day	Night	All	Day	Night	All
ANFIS	22.9600	28.3889	26.0899	15.5690	53.8001	25.8076
ESN	5.7752	13.4408	10.1946	4.1044	14.2487	10.2686

Table 3.7: ESN vs ANFIS

Property	ANFIS	ESN
Development complexity	Low	High
Computational time	High	Low
Convergence	High	Low
Data storage requirement	High	Low
Handling vagueness	High	Low

3.9 Power System Frequency Predictions

Current power system experiences power and frequency fluctuations with the increasing penetration levels of PV power. Power system frequency needs to be maintained under a desired frequency (60Hz in USA/ 50Hz in Europe) which has become difficult with the high penetration levels of PV. Having a foresight of frequency fluctuations provide ths SI for power system monitoring, control and protection under increasing levels of PV power integration in the grid.

Numerous frequency prediction and estimation methodologies have been introduced in literature. A state-space method and an uncertain basic function modeling frequency prediction method [72], Kalman filter [73], Newton type algorithms [74], artificial neural networks (ANN)[75] and support vector regression [76] are few approaches in estimating/predicting power system frequencies. These traditional approaches are suitable for small systems and learning slow dynamics. CCN is a distributed scalable architecture, which is more suitable for predicting parameters in large complex systems with faster dynamic learning. A generalized neuron (GN) based CCN is implemented for predicting power system frequency in [77]. In this study a cellular computational extreme learning machine network (CCELMN) based frequency prediction approach is presented for a two-area for machine power system with PV plant integration [8].

3.9.1   Cellular Computational Extreme Learning Machine Network (CCELMN)

CCN implemented in this research uses the topology of the two-area four machine power system in Fig. 3.19. The system includes twelve Buses. PMUs are deployed at each bus of the system. A cell is implemented to represent a Bus. Each cell uses an ELM as the computational unit of the cell. Hence referred as cellular computational extreme learning machine network (CCELMN).

The CCELMN implemented is given in Fig. 3.20. Each cell of the CCN represents a Bus and indicating by a black box. Cell communication links are defined based on the electrical distance between bus-lines. Bus 1, Bus 2, Bus 3, Bus 4 and Bus 12 (Generator buses and the Bus connected
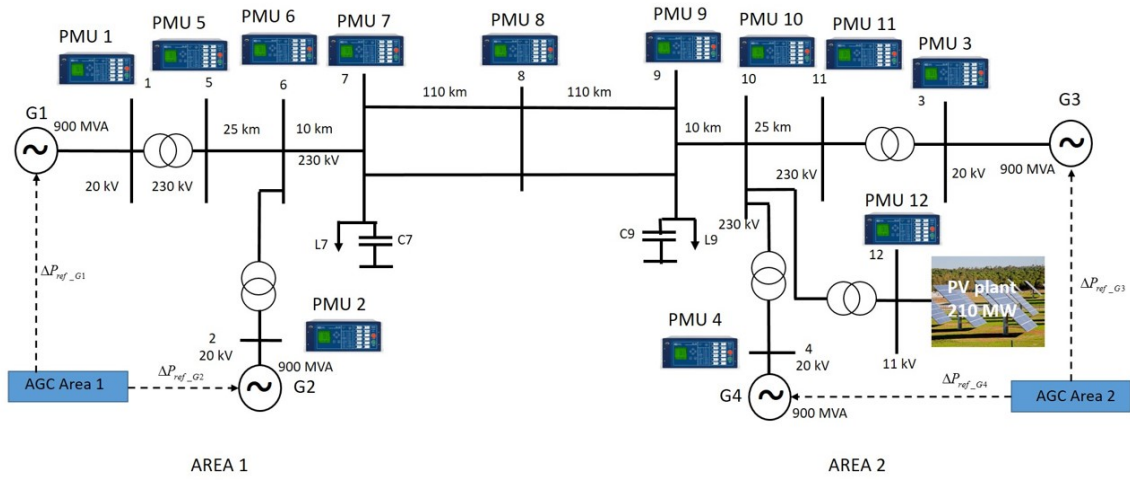
Figure 3.19: Two-area four machine power system with PV plant
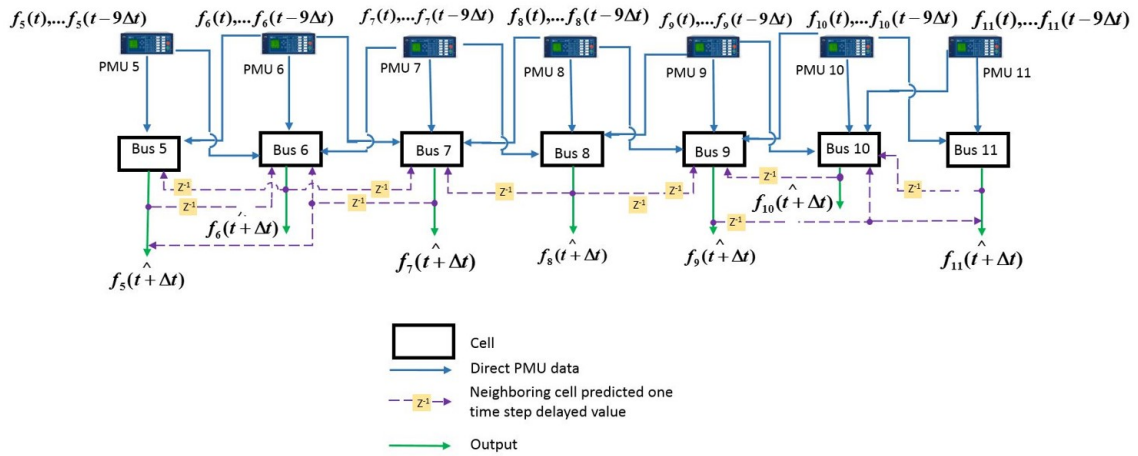
Figure 3.20: CCELMN for predicting bus frequencies of two-area four machine power system with PV plant; (intercommunication are designed based on the electrical distance between buses)
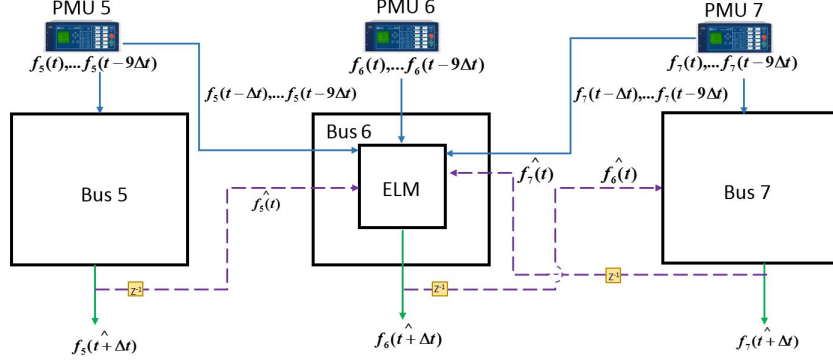
Figure 3.21: Detalied CCELMN cell representation for cell 6 given in Fig. 3.20

to PV plant) are neglected in this study, since the electrical distance between these Buses and the neighboring connecting Bus is negligible. Data flow directions are indicated by arrows. Direct PMU measurement data flows are represented by blue, neighboring cell predicted data flows are represented by purple and cell outputs are represented by green. Brown box with Z^1 represents 1 time step time delay. Time delayed values are used since the cell computations needs to be done in parallel in obtaining near real-time prediction values.

The inputs and outputs of each cell are given in (3.20), (3.21).

$$Input_i(t) = (f_i(t-9\Delta t), f_i(t-8\Delta t), \dots, f_i(t-\Delta t), f_i(t), (f_j(t-9\Delta t), f_j(t-8\Delta t), \dots, f_j(t-\Delta t), \hat{f_i}(t)) \tag{3.20}$$

$$Output_i(t) = f_i(t \hat{+} \Delta t) \tag{3.21}$$

where $f_i(t)$ and $f_j(t)$ are frequencies at time t at the ith cell and j^{th} cell respectively. j represent all neighboring Buses. $\hat{f_j}(t)$ is the jth cell predicted frequency at time $t - \Delta t$. Δt is the prediction time step which is 33ms in this study. $f_i(t \hat{+} \Delta t)$ is the ith cell predicted frequency at $t + \Delta t$. Input and Output data flows are clearly indicated in Fig. 3.21.

All the ELM cells are learned with online sequential ELM (OS-ELM) learning algorithm, explained in Section 3.1.1.2. The algorithm provides better results for dynamic inputs.

Table 3.8: MAPE, STD, RMSE and Skill Factor(S) obtained for operation phase

Bus No	MAPE %			STD			RMSE			S %		
	ELM	CC ELMN	Persi- stence	ELM	CC ELMN	Persi- stence	ELM	CC ELMN	Persi- stence	ELM	CC ELMN	Persi- stence
6	0.0089	0.0075	0.0117	0.0092	0.0091	0.0103	0.0077	0.0072	0.0093	17.20	22.58	0
7	0.0105	0.0090	0.0142	0.0111	0.0108	0.0128	0.0093	0.0085	0.0115	19.13	26.08	0
9	0.0231	0.0225	0.0314	0.0213	0.0212	0.0242	0.0189	0.0185	0.0238	20.58	22.26	0
10	0.0153	0.0139	0.0221	0.0150	0.0152	0.0173	0.0127	0.0125	0.0168	24.40	25.59	0

3.9.2   Results for Power System Frequency Predictions

In order to reflect the frequency fluctuations in the system pseudo-random binary signals (PRBS) are applied to all four generator excitation systems.

The algorithm is tested on a real-time simulation system (RTDS). In order to reflect the frequency fluctuations, pseudo random binary signals (PRBS) are applied to all four generators. The data used for the learning and operation process includes 5 minutes of data with 33ms of window size. Learning and operation data sets are divided in 95%:5% ratio.

Accuracy measures observed for operation phase are given in Table 3.8. Independent ELM predictions, CCELMN predictions and persistence model are compared. According to the results, CCELMN predictions outperforms other two approaches in all three accuracy measures, MAPE, RMSE and S. The operational results observed are shown in Fig. 3.22. The comparison of actual frequency versus predicted frequency values observed for three approaches, CCELMN, independent ELM and persistence prediction are given in Fig. 3.23. This shows CCELMN predictions outperform other two models. CCELMN cells are connected with neighboring cells based on the electrical distance between connected Bus lines of the studied system. Hence CCELMN cells can dynamically learn from neighboring cells.

3.10   Summary

Accurate and efficient predictions create SI in power system operation. In this research, multiple PV power prediction models and a solar irradiance prediction model are presented. The solar irradiance prediction method is implemented for a spatially distributed utility-scale PV plant. The model uses CCN architecture, which is a distributed and scalable architecture for modeling
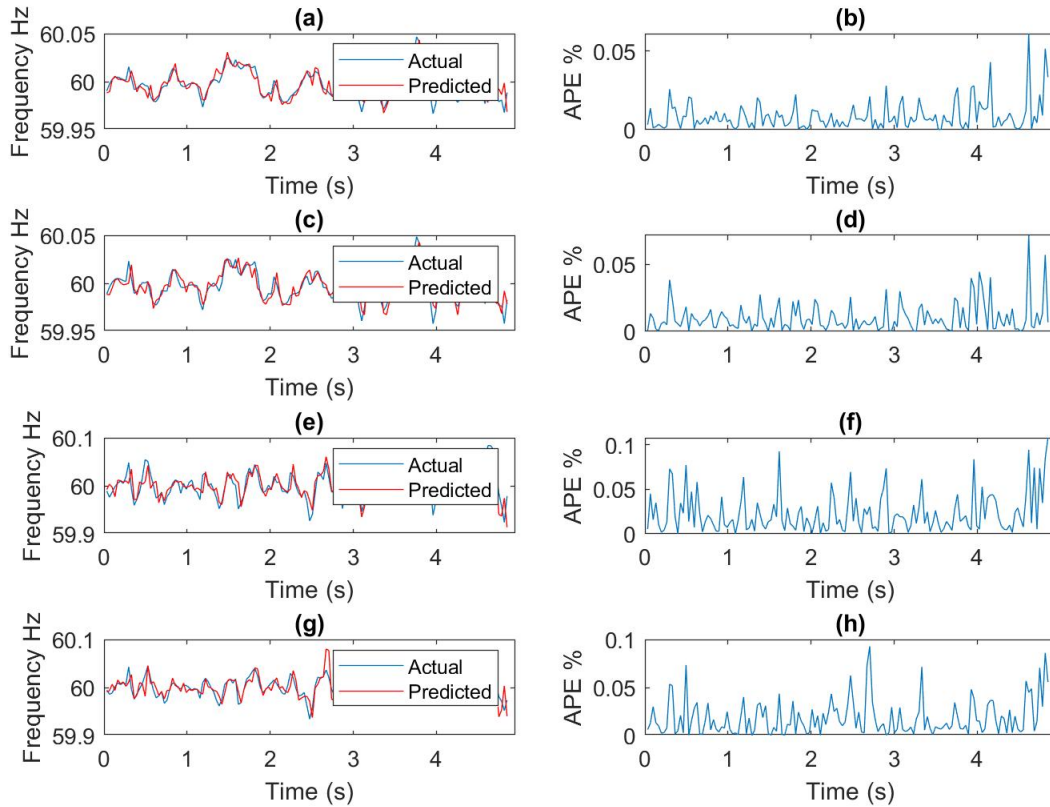
Figure 3.22: CCELMN frequency predictions. (a) Predicted versus actual frequency at Bus 6, (b) APE for frequency predictions at Bus 6, (c) Predicted versus actual frequency at Bus 7, (d) APE for frequency predictions at Bus 7, (e) Predicted versus actual frequency at Bus 9, (f) APE for frequency predictions at Bus 9, (g) Predicted versus actual frequency at Bus 10, (h) APE for frequency predictions at Bus 10.
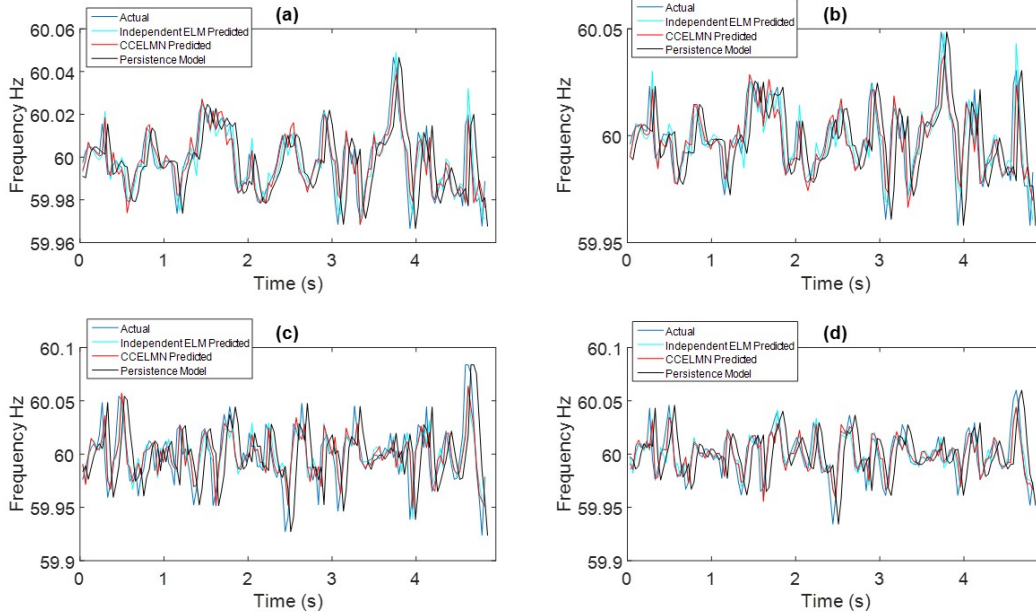
Figure 3.23: Comparison of actual, independent ELM, CCELMN and persistence model predictions. (a) at Bus 6, (b) at Bus 7, (c) at Bus 9 and (d) at Bus 11

dynamics of large systems. Reservoir based neural networks are more suitable for modeling non-linear dynamics of PV power generation. ESN and ELM prediction models provide accurate short term multi-time step predictions with minimum computational complexity. An ANFIS model is implemented by considering advantages of fuzzy systems.

A CCELMN is presented for predicting power system bus frequencies. CCELMN consists of interconnected cells where each cell includes an ELM computational unit. CCELMN prediction results are compared with an independent ELM and persistence model predictions. It is observed that the CCELMN outperforms other two approaches. CCELMN is capable of dynamically learning from interconnected Buses in the system. Hence it outperforms independent ELM predictions. CCELMN is more suitable for large interconnected systems such as power systems. The approach of integrating SI for resilient and sustainable tie-line bias control under uncertain environments is explained in next section.

Chapter 4

Resilient and Sustainable Tie-line Bias Control for a Power System in Uncertain Environments

4.1 Introduction

The conventional approaches of AGC has become challenging with the integration of solar PV power into the power system [78]. It is necessary to have intelligent control techniques to overcome the challenges in variable renewable energy (VRE) sources. Several studies have demonstrated the value of different strategies to improve the AGC performance in the presence of VRE sources [79]. Recent studies include an optimal mileage based dispatch (OMD) algorithm [80], a lazy reinforcement learning method [81], a predictive optimal PID plus second order derivative method [82] and, a coordinated active power control strategy [83]. The use of synchrophsor networks consisting of phasor measurement units (PMUs), can improve AGC performance to mitigate the challenges of integrating VRE. Improved AGC strategies are introduced by utilizing PMU measurements and sensor data[2, 36, 84]. In this research, the importance of PV power and frequency predictions for improved tie-line bias control is explored. Predictions are obtained by utilizing PMU data of the power system synchrophasor network.

Synchrophasor networks need to be secure to ensure reliability in smart grid operation and control. Delayed or missing measurements from PMUs in real-time power system applications lead to power system frequency instability. Although, the use of virtual private networks (VPNs) eliminate many security vulnerabilities, VPNs are still vulnerable to denial of service (DoS) attacks that exploits side-channels [36].

Accurate predictions of system dynamics can overcome the challenges presented by PV power integration. The main contributions of this section are:

- With PV power predictions and virtual synchrophasor network (VSN) included in AGC operations, a resilient and sustainable tie-line bias control is achievable under uncertain environments, including changing weather and load conditions.

- The VSN based on Cellular computational Echo State Network (CCESN) can mitigate the impact(s) of denial of service attacks on the physical synchrophasor network.

4.2 Cyber-Physical Power System

The cyber-physical system (Fig. 4.1) studied in this research consists of four layers namely; power system (two-area four machine power system and synchrophasor network), AGC (Area-1 AGC and Area-2 AGC), prediction models (PV power predictor and VSN frequency predictor), and cyber-security (DoS attack countermeasures).

4.2.1 Two-area Four-Machine Power System

The power system consists of two areas connected by two parallel transmission lines, each area has two synchronous generators, all rated at 900 MVA (4.1). Generators G1 and G2 are in Area-1 and G3 and G4 are in Area-2. All of the generators are equipped with their primary controllers, including turbine governors, automatic voltage regulators and power system stabilizers (PSSs). The PSS structure used in this power system is a second order lead-lag compensator as shown in Fig.B.2. The power system is developed and simulated on a real-time digital simulator (RTDS). The experimental setup consisting of the RTDS, weather station, synchrophasor network, and prediction models is given in Fig. B.1.
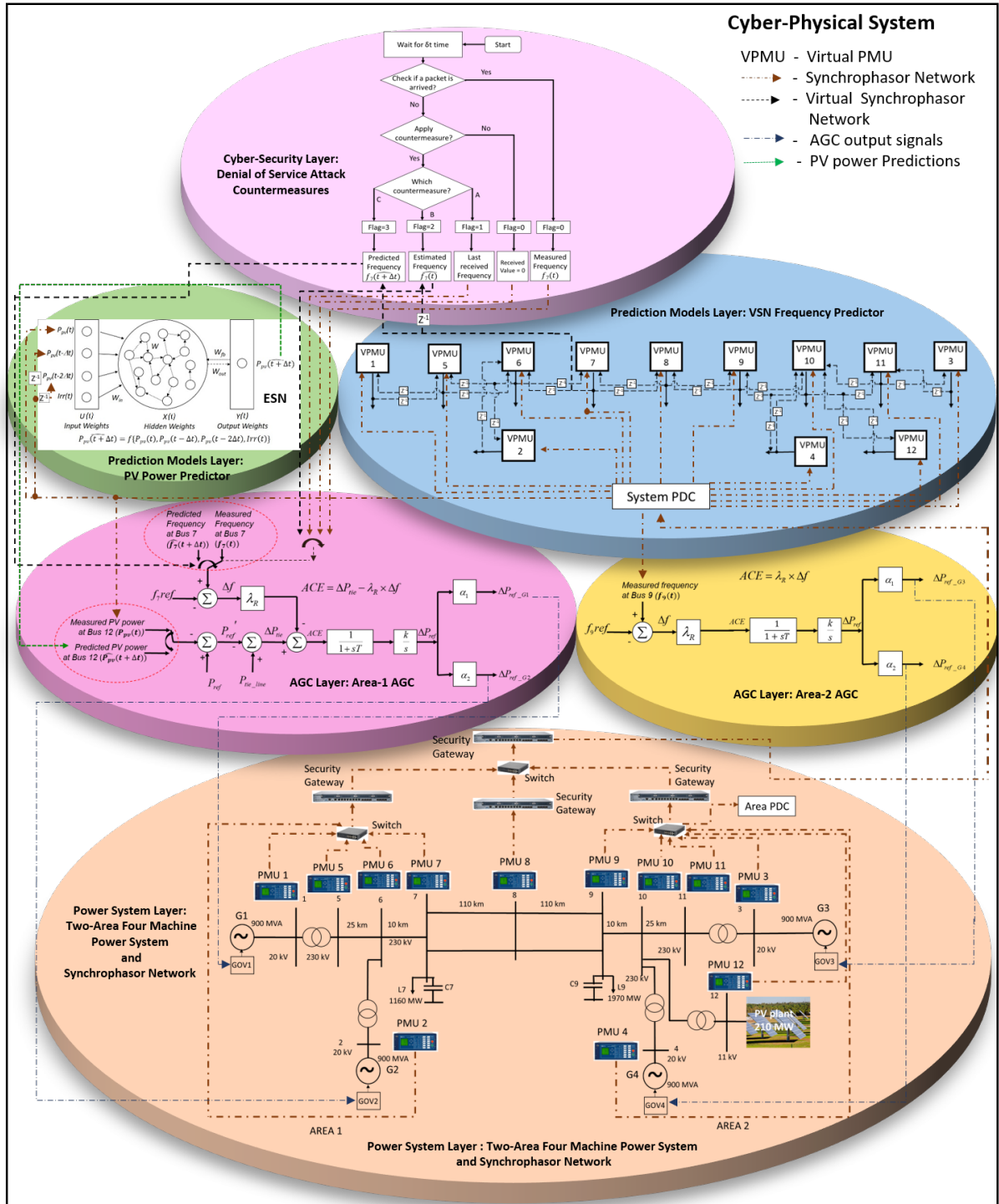
Figure 4.1: Cyber-physical system consisting of the power system, AGCs, prediction models, and cyber-security layers.

4.2.2 PV Power Plant

A large PV plant of capacity 210 MW is installed at Bus 12, a 230 kV utility transmission grid bus in Area-2 of the power system [85]. Real-time weather profiles, solar irradiance (Irr(t)) and temperature (Temp(t)) are used to simulate the PV plant generation.

4.2.3 Synchrophasor Network

Analogue voltages and current values are transmitted from the RTDS simulation to physical PMUs. Physical PMUs are placed at each bus of the system to to measure the bus frequencies, generator power outputs, tie-line power flow and PV plant power generation. A dedicated communication synchrophasor network is used to transmit PMU measurements to upper level layers (Fig. 4.1). The synchrophasor network configuration given in [36] is used for this study. The network consists of secured subnets, which are connected by a dedicated network with a security gateway protecting each secured subnet. The use of security gateways reduce the risk and cost of transmitting critical information securely through a long distance network, eliminating many vulnerabilities such as packet sniffing, data spoofing, malicious code injection, and replay attacks. VPN tunnels are established between each of the security gateways. The traffic transmitted through VPN tunnels is encrypted by the security gateway. This configuration with security gateways eliminate many vulnerabilities but still vulnerable to DoS attacks that exploits side-channel vulnerability. Phasor data concentrator (PDC) produces time-aligned output data streams by time-synchronizing phasor data receive from multiple PMUs. There are two PDCs, each located at a secured subnet. The PMUs located at Area-1 are sending measurement to a system PDC and the PMUs located at Area-2 are sending measurement to Area PDC. The system PDC also collects measurements from Area PDC. OpenPDC is an open source synchrophasor data concentrator software, which is used as the PDC in this study.

4.2.4 AGC and Tie-line Bias Control

The block diagram for the AGCs in Area-1 and Area-2 (AGC-1 and AGC-2) are given in Fig. 4.1. AGCs are designed with proportional-integral (PI) controllers. Corresponding AGC parameters are given in Table B.1. The objective of each area's AGC is to maintain the frequency at the nominal value (f_7ref). In addition, the AGC-1 also changes the tie-line power flow based on
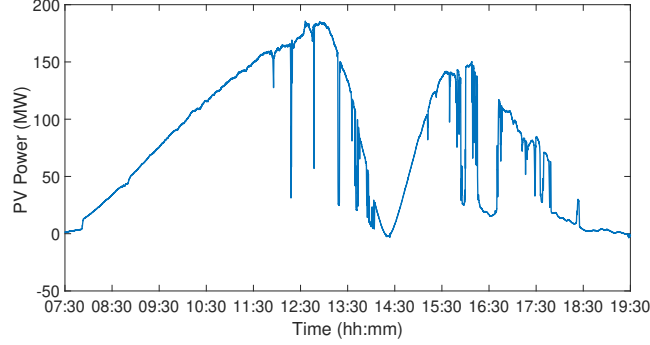
Figure 4.2: PV Power generation observed during Great American Eclipse of August $21^{st}, 2017$.
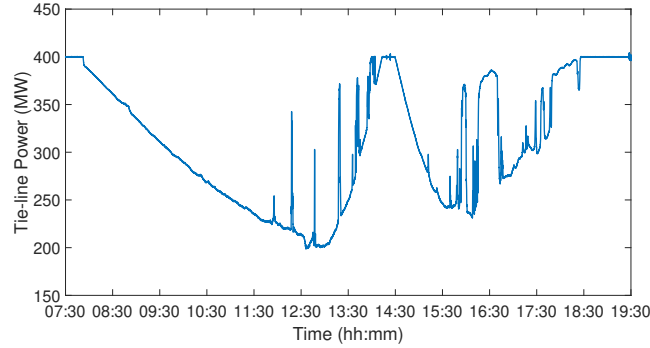
Figure 4.3: During the Tie-line power flow observed during Great American Eclipse of August $21^{st}, 2017$.

the information received from the PMU at the PV plant in Area-2. The objective is to adjust the power outputs of generators G1 and G2 to make the ACE equal to zero. The PV power generation in Area-2 offsets the power outputs of G1 and G2, thus enabling maximum PV power generation utilization in supplying the load demand in Area-2. The scheduled interchange value (reference tie-line power flow (P'_{ref}) is adjusted in real-time based on the PV power generation.

PV power generation and corresponding tie-line power variation obtained with AGC-1 operation on the Great American Eclipse of August $21^{st}, 2017$ are shown in Figs. 4.2 and **??**. Under normal operating conditions (when the PV power generation is 0 MW), a 400 MW (P_{ref}) tie-line power flow from Area-1 to Area-2 is observed.

The AGC adjusts the respective generators' governor references at every one second interval. However, the sum of the response times of AGC and generator governor is greater than one second. In other words, the inputs to the AGC at time t provides consequent changes in the system at time $t + \Delta t$. The time delay $(\Delta t > 1)$ is the response time (frequency bandwidth) of the AGC and

69

governor. The tie-line power reference (P'_{ref}) of the AGC-1 changes dynamically with respect to the current PV power generation, without considering this time delay. Therefore, the deviation in tie-line power flow (P_{tie_line}) from its commanded reference value (P'_{ref}) due to the response time of AGC and governor is minimized by predicting the PV plant power output, Predicted PV power. The prediction time step is synchronized with the optimal frequency bandwidth (response time (Δt)) of the AGC-1 and governors of generators G1 and G2. The optimal prediction time step is determined to minimize the tie-line power flow deviation, which is founded to be approximately 30s for this study[?]. This performance is further enhanced by predicting Area-1 frequency Predicted frequency by considering response time for frequency. The frequency prediction time step is determined to minimize the frequency deviation, which is 1s for this study. Two prediction parameters are shown in highlighted dash circles in Fig. 4.1. Predicted PV power ($\hat{P}_{pv}(t + \Delta t)$) and Predicted Frequency ($\hat{f}_7(t + \Delta t)$) values are applied instead of measured PV power and frequency, respectively.

4.3 Results and Discussion

North American Electric Reliability Corporation (NERC) defines control performance standard 1 ($CPS1$) to measure the steady-state interconnection frequency in balancing authorities. Control performance standard 2 ($CPS2$) is introduced as a safety metric for $CPS1$. If $CPS1$ was the only control performance standard, the balancing authority could excessively increase or decrease the generation and obtain a very good $CPS1$, yet impact its' neighbors with excessive power flows [31]. In this study, $CPS1$, $CPS2$ and related measures are used as the performance metrics.

The CPS1 is given in (4.1) - (4.3)

$$CPS1 = (2 - CF) \times 100\% \tag{4.1}$$

$$CF = \frac{(CF_{1min})_{12months}}{(\epsilon)^2} \tag{4.2}$$

$$CF_{1min} = \frac{(ACE_{1min})}{-\lambda_R} \times \Delta f_{1min} \tag{4.3}$$

where ACE_{1min} is the average ACE within a minute, Δf_{1min} is the average Δf within a minute and

CF_{1min} is the average CF within a minute and $(CF_{1min})_{12months}$ is the CF_{1min} obtained over 12 months. In this study, ϵ is considered as 18 mHz, NERC defined value for Eastern Interconnection. This is the benchmark frequency noise calculated by root mean square error of one minute averages of frequency. If the one minute average of ACE and frequency deviation are "out of phase", then the $CPS1$ is greater than 200%. Therefore, obtaining small positive CF_{1min} or larger negative CF_{1min} indicates better performance of the system.

CPS2 related metrics are given in (4.4) -(4.6)

$$CPS2_{10min} = \frac{periods \quad without \quad violations}{total \quad periods \quad over \quad the \quad month} \times 100\% \tag{4.4}$$

$$periods \quad without \quad violations = \sum non - violated_{ACE} \tag{4.5}$$

$$non - violated_{ACE} = \begin{cases} 1 & \text{, if } ACE_{10min} < L_{10} \\ 0 & \text{, otherwise} \end{cases} \tag{4.6}$$

where ACE_{10min} is the average ACE within 10 minutes and L_{10} is decided based on the balancing authority size [31], in this study $L_{10} = 30.4667$, calculated based on the Table 4 in [31] assuming the balancing authority size of each Area is 1800 MW. Equation (4.4) is modified to consider total periods over the simulation, instead of total periods over the month due to the availability of test data. Moreover, $CPS2$ related metrics ($CPS2_{4s}$ and $CPS2_{1s}$) are calculated by considering average ACE within 4 seconds (ACE_{4s}) and 1 seconds (ACE_{1s}) for the better comparison of performance. The calculations are performed as given in (4.4) -(4.6). Total number of ACE violations observed for ACE_{4s} and ACE_{1s} are also calculated as given in (4.7) - (4.10).

$$total - violated_{ACE_{4s}} = \sum violated_{ACE4s} \tag{4.7}$$

$$violated_{ACE4s} = \begin{cases} 1 & \text{, if } ACE_{4s} > L_{10} \\ 0 & \text{, otherwise} \end{cases} \tag{4.8}$$

$$total - violated_{ACE_{1s}} = \sum violated_{ACE1s} \tag{4.9}$$

$$violated_{ACE1s} = \begin{cases} 1 & \text{, if } ACE_{1s} > L_{10} \\ 0 & \text{, otherwise} \end{cases} \qquad (4.10)$$

4.3.1 Performance of AGCs and Tie-line Bias Control

Tie-line bias control performance is analyzed under four different test cases, including under real-time variable weather conditions, under severe load and weather changes, under weather conditions obtained on the "Great American Eclipse" on August 21st, 2017, and under denial of service (DoS) attacks performed on physical PMUs. The performance of the test cases are investigated in the following subsections.

4.3.1.1 Real-time Weather

Tie-line bias control performance is analyzed under different weather conditions. The analysis results are categorized based on four PV power variations. PV power generation, tie-line power and CF_{1min} calculated with and without predictions obtained under four PV power variation categories are shown in Figs. 4.4 - 4.15. Positive and negative CF_{1min} counts, Accumulated CF_{1min}, $CPS1$, $CPS2_{10min}$, $CPS2_{4s}$ and $CPS2_{1s}$ values calculated are recorded in Table 4.1. All four PV power variation categories have high negative CF_{1min} counts and less positive CF_{1min} counts when predictions are applied, which indicates better performance with predictions compared to without predictions. Although, the differences between Accumulated CF_{1min} and $CPS1$ values are very small over one hour time periods analyzed in this study, long term execution of prediction algorithm increases the differences between performance metrics, indicating the usefulness of the prediction algorithm in improving AGC performance. $CPS2$ values observed for ACEs averaged within 10 minutes, 4 seconds and 1 second time periods are 100% for both test cases, indicating no under generation or over generation due to $CPS1$ improvements.

4.3.1.2 Load Profiles with Variable Weather

The system behavior is studied under severe weather and load changes. Simulated PV power and area load profiles are given in Fig. 4.16. Changing load profiles include loads ramping up and down in order of 10% and 20%, as shown in Fig. 4.16. The PV power is concurrently varied in maximum order of 80% with the load changes. The AGC is tested with PV power predictions (30s
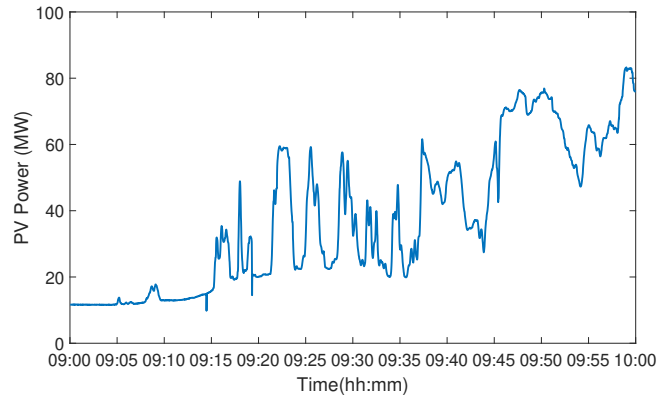
Figure 4.4: (a) PV power observed when PV power increases from 0 MW to 80MW.
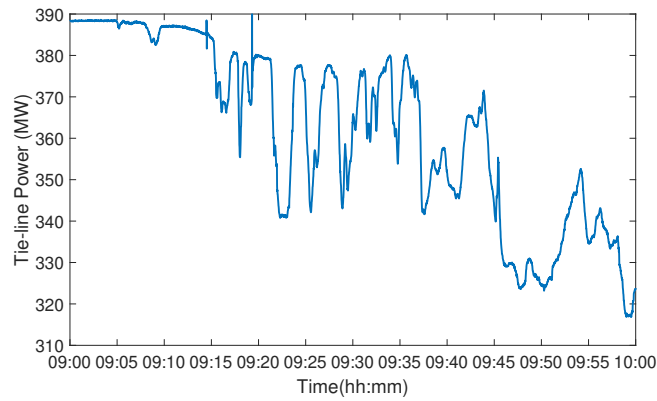
Figure 4.5: (b) Tie-line Power observed when PV power increases from 0 MW to 80MW.
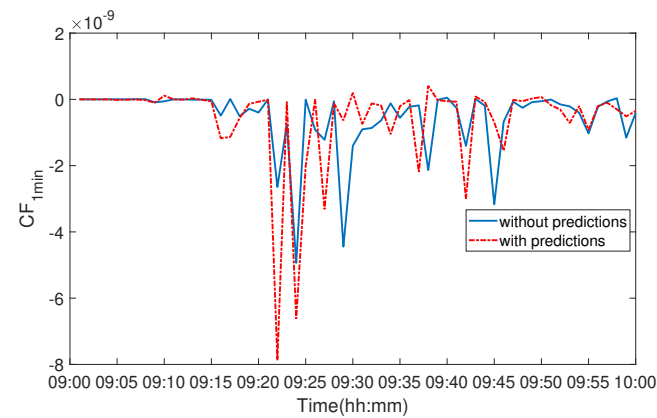
Figure 4.6: (c) CF_{1min} observed when PV power increases from 0 MW to 80MW.
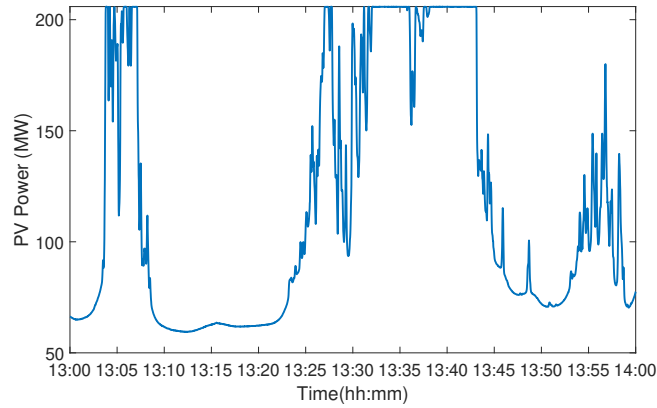
Figure 4.7: (a) PV power observed when PV power decreases from 200 MW to 50MW.
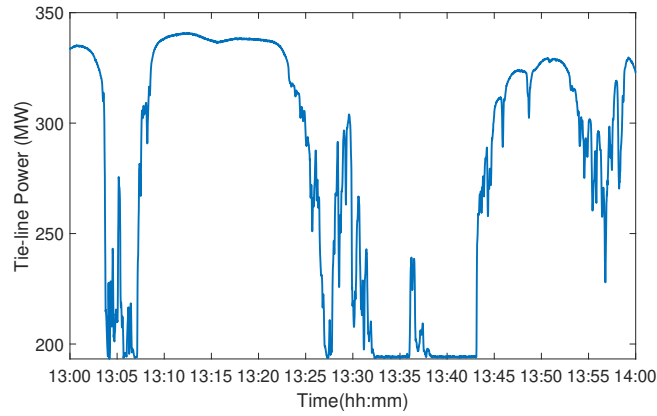
Figure 4.8: (b) Tie-line Power observed when PV power decreases from 200 MW to 50MW.
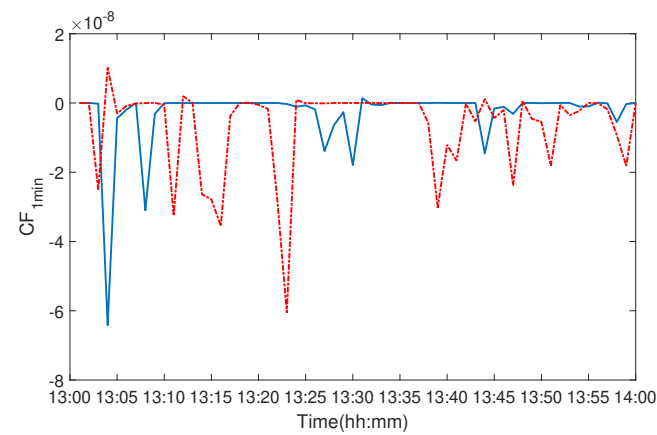
Figure 4.9: (c) CF_{1min} observed when PV power decreases from 200 MW to 50MW.
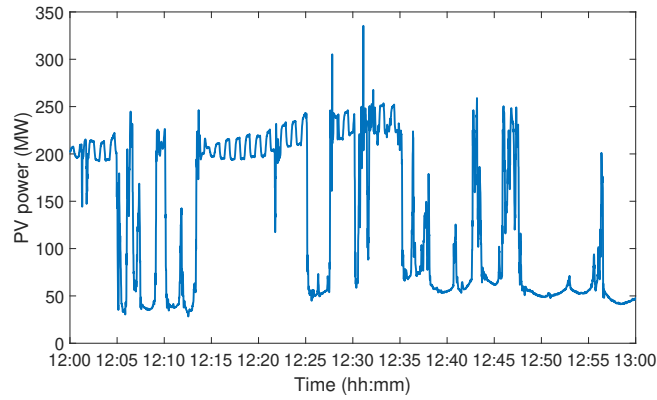
Figure 4.10: (a) PV power observed when PV power decreases from 200 MW to 30MW.
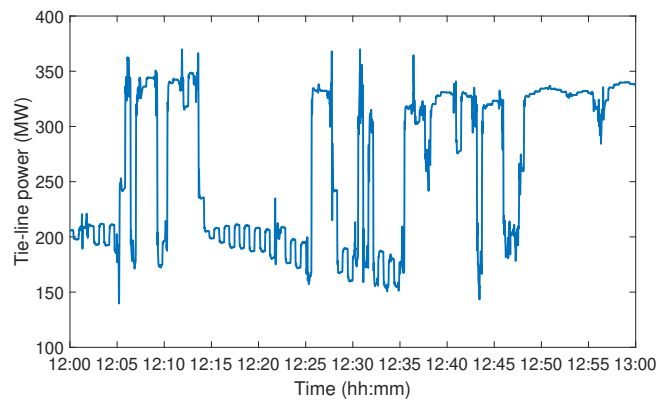
Figure 4.11: (b) Tie-line Power observed when PV power decreases from 200 MW to 30MW.
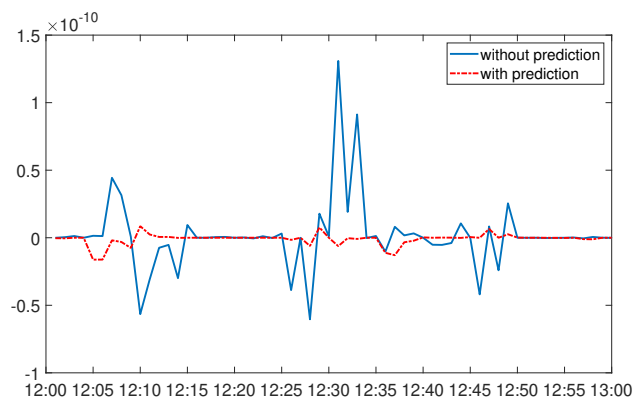
Figure 4.12: (c) CF_{1min} observed when PV power decreases from 200 MW to 30MW.
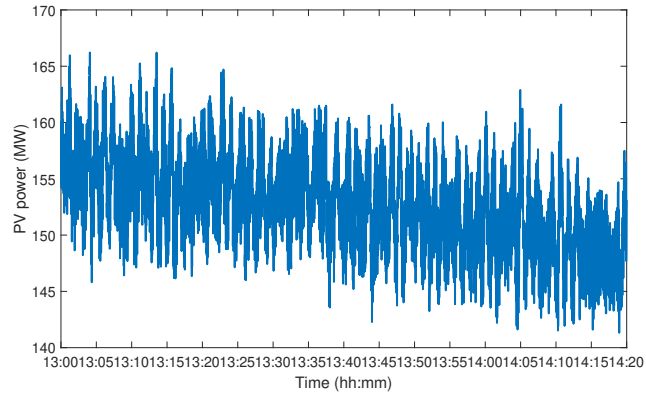
Figure 4.13: (a) PV power observed when PV power increases from 160 MW to 140MW.
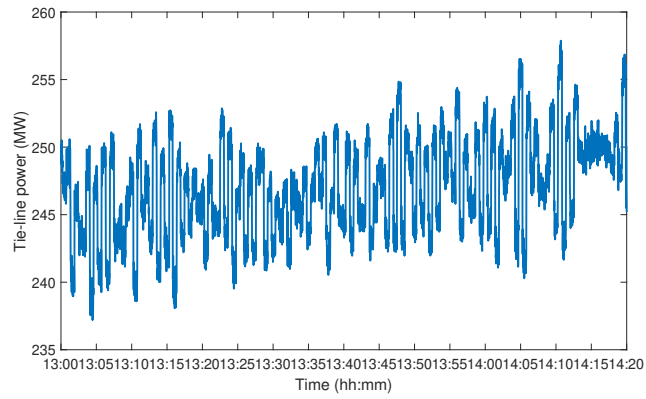
Figure 4.14: (b) Tie-line Power observed when PV power increases from 160 MW to 140MW.
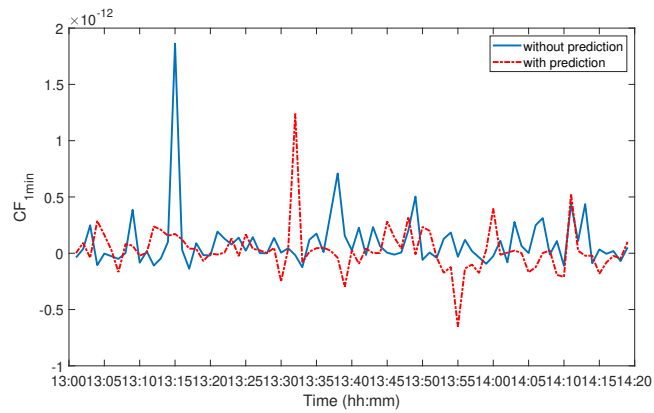
Figure 4.15: (c) CF_{1min} observed when PV power increases from 160 MW to 140MW.
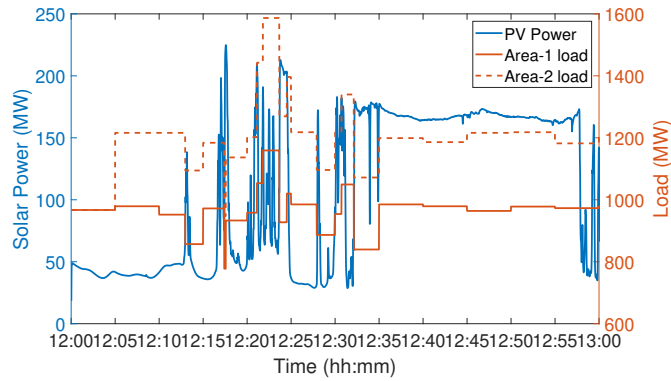
Figure 4.16: (a) PV power, Area-1 load and Area-2 load profiles observed under load changes with variable weather.
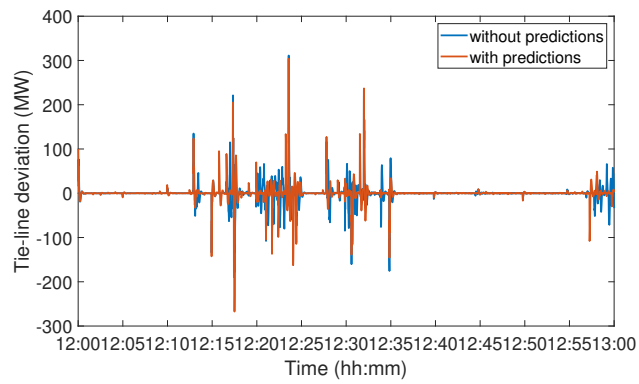
Figure 4.17: (b) Tie-line Power observed under load changes with variable weather.
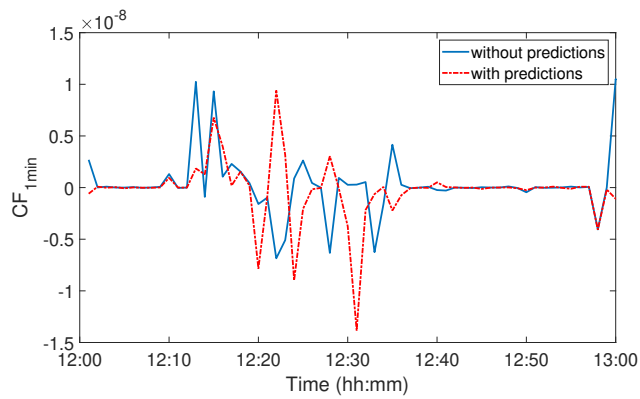
Figure 4.18: (c) CF_{1min} observed under load changes with variable weather.

77

Table 4.1: Performance Comparison Under Variable Weather Conditions

Metric		PV Change Level							
		0 - 80 MW		200 - 50 MW		200 - 30 MW		160-140 MW	
		Without Predictions	With Predictions	Without Predictions	With Predictions	Without Predictions	With Predictions	Without Predictions	With Predictions
CF_{1min}	Positive	10	09	20	17	51	41	51	48
count	Negative	49	50	39	42	38	48	28	31
Accumulated CF_{1min}		-3.3097×10^{-8}	-3.5712×10^{-8}	-5.0545×10^{-7}	-5.7360×10^{-7}	1.4248×10^{-10}	-6.8486×10^{-11}	7.6731×10^{-12}	2.3734×10^{-12}
$CPS1(\%)$		200.0290	200.0313	200.1556	200.3472	199.9999	200.0001	200.0000	200.0000
$CPS2_{10min}(\%)$		100	100	100	100	100	100	100	100
$CPS2_{4s}(\%)$		100	100	100	100	100	100	100	100
$CPS2_{1s}(\%)$		100	100	100	100	100	100	100	100
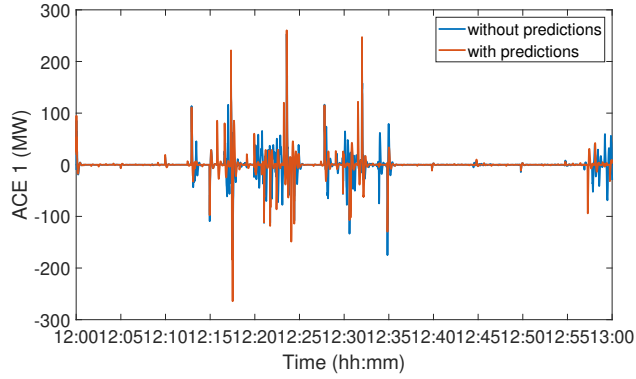
Figure 4.19: (d) ACE observed under load changes with variable weather.

ahead and 4s ahead) and 1s ahead Area-1 frequency predictions. AGC performance with prediction cases are compared with that of conventional AGC including measured parameters. Obtained performance metrics including positive and negative $CF1_{min}$ counts, accumulated $CF1_{min}$, $CPS1$, $CPS2$ and total violated ACE values are given in Table 4.2. Two main test cases are considered, Area-1 load changes with concurrently changing PV power generation and Both Area-1 and Area-2 loads change with concurrently changing PV power. Better performances are observed for AGC with 30s ahead PV power predictions and 1s ahead bus frequency predictions for both test cases. The comparison of tie-line power flow deviation, $CF1_{min}$, and Area-1 ACEs observed with and without application of predictions are given in Figs. 4.17-4.19. However, 4s ahead PV power predictions does not show any enhanced performance, which justify the importance of selecting optimal prediction time step. Although the $CPS2_{10min}$ is 100% for all the scenarios, $CPS2_{4s}$, $CPS2_{1s}$ and total violated ACE counts show better values for the AGC with optimal prediction time step. Higher

ACE values are expected with the non-confirming load changes. Fig. 4.20 shows an over-frequency condition caused by load decreasing concurrently with PV power increasing (tie-line power flow is decreased). Fig. 4.21 shows an under-frequency condition caused by load increasing concurrently with PV power decreasing (tie-line power flow is increased). The improvements in tie-line power flow deviation, frequency deviations and ACEs observed with predictions at these scenarios as shown in Figs. 4.20 and 4.21.

Table 4.2: PERFORMANCE COMPARISON UNDER WEATHER AND LOAD CHANGES.

Metric		Area-1 Load Change		Area-1 and Area-2 Load Change		
		Without Predictions	With Predictions $(\Delta t_{pv} = 30s)$ $(\Delta t_{freq} = 1s)$	Without Predictions	With Predictions $(\Delta t_{pv} = 30s)$ $\Delta t_{freq} = 1s)$	With Predictions $(\Delta t_{pv} = 4s)$ $(\Delta t_{pv} = 4s)$
CF_{1min}	Positive	37	27	41	31	38
count	Negative	24	34	20	30	23
Accumulated CF_{1min}		0.1495 $\times 10^{-7}$	-0.1678 $\times 10^{-7}$	0.1261 $\times 10^{-6}$	0.0972 $\times 10^{-6}$	0.3070 $\times 10^{-6}$
$CPS1(\%)$		199.9869	200.0147	199.8895	199.9149	199.7311
$CPS2_{10min}(\%)$		100	100	100	100	100
$CPS2_{4s}(\%)$		91	94	91	94	91
$total-violated_{ACE_{4s}}$		79	51	78	52	79
$CPS2_{1s}(\%)$		91	95	92	95	91
$total-violated_{ACE_{1s}}$		304	174	298	170	311

4.3.1.3 The "Great American Eclipse" of August 21st, 2017

The system resiliency is also analyzed with weather data observed on the Great American Eclipse of August $21^{st}, 2017$. PV power generation, tie-line power flow and calculated CF_{1min} with and without predictions are shown in Fig. 4.24. Positive and negative $CF1_{min}$ counts, Accumulated $CF1_{min}$, $CPS1$ and $CPS2$ values are given in Table 4.3. Similar results are observed as in variable weather conditions described), indicating improvements under predictions. However, long term application of prediction algorithm can guarantee higher percentage of accuracy.

4.3.2 Resilience to Denial of Service (DoS) Attacks

The dedicated synchrophasor network studied in this study consists of security gateways and VPNs, eliminates many vulnerabilities but still vulnerable to denial of service (DoS) attacks.
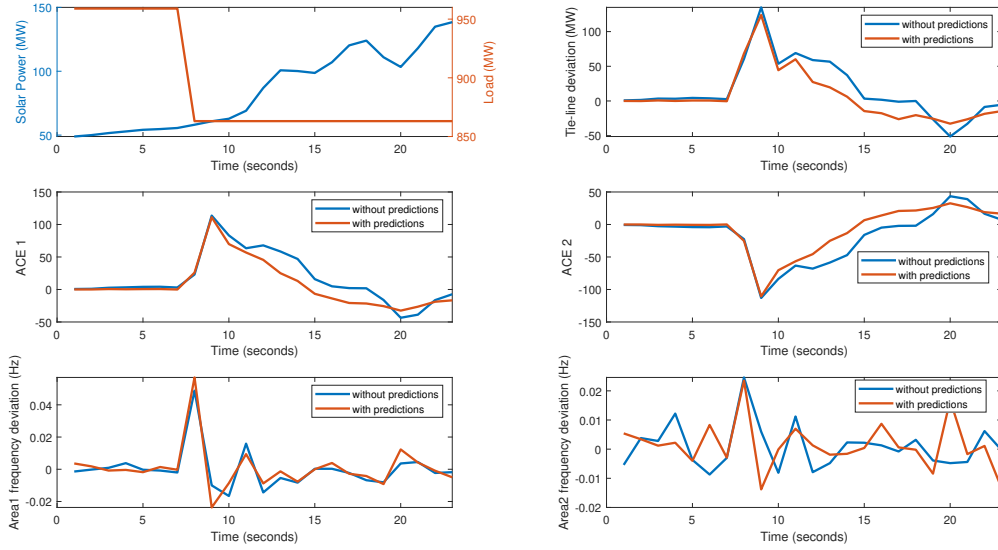
Figure 4.20: (a) PV power, (b) Tie-line Power deviation, (c)Area-1 ACE, (d) Area-2 ACE, (e) Area-1 frequency deviation and (f) Area-2 frequency deviation observed when load is reduced by 20% and PV power increased by 50%.
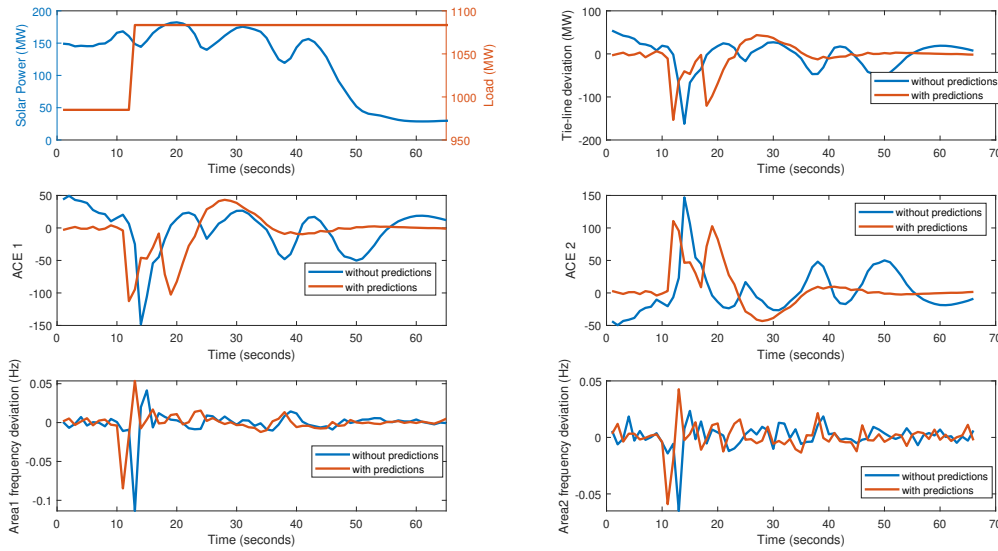
Figure 4.21: (a) PV power, (b) Tie-line Power deviation, (c)Area-1 ACE, (d) Area-2 ACE, (e) Area-1 frequency deviation and (f) Area-2 frequency deviation observed when load is increased by 20% and PV power decreased by 50%.
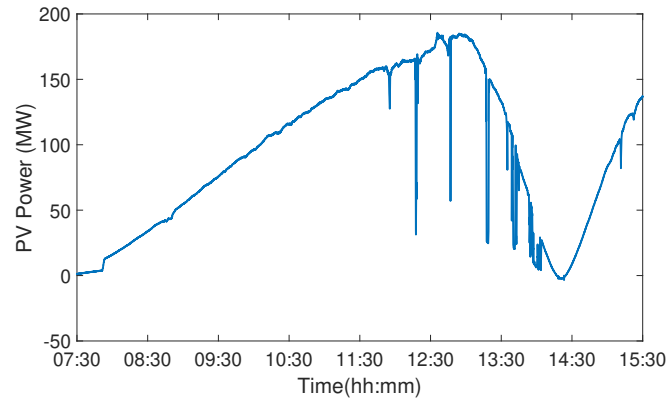
Figure 4.22: (a) PV power observed on the Great American Eclipse of August $21^{st}, 2017$.
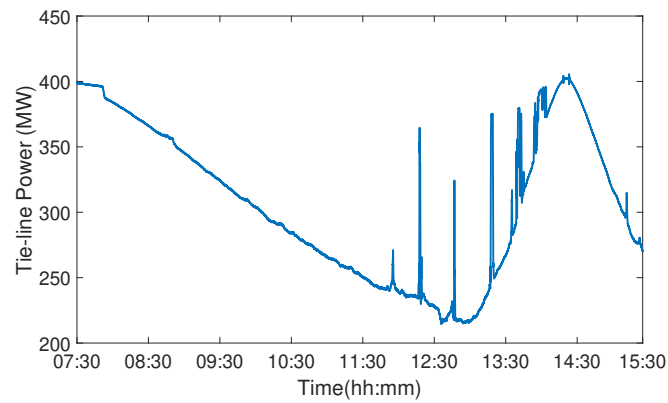
Figure 4.23: (b) Tie-line Power observed on the Great American Eclipse of August $21^{st}, 2017$.
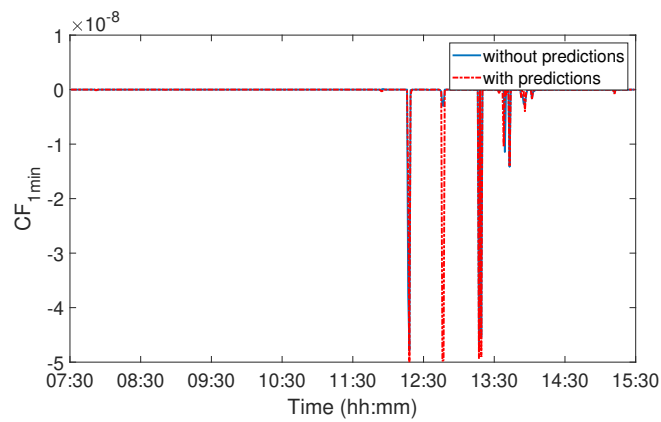
Figure 4.24: (c) CF_{1min} observed on the Great American Eclipse of August $21^{st}, 2017$.

Table 4.3: PERFORMANCE COMPARISON UNDER ECLIPSE DAY WEATHER CONDITIONS.

Metric		Without Predictions	With Predictions
CF_{1min} count	Positive	68	61
	Negative	411	418
Accumulated CF_{1min}		-2.5030×10^{-7}	-2.8739×10^{-7}
$CPS1(\%)$		200.2391	200.2522
$CPS2_{10min}(\%)$		100	100
$CPS2_{4s}(\%)$		100	100
$CPS2_{1s}(\%)$		100	100

Table 4.4: CCESN BASED FREQUENCY PREDICTION PERFORMANCE UNDER DoS ATTACK.

Accuracy Measure	Bus 7 is Attacked			Bus7 and Bus 6 are Attacked			Bus7, Bus 6, and Bus 8 are Attacked		
	Bus7	Bus 6	Bus 8	Bus7	Bus 6	Bus 8	Bus7	Bus 6	Bus 8
$SF(\%)$	85	97	94	84	84	94	68	-10	51
$MAPE(\%)$	1.30×10^{-03}	7.37×10^{-04}	9.68×10^{-04}	1.5×10^{-03}	1.28×10^{-03}	9.03×10^{-04}	2.57×10^{-03}	5.29×10^{-03}	2.94×10^{-03}

Therefore, the proposed resilient and sustainable tie-line bias control is analyzed under DoS attacks performed on the primary PMU of the system (PMU at Bus 7), on PMUs at Buses 6 and 7, and on PMUs at Buses 6, 7 and 8, where Buses 6 and 8 are the neighbors of Bus 7.

4.3.2.1 DoS attack detection

Table 4.5: PERFORMANCE COMPARISON UNDER DoS ATTACK

Metric		Scenario 2 Blocked PMU 7	Countermeasure A Blocked PMU 7	Countermeasure B Blocked PMU 7	Countermeasure C		
					Blocked PMU 7	Blocked PMUs 6,7	Blocked PMUs 6, 7, 8
CF_{1min} count	Positive	29	37	37	26	30	29
	Negative	32	24	24	35	32	34
Accumulated CF_{1min}		6.67	0.6866×10^{-7}	0.1043×10^{-6}	0.1008×10^{-6}	0.1030×10^{-6}	0.1043×10^{-6}
$CPS1(\%)$		-5.8458e+06	199.9399	199.9086	199.9117	199.9097	199.9086
$CPS2_{10min}(\%)$		100	100	100	100	100	100
$CPS2_{4s}(\%)$		0.64	91	91	95	94	94
$total-violated_{ACE_{4s}}$		918	79	83	47	50	46
$CPS2_{1s}(\%)$		0.67	91	92	95	95	95
$total-violated_{ACE_{1s}}$		3674	313	297	170	172	175

In OpenPDC, the time required to arrive all the data for a particular time frame is measured by a parameter called Lag Time (δt). If the measurements are expected but not received within

the δt time window, the OpenPDC recognizes these measurements as missing/delayed data. These missing data positions are filled in order to keep the format of the aligned data packet fixed. A flag in the aligned data packet is set to indicate the data is invalid [86]. The missing data positions are often set to zeros. When a DoS attack is performed, that is when the attacker drops all measurement data from a PMU without interrupting the connection, PMU measurement packets are not delivered to PDC within the expected time window (Lag Time (δt)). The PDC set the invalid flag for the aligned data packet and send zeros instead of missing measurements.

4.3.2.2 Countermeasures

In this study, PMU 7 located at Bus 7 (Fig. 1), is used to provide frequency measurement ($f_7(t)$) to the AGC in Area-1, which is the primary PMU of the system. Flow chart for the possible scenarios during a DoS attack on PMU 7 is given in Fig. 4.1, Denial of Service Attack Countermeasures layer. At each time step t, the PDC waits for δt time window until the PMU measurements are arrived. Then at $t + \delta t$, PMU packet flag status is checked to detect if there is an attack. Based on the flag status, multiple test scenarios are performed [36].

- Scenario 1 : If the packet is arrived at $t + \delta t$, set the flag $= 0$ and the measured value $f_7(t)$ is sent to AGC control

- Scenario 2: If the packet is not arrived $t + \delta t$, set the flag $= 0$ and the PDC filled data value (typically 0) is sent to AGC control

- Scenario 3: If the packet is not arrived $t + \delta t$, set the flag $= 1$ and countermeasure A (Last received valid data point) is sent to AGC control

- Scenario 4: If the packet is not arrived $t+\delta t$, set the flag $= 2$ and countermeasure B (Estimated frequency $\hat{f_7}(t)$) is sent to AGC control

- Scenario 5: If the packet is not arrived $t + \delta t$, set the flag $= 3$ and countermeasure C (CCESN based VSN predicted frequency $\hat{f_7(t + \Delta t)}$) is sent to AGC control

Scenarios for flag $= 0$, 1, 2 (normal condition, countermeasure A and countermeasure B) have been discussed in [36]. In this study, flag $= 3$ (countermeasure C) scenario is introduced.

83
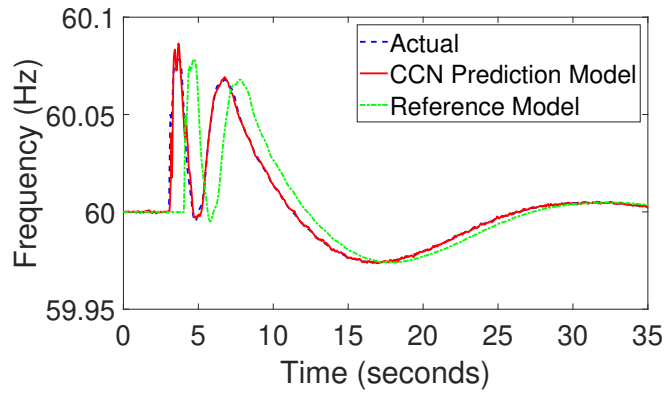
Figure 4.25: Actual, CCN predicted, and reference model frequencies at Bus 6 when PMU at Bus 7 is under attack
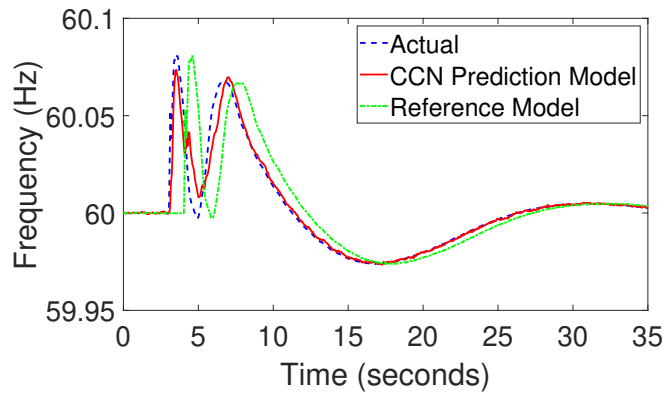
Figure 4.26: Actual, CCN predicted, and reference model frequencies at Bus 7 when PMU at Bus 7 is under attack.
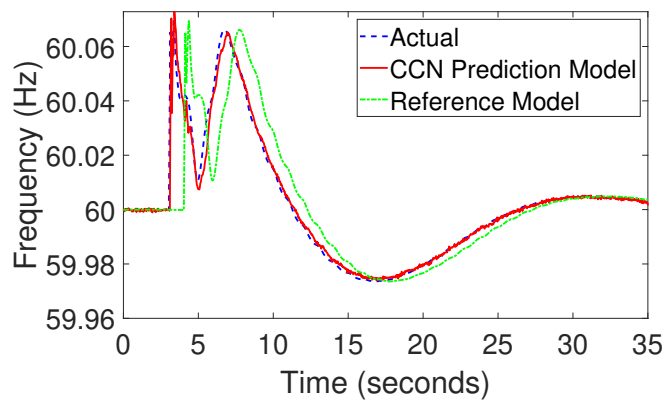
Figure 4.27: Actual, CCN predicted, and reference model frequencies at Bus 8 when PMU at Bus 7 is under attack.
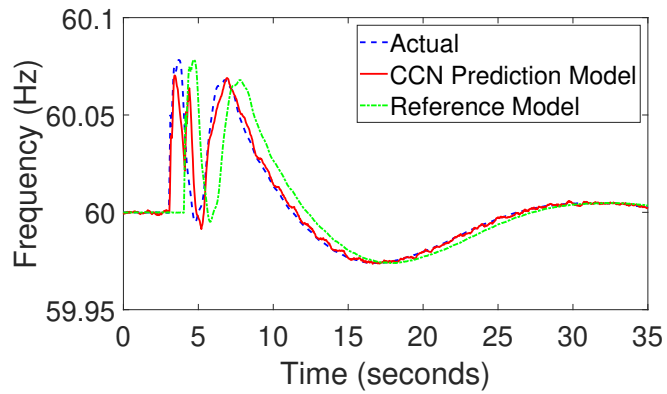
Figure 4.28: Actual, CCN predicted, and reference model frequencies at Bus 6 when PMUs at Bus 7 and Bus 6 are under attack.
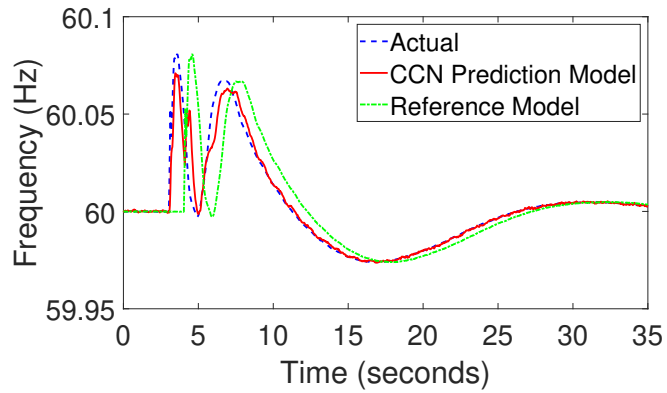
Figure 4.29: Actual, CCN predicted, and reference model frequencies at Bus 7 when PMUs at Bus 7 and Bus 6 are under attack.
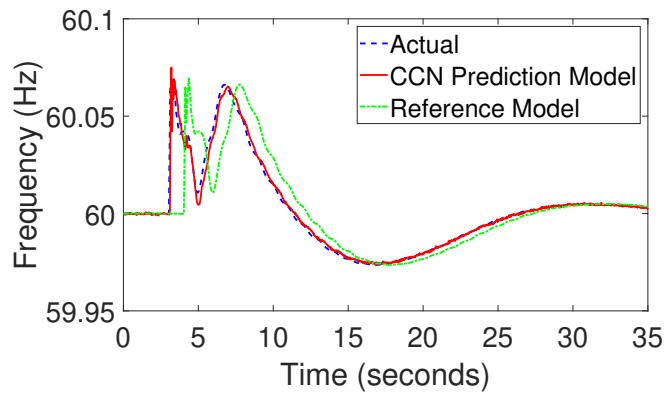
Figure 4.30: Actual, CCN predicted, and reference model frequencies at Bus 8 when PMUs at Bus 7 and Bus 6 are under attack.
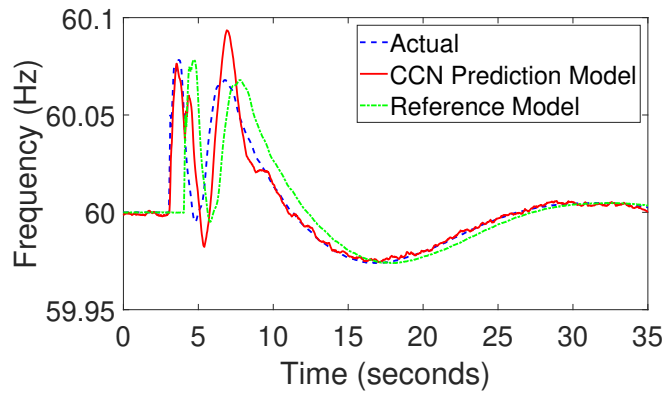
Figure 4.31: Actual, CCN predicted, and reference model frequencies at Bus 6 when PMUs at Bus 6, Bus 7 and Bus 8 are under attack.
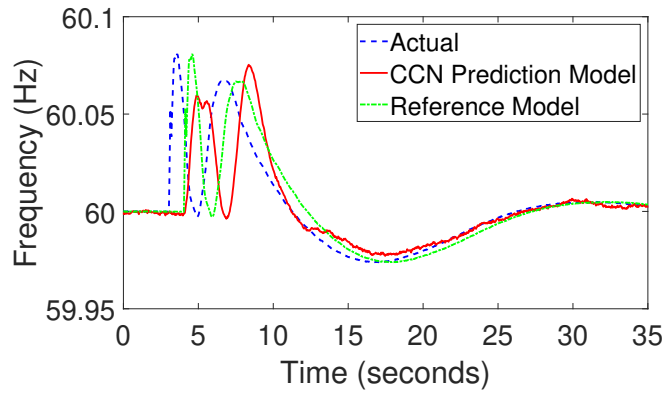
Figure 4.32: Actual, CCN predicted, and reference model frequencies at Bus 7 when PMUs at Bus 6, Bus 7 and Bus 8 are under attack.
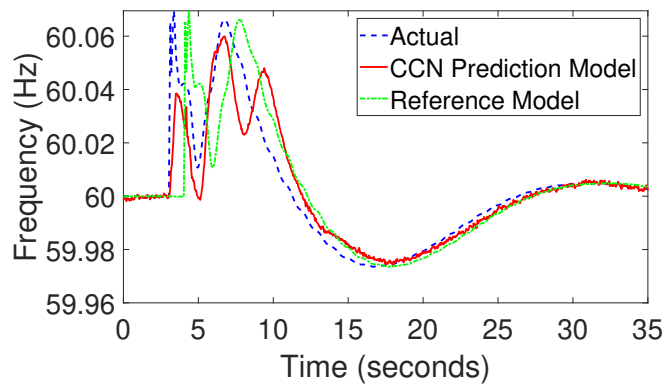
Figure 4.33: Actual, CCN predicted, and reference model frequencies at Bus 8 when PMUs at Bus 6, Bus 7 and Bus 8 are under attack.

4.3.2.3   Multiple DoS Attacks

According to the topology of the power system (Fig. 4.1), Bus 6 and 8 are the neighboring cells of the Bus 7. CCESN based frequency prediction results observed when Bus 7 PMU is attacked, when both Bus 7 and Bus 6 PMUs are attacked, when all three PMUs (Bus 6, 7 and 8) are attacked are given in Figs. 4.27, 4.30, and 4.33 respectively. Prediction accuracy measures are presented in Table 4.4. A three phase-to-ground fault is performed at Bus 8 (the tie-line power connecting Bus) while PMUs (at Bus 7, Bus 6, and Bus 8) are blocked. According to the Figs. 4.27-4.33 and Table 4.4, VSN provides good prediction results although the neighboring cell PMUs are blocked. Frequency measurements among neighboring cells are related due to the network topology. Therefore, VSN cells can use neighboring PMU measurements to approximate missing data. However, prediction accuracies are degrading when the number of dropped PMU count is increased. However, it is still possible to use the predicted frequencies for AGC operation. Tie-line bias control performance is analyzed under DoS attacks with the weather and load profiles given in Fig. 4.16. PMUs are blocked around 12:13, where PV power is increased from 50 MW to 150 MW and area loads are decreased by 10%. Performance metrics calculated are given in Table 4.5. A negative $CPS1$ value is observed for Scenario 2, indicating the system vulnerability to DoS attack. Scenarios 3 and 4 (with countermeasures A and B respectively) shows better $CPS1$ values, however the $CPS2_{4s}$ and $CPS2_{1s}$ values are low for both cases compared to scenario 5 (countermeasure C). Lower $total-violated_{ACE_{4s}}$ and $total-violated_{ACE_{1s}}$ values are observed for countermeasure C compared countermeasures A and B. Three cases under countermeasure C include when PMU 7 is attacked, when PMUs 6 and 7 are attacked, and when PMUs 6, 7, and 8 are attacked. Improved $CPS1$, $CPS2$ and total violated ACE values are illustrated with countermeasure C. However, the AGC performance is dropped with the increasing number of PMUs are under attack. This is due to the degrading accuracy of the VSN predictions.

4.4   Summary

Interconnected power systems with large-scale penetration of photovoltaic (PV) power introduce frequency and tieline power flow fluctuations. This is due to the variability and uncertainty characteristics of PV power. This makes automatic generation control (AGC) to be more challenging. In this study, an enhanced tie-line bias control method is proposed by predicting PV power

generation and bus frequencies. A cyber-physical two-area power system with a large PV plant consisting of phasor measurement units (PMUs) is studied. The use of synchrophasor networks consisting of PMUs can enable smooth power system operations overcoming the challenges of PV power variability and uncertainty. However, the use of PMUs in power system control creates vulnerabilities for cyber-attacks that could jeopardize the power system operations. It is shown that the frequency prediction using a virtual synchrophasor network (VSN) can mitigate the impact(s) of denial of service (DoS) attacks on physical PMUs. Enhanced AGC performance is investigated under different weather and load conditions including a weather profile during the "Great American Eclipse" of August 21st, 2017. Typical results indicate that the enhanced AGC structure provides a resilient and sustainable tie-line bias control in uncertain environments.

A faster method to solve security-constrained optimal power flow problem (SCOPF) is presented in next section.

Chapter 5

Distributed and Parallel Security-Constrained Optimal Power Flow

5.1 Introduction

Modern electrical power grid faces major challenges with the increasing penetration levels of renewable energy. It is necessary to have robust operating and control strategies to address the uncertainties introduced by the intermittency of renewable energy sources [87]. The requirements for resolving challenges in avoiding cascading failures, maintaining network robustness and resiliency are imperative. Additionally, the need for coordinating energy resources in a distributed manner is necessary[88]. The security constrained optimal power flow (SCOPF) problem aims to balance the security and the economic requirements of the power system by optimizing the system operating state with security constraints. The method is an effective tool for the online operation and offline planning of power system. The current centralized coordination strategies of solving SCOPF problem are incapable of addressing challenges introduced by the evolving grid. Therefore, more accurate, faster and distributed SCOPF problem solving approaches must be introduced to overcome these challenges.

The SCOPF is a non-convex problem to solve and has been proven to be in NP-hard [89].

The problem is made worse since the practical power grid SCOPF problem involves tens of thousands of variables. To solve a problem of this scale, the maximum utilization of available computational power is necessary.

Modern computing power, on the other hand, largely depends on the expansion of distributed and parallel processing capabilities much more than the improvement of the individual processing element itself[90]. Cheap parallel hardware devices such as general purpose graphics processing units (GPGPUs) are currently commercially available for common use. At the same time, the current electric power grid is expanding as a distributed control structure with the integration of distributed energy sources. The distributed architecture provides easy maintenance, high software and hardware performance as compared to a centralised control architecture [90]. In this study, a distributed and parallel SCOPF (DP-SCOPF) method is proposed that could achieve the task by breaking down the problem in to manageable pieces.

Several methods of efficient optimization of moderate and large scale OPF/SCOPF have been proposed in literature. Relaxation based SCOPF solving approaches have been studied in [91, 92]. Convex relaxation simplifies the non-convex optimization problem, but does not guarantee the solution for the original problem. Several distributed and parallel methods have been introduced by decomposing the power network in to manageable components. An accelerated parallel SCOPF method is presented in [93] by using GPU programming. The alternating direction method of multipliers (ADMM) have been suggested to solve alternating current optimal power flow (ACOPF) and SCOPF problems in [94, 95, 96]. Although ADMM addresses the large scale SCOPF problem, a central coordination of the sub problems is required for the update of the multipliers. A Bender's decomposition method is suggested for OPF in [97]. Benders decomposition facilitates parallel computing by decomposing the problem into a master problem corresponding to normal operation and sub problems, each corresponding to a contingency case. A similar decomposition method is presented in [98] to solve the contingencies in SCOPF problem. An innovation based distributed SCOPF method is proposed in [88] for direct current optimal power flow (DCOPF) problem. Although these research introduce various distributed and parallel methods of optimization by decomposing the network into regions/clusters, the dividing criteria themselves are not that often discussed. However, the selection of regions/clusters could severely hinder or support the algorithm converging to a good solution. Optimization of active/reactive power generation is a challenging task with the availability of generators within clusters. Primary contributions of this study are

- A robust clustering method for SCOPF is presented. The method creates clusters with highly connected power system buses and few boundary branches as possible to assure less complexity and less computational time.

- The distributed and parallel SCOPF (DP-SCOPF) method provides more accurate solutions during normal and contingency operations.

- The DP-SCOPF method is capable of providing solutions for online and offline operations on real-world power systems.

5.2   The SCOPF Problem Formulation

The objectives of SCOPF problem include determining optimal operating parameters $(v_i, \theta_i, p_g, q_g, b_i^{CS})$ such that:

- The power balance and operating constraints of the power system are met while the generator real power output costs are minimized.

- The resulting optimal operating point has to be feasible after any single outage in the power system (N-1 security constraints).

The problem needs to be solved within two time limits, online operation for normal operation including economic dispatch and offline operation for planning and optimization purposes. The problem formulation for the SCOPF problem studied is given in (5.1) [99]. Formulations for active power balance and reactive power balance are given in (5.2) and (5.3) respectively. Line apparent

power limit constraints are given in (5.4) - (5.5). Variable limit constraints are given in (5.6) - (5.9).

$$\min_{v_i, \theta_i, p_g, q_g, b_i^{CS}} \sum_{g \in G} f(p_g) \tag{5.1}$$

subject to

$$\sum_{g \in G_i} p_g - p_i^L - g_i^{FS} v_i^2 - \sum_{e \in E_i^o} p_e^o - \sum_{e \in E_i^d} p_e^d = 0 \tag{5.2}$$

$$\sum_{g \in G_i} q_g - q_i^L - (b_i^{FS} - b_i^{CS}) v_i^2 - \sum_{e \in E_i^o} q_e^o - \sum_{e \in E_i^d} q_e^d = 0 \tag{5.3}$$

$$\sqrt{(p_e^o)^2 + (q_e^o)^2} \leq \overline{s_e}, \tag{5.4}$$

$$\sqrt{(p_e^d)^2 + (q_e^d)^2} \leq \overline{s_e}, \tag{5.5}$$

$$\underline{v_i} \leq v_i \leq \overline{v_i} \quad \forall v \in I \tag{5.6}$$

$$\underline{p_g} \leq p_g \leq \overline{p_g} \quad \forall g \in G \tag{5.7}$$

$$\underline{q_g} \leq q_g \leq \overline{q_g} \quad \forall g \in G \tag{5.8}$$

$$\underline{b_i^{CS}} \leq b_i^{CS} \leq \overline{b_i^{CS}} \quad \forall i \in I \tag{5.9}$$

where I is the set of buses, G is the set of generators, E is the set of lines, $i \in I$ is the bus indices, $g \in G$ is the generator indices, $e \in E$ is the line indices, $G_i \subset G$ is the G generators connected to bus i, p_i^L is the bus i constant real power load, g_i^{FS} is the bus i fixed shunt conductance, v_i is the bus i voltage magnitude, q_i^L is the bus i constant reactive power load, b_i^{FS} is the bus i fixed shunt susceptance, b_i^{CS} is the bus i maximum controllable shunt susceptance, q_e^o is the line e reactive power from origin bus into line, q_e^d is the line e reactive power from destination bus into line, $\overline{s_e}$ is the line e apparent power maximum, p_g is the generator g real power output, $E_i^d \in E$ is the lines with destination bus i, $E_i^o \in E$ is the lines with origin bus i, $\overline{v_i}$ is the bus i voltage magnitude maximum in the base case, $\underline{v_i}$ is the bus i voltage magnitude minimum in the base case, $\overline{p_g}$ is the generator g real power maximum , $\underline{p_g}$ is the generator g real power maximum, $\overline{q_g}$ is the generator g reactive power maximum, $\underline{q_g}$ is the generator g reactive power maximum, $\overline{b_i^{CS}}$ is the bus i maximum controllable shunt susceptance, $\underline{b_i^{CS}}$ is the bus i minimum controllable shunt susceptance and θ_i is the bus i voltage angle.

5.3   Distributed and Parallel SCOPF (DP-SCOPF)

The complete DP-SCOPF algorithm is given in Fig. 5.2. Basic steps of the algorithm are described in following sub sections.

5.3.1   Initialize Parameters

In this step, inner and outer iterations, time limit for the optimization (offline or online) are initialized. v_i is initialized to 1.00.

5.3.2   DCOPF

One approach of solving non-linear non-convex types of optimization problems is linear approximation of equations [100]. Direct-Current optimal power flow (DCOPF) provides a linear approximation to the SCOPF problem defined in (5.1) [101]. In this study, DCOPF solved solution is applied as the initial point of the Algorithm. In DCOPF, it is assumed that the v_i is nearly equal to 1.00, the difference between voltage angles $(\theta_i^o - \theta_i^d)$ is very small (≈ 0.0), and the branch resistance is very small compared to reactance ($g << b$). Based on these assumptions problem in (5.1) is simplified to the problem formulation given in (5.10). The objective is to minimize the active power generation cost and soft constraint variables subject to active power balance (5.11), line rating limit constraints for active power (5.13) and (5.14) and active power limits (5.25).

$$\theta_i, p_g \sum_{g \in G} f(p_g) + \lambda \sum_{e \in E} \sigma_e^s \tag{5.10}$$

subject to

$$\sum_{g \in G} p_g = \sum_{i \in I} p_i^L \tag{5.11}$$

$$p_e = -b_e(\theta_{i_e}^o - \theta_{i_e}^d) \tag{5.12}$$

$$p_e \leq \overline{s_e} + \sigma_e^s, \sigma_e^s \geq 0 \tag{5.13}$$

$$-p_e \leq \overline{s_e} + \sigma_e^s, \sigma_e^s \geq 0 \tag{5.14}$$

$$\underline{p_g} \leq p_g \leq \overline{p_g} \ \ \forall g \in G \tag{5.15}$$

where $f(.)$ is the modeling function for generator real power output costs, σ_e^s is the soft constraint for line rating violations, b_e is the line e series susceptance, $_e^o \in I$ is the origin bus of line e and $i_e^d \in I$ is the destination bus of line e.

Initial voltage angles (θ_i) and active power generations (p_g) are set to values obtained from DCOPF $(\theta_{iDCOPF}$ and $p_{gDCOPF})$ before the next step. Reactive power (q_g) and variable shunt (b^{CS}) values are calculated from (5.3).

5.3.3 Clustering for Optimization

In this study, network clusters are obtained using a spectral clustering algorithm [102]. The method uses graph Laplacian matrix, which is calculated using the adjacency matrix and the degree matrix of the power network when the power network is represented as a graph. Eigenvalues and eigenvectors of the Laplacian matrix provide the information on local neighborhood relationships between nodes such as connected component density and minimum graph cut. Therefore, the method is capable of providing dense uniform clusters with few boundary branches. The spectral clustering algorithm is illustrated in Algorithm 2. The clusters generated for IEEE 14 bus power system is given in Fig. 5.1. MATLAB implemented spectral clustering algorithm is utilized to generate clusters.

Algorithm 2: Spectral Clustering

Result: The assignment of $i \in I$ to the C clusters

Pre-processing

    1. construct Laplacian Matrix;

Decomposition

    1. compute eigenvalues and the eigenvectors of the matrix;

    2. map each point to a lower-dimensional representation based on one or more eigenvectros;

Grouping

    1. assign points to clusters based on the new representation;

Distributed and parallel capabilities of the DP-SCOPF algorithm is obtained by decomposing the power network into small clusters and formulating a local SCOPF problem for each cluster through voltage optimization. Network clustering is a key aspect in ensuring the performance of the optimization in the proposed method. Under the best circumstances, compact clusters with very
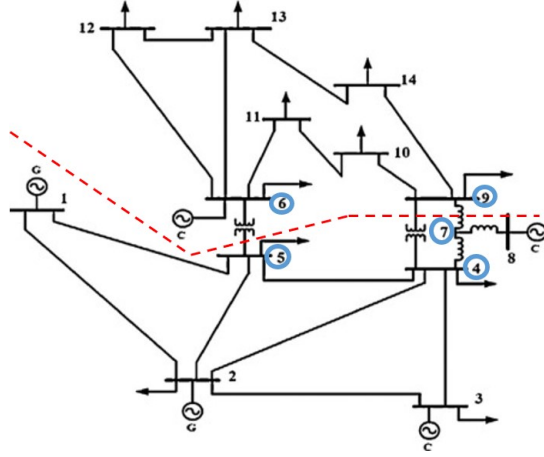
Figure 5.1: IEEE 14 bus system with 2 clusters

few boundary branches assure less complexity, accurate solution and less computational time.

However, the problem formulated in (5.1) is not directly separable. Consider the power system diagram given in Fig.5.1. In Fig. 5.1, IEEE 14 bus power system is divided into two clusters. The buses highlighted in blue represent the connecting buses (or the boundary buses) of the two clusters. The power flows between highlighted buses depend on the values of v_i and θ_i of the corresponding buses, which fall into different clusters. The boundary voltages introduce a coupling constraints in (5.2) and (5.3).

In the distributed and parallel SCOPF optimization approaches introduced in literature, local objective function includes optimization of active/reactive power generation, which is a challenging task with the availability of generators within clusters. In the proposed method, only the voltages (v_i and θ_i) are solved in distributed and parallel manner, where the active/reactive power generation (p_g, q_g) are optimized separately for the entire network as a linear problem formulation.

Consider the total number of clusters in the network is C and $R_c, c = 1, \ldots, K$ denote the set of buses assigned to cluster c with $R_c \cap R_l = \emptyset, \forall c \neq l$. And it is assumed that the average number of buses in each cluster has a uniform size m. To enable the distributed and parallel approach, the buses belong to boundary branches (B_c) are optimized separately from the remaining buses of the cluster c. The optimization is preformed in two-levels such that;

1. Level-1 - optimized $v_i, \theta_i \in \{R_c - B_c\}$ while $v_i, \theta_i \in B_c$ are fixed $\forall c$.

2. Level-2 - optimized $v_i, \theta_i \in \{B_c \cup B_l\}$ while $v_i, \theta_i \in \{R_c - B_c\}$ are fixed $\forall c$.

With this configuration, Level-1 can be processed in a distributed and parallel manner for each cluster c. Similarly, Level-2 can be processed in a distributed and parallel manner since the set of boundary buses ($\{B_c \cup B_l\}$) includes set of disconnected components (boundary clusters) with no dependencies.

5.3.4 Voltage optimization

The problem formulation for the cth cluster is given in (5.16). The objective function includes real power excess/deficit imbalance, reactive power excess/deficit imbalance and line current rating violation soft constraints subject to active power balance (5.17), reactive power balance (**??**), line rating violations (5.19) and (5.20), and voltage limits (5.21).

$$v_i, \theta_i \in \{R_k - B_k\} \lambda \sum_{i \in R_k} (\sigma_i^{P+} + \sigma_i^{P-} + \sigma_i^{Q+} + \sigma_i^{Q-}) + \sum_{e \in E_k, f \in F_k} \sigma_f^s \tag{5.16}$$

subject to

$$\sum_{g \in G_i} p_g - p_i^L - g_i^{FS} v_i^2 - \sum_{e \in E_i^o} p_e^o - \sum_{e \in E_i^d} p_e^d = \sigma_i^{P+} - \sigma_i^{P-}, \text{where } \sigma_i^{P+} \geq 0 \text{ and } \sigma_i^{P-} \geq 0 \ \forall i \in I$$
$$\tag{5.17}$$

$$\sum_{g \in G_i} q_g - q_i^L - (b_i^{FS} - b_i^{CS}) v_i^2 - \sum_{e \in E_i^o} q_e^o - \sum_{e \in E_i^d} q_e^d = \sigma_i^{Q+} - \sigma_i^{Q-}, \text{where } \sigma_i^{Q+} \geq 0 \text{ and} \tag{5.18}$$

$$\sigma_i^{Q-} \geq 0 \ \forall i \in I$$

$$\sqrt{(p_e^o)^2 + (q_e^o)^2} \leq \overline{s_e} + \sigma_e^s, \sigma_e^s \geq 0, \ \ \forall e \in E, \tag{5.19}$$

$$\sqrt{(p_e^d)^2 + (q_e^d)^2} \leq \overline{s_e} + \sigma_e^s, \sigma_e^s \geq 0, \ \ \forall e \in E, \tag{5.20}$$

$$\underline{v_i} \leq v_i \leq \overline{v_i} \ \ \forall v \in I \tag{5.21}$$

where σ_{P+}^i, σ_{P-}^i, σ_{Q+}^i and σ_{Q-}^i are soft constraint violation variables.

The voltage optimization (given in Algorithm 2) is modeled as a recursive algorithm. Separation of clusters can result large number of boundary nodes with large connected boundary clusters. This can cause reduced performance. As a solution, the boundary clusters which exceed the average cluster size (m) are recursively separated into 2nd level clusters and boundaries as given in Algorithm 2.
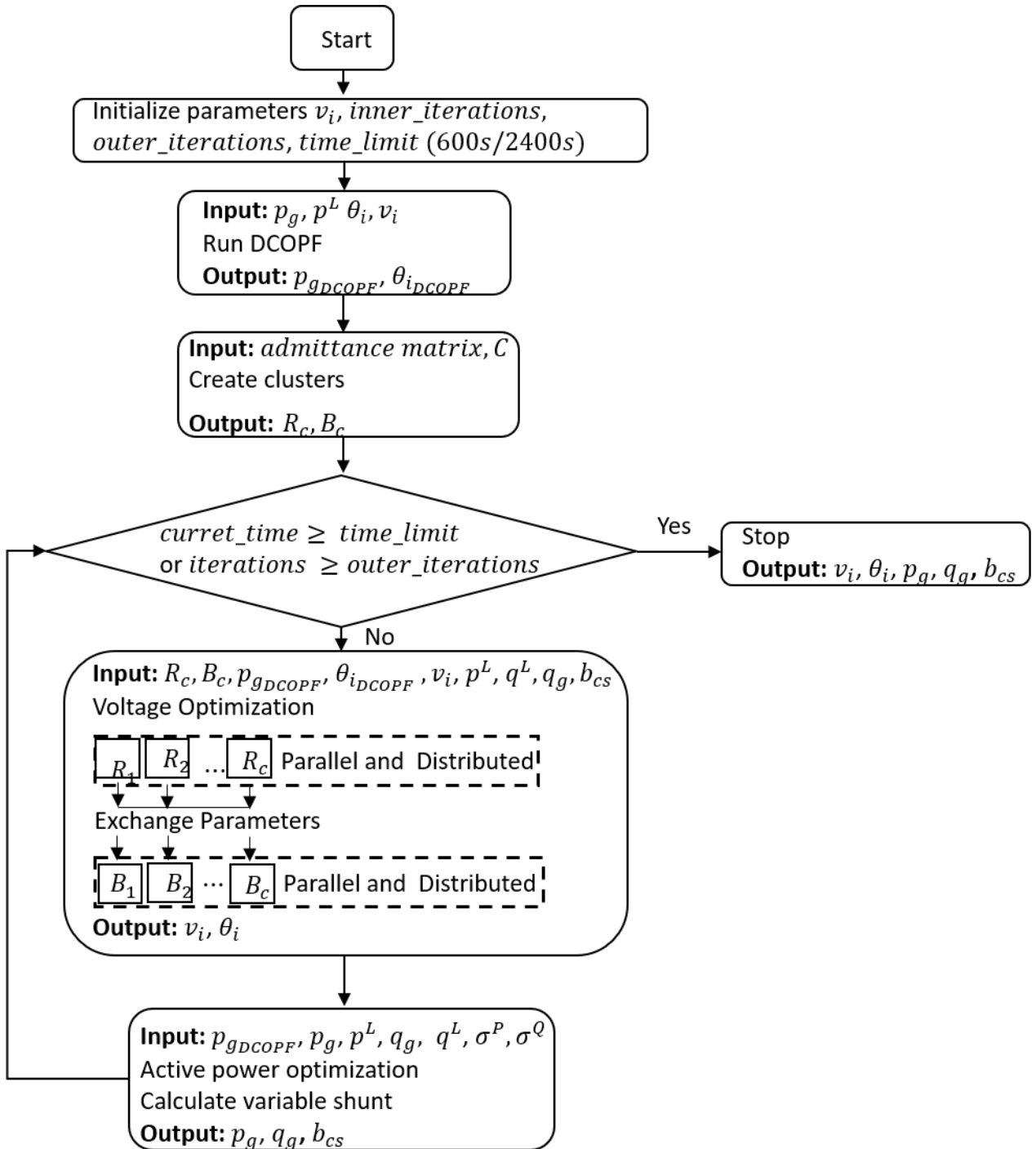
Figure 5.2: DP-SCOPF Algorithm

Algorithm 3: VOLTAGE_OPTIMIZATION

Result: $v_i, \theta_i \in I$
Initialize variables;

   1. Set inner_iterations ;

VOLTAGE_OPTIMIZATION$(v_i, \theta_i \in I)$
  do in parallel for $c = 1, \ldots C$
    while *iterations ¡ inner_iterations* **do**
      Solve (5.16) for R_c ;
      iterations = iterations + 1 ;
    end
  end
  do in parallel for $c = 1, \ldots C$
    if *size(B_c) > m* **then**
      VOLTAGE_OPTIMIZATION$(v_i, \theta_i \in B_c)$;
    end
    else
      while *iterations ¡ inner_iterations* **do**
        Solve (5.16) for B_c ;
        iterations = iterations + 1 ;
      end
    end
  end

5.3.5 Active and Reactive Power Optimization

The problem formulation for the power generation optimization is given in (5.22). The objective is to minimize the difference between p_g and the initial p_g obtained by solving DCOPF while satisfying the active power (5.23), reactive power balance constraints (5.23) and generation limits (5.25) and (5.26). This is a convex optimization process, which is less time consuming, hence solved for the entire network. Finally, controllable shunt (b_i^{CS}) variables are calculated based on the obtained results.

$$p_g, q_g \lambda \sum_{g \in G} (p_g - p_{gDCOPF})^2 \tag{5.22}$$

subject to

$$\sum_{g \in G} p_g = \sum_{i \in I} p_i^L + \sum_{i \in I} (\sigma_i^{P+} - \sigma_i^{P-}) \tag{5.23}$$

$$\sum_{g \in G} q_g = \sum_{i \in I} q_i^L + \sum_{i \in I} (\sigma_i^{Q+} - \sigma_i^{Q+}) \tag{5.24}$$

$$\underline{p_g} \leq p_g \leq \overline{p_g} \ \ \forall g \in G \tag{5.25}$$

$$\underline{q_g} \leq q_g \leq \overline{q_g} \ \ \forall g \in G \tag{5.26}$$

where p_{gDCOPF} is the generator g real power output obtained from DCOPF and θ_{iDCOPF} is the bus i voltage angle obtained from DCOPF.

5.4   Results and Discussion

The proposed method is tested on multiple real-world power systems (given in Table 5.1). Corresponding number of clusters, time taken for the clustering algorithm, cluster sizes and boundary sizes are given in Table 5.1. The performance is measured under two categories, online optimization and offline optimization. All the test cases are executed five times and average values are considered for analysis. All non-linear optimization problems are solved using interior-point optimization method with primal-dual approach. All the linear optimization problems are solved using linear programming optimization method. All the test cases are analyzed on a Intel Xeon computer with 64 GB memory and 8 workers.

5.4.1   Performance Metrics

The optimization algorithm performance is measured using multiple performance metrics. The generators active power output costs are modeled using piece-wise linear tables according to [99] given in (5.27). A weighted sum of soft constraint violation penalties, including penalties on violations of bus active and reactive power balance and penalties on violations of line and transformer apparent current ratings is calculated as given in (5.28). The penalty is given by a piece-wise

Table 5.1: POWER NETWORK DATA

Network	Buses	Gen-erators	Loads	Bran-ches	Trans-formers	Fixed shunts	Variable shunts	No of Clusters	Time (s)	cluster size [mean ± std]	boundary size [mean ± std]
1	500	58	200	463	131	-	13	2	0.4	245±69	2±0
								5	0.4	93±26	5±3
								10	0.4	45±16	7±9
2	793	82	510	769	143	49	50	10	0.5	73±45	3±2
								20	0.5	34±11	3±4
								30	0.5	22±8	5±4
3	2000	432	1125	2337	842	-	150	30	1.3	53±21	7±31
								50	1.5	20±11	8±45
								70	1.6	30±12	7±42
4	3013	865	2836	1290	842	129	405	70	2.9	35±17	5±9
								100	3.1	23±11	10±6
								130	3.5	17±9	7±22
5	4918	1340	3070	4412	2315	246	486	100	6.4	10±14	6±17
								125	6.7	40±16	6±17
								150	7.5	41±16	6±17

linear cost function, where a small penalty price is applied to minor violations followed by a more stringent penalty price for moderate violations and then an extremely severe penalty for all remaining violations.Finally, a combined metric (c) is modeled to measure the combination of cost of generation and the constraint violation penalties in the base case and contingencies given in (5.29).

$$c_g = \sum_{g \in G} f(p_g) \tag{5.27}$$

$$c^\sigma = \sum_{n \in N} [\lambda_n^P \sum_{i \in I} (\sigma_{in}^{P+} + \sigma_{in}^{P-}) + \lambda_n^Q \sum_{i \in I} (\sigma_{in}^{Q+} + \sigma_{in}^{Q-}) + \lambda_n^S \sum_{e \in E} \sigma_{en}^S + \lambda_n^S \sum_{f \in F} \sigma_{fn}^S] \tag{5.28}$$

$$c = \sum_{g \in G} c_g + \delta c^\sigma + (1 - \delta)/|K| \sum_{k \in K} c_k^\sigma \tag{5.29}$$

where $\lambda, \lambda_n^P, \lambda_n^Q, \lambda_n^S$ are pre-set penalty multipliers, c_g is the generator real power output costs, $n \in N$ is the segment number for the piece-wise linear penalty cost function for violations, N is the set of segments in the piece-wise linear penalty cost function for violations, σ_{in}^{P+} is the bus i real power excess violation for segment n in the piece-wise linear penalty cost function, σ_{in}^{P-} is the bus i real power deficit violation for segment n in the piece-wise linear penalty cost function, σ_{in}^{Q+} is the bus i reactive power excess violation for segment n in the piece-wise linear penalty cost function ,
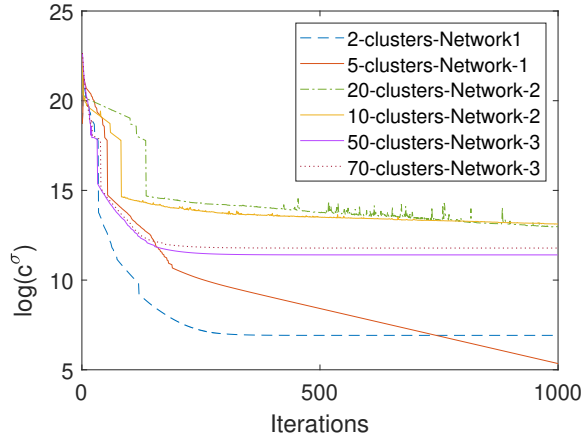
Figure 5.3: c^σ convergence with number of clusters for Networks 1, 2 and 3.

σ_{in}^{Q-} is the bus i reactive power deficit violation for segment n in the piece-wise linear penalty cost function, σ_{en}^{S} is the line e apparent current rating violation for segment n in the piece-wise linear penalty cost function, c^σ is the weighted sum of soft constraint violation penalties, c is the combined metric, δ is the weight in combined metric, k is the contingency and K is the set of contingencies.

5.4.2 Optimization Results

The convergence performance of the proposed method with different number of clusters are illustrated in Fig. 5.3. The number of clusters affect on the algorithm speedup and the accuracy of the solution. Selecting an average cluster size which can generate clusters in order of 20 to 100 buses illustrates faster convergence and higher accuracy. The best performing cluster combination of each network is selected to analyze the performance.

5.4.2.1 Centralized versus DP-SCOPF for Offline Optimization

For the offline optimization, the base case is solved within 40 minutes and each contingency is solved within 2 seconds. The optimization results obtained under normal and contingency operations with Centralized and DP-SCOPF method are given in Table 5.2. According to the Table 5.2, the DP-SCOPF method provides more accurate results (lower combined metric c and related metrics) for networks 2 and 3 under normal operation. The network 1 provides lower combined metric c with the Centralized approach under normal operation. However, the DP-SCOPF method provides better results for all three networks under contingency operations. This illustrates that the DP-SCOPF

Table 5.2: ONLINE AND OFFLINE OPTIMIZATION PERFORMANCE

Parameters				Network		
				1	2	3
no of clusters				5	20	50
no of contingencies				386	91	3161
Offline	Centralized	Base case	c_g	2.6988e+04	2.2785e+04	5.1657e+05
			$\sigma_i^P[min,max]$	[-9.07e-06,2.87e-05]	[-2.48e-01, 9.54e-02]	[-1.28e+00,1.39e-01]
			$\sigma_i^Q[min,max]$	[-2.78e-05,1.17e-04]	[-1.81e-01, 1.49e-02]	[-3.75e+00, 2.51e+00]
			violated lines	0	0	0
			c^σ	3.850e+01	7.7071e+05	3.4370e+09
			c	**2.7007e+04**	4.0717e+05	3.6882e+09
		Contingencies	$c_g[mean \pm std]$	2.66e+04± 1.61e+03	2.30e+04±3.58e+02	5.15e+05±5.24e+03
			$\sigma_i^P[min,max]$	[-1.38e+00,6.43e-01]	[-1.62e+00,1.31e+00]	[-4.30e+00,2.52e+00]
			$\sigma_i^Q[min,max]$	[-5.39e+00,4.09e+01]	[2.60e+00,-2.83e+00]	[-2.48e+01,2.43e+01]
			violated lines $[mean \pm std]$	0±0	1.00e+00±0	2.99e+00±3.08e-02
			$c_k^\sigma[mean \pm std]$	5.75e+08±1.36e+08	2.70e+09±4.49e+07	7.21e+09±3.02e+08
			c	2.8752e+08	1.3504e+09	4.9554e+09
	DP-SCOPF	Base case	c_g	3.6030e+04	2.2473e+04	5.3276e+05
			$\sigma_i^P[min,max]$	[-3.98e-08, 6.39e-08]	[-1.36e-01, 5.68e-02]	[-2.68e-11, 8.37e-11]
			$\sigma_i^Q[min,max]$	[-2.51e-07, 1.84e-13]	[-4.70e-02, 3.98e-02]	[-1.76e-13, 5.16e-10]
			violated lines	0	0	0
			c^σ	5.8930e-01	4.1809e+05	9.0636e+04
			c	3.6030e+04	**2.3151e+05**	**5.7807e+05**
		Contingencies	$c_g[mean \pm std]$	3.55e+04±1.86e+03	2.24e+04±2.54e+02	5.31e+05±5.80e+03
			$\sigma_i^P[min,max]$	[-6.59e-01,3.52e-01]	[-1.26e+00,4.67e-01]	[-9.50e-01,2.04e+00]
			$\sigma_i^Q[min,max]$	[-3.42e+00,7.36e-01]	[-1.16e+00,4.69e-02]	[-7.89e+00,6.24e-11]
			violated lines$[mean \pm std]$	0±0	1.00e+00±0	1.99e+00±1.02e-01
			$c_k^\sigma[mean \pm std]$	7.26e+06±4.17e+07	2.51e+06±7.76e+07	1.17e+07±1.17e+08
			c	**3.6660e+06**	**1.4865e+06**	**6.4280+e06**
Online	Centralized	Base case	c_g	2.5918e+04	2.2231e+04	5.1423e+05
			$\sigma_i^P[min,max]$	[-4.70+e-03,5.80e-03]	[-9.98e-01,5.18e-01]	[-1.19e+00,1.39e-01]
			$\sigma_i^Q[min,max]$	[-9.08e-02,8.98e-04]	[-4.41e+00,4.62e+00]	[-3.75e+00, 2.51e+00]
			violated lines	0	0	3
			c^σ	1.0296e+05	7.0971e+09	7.3240e+09
			c	7.74e+04	3.5486e+09	3.6625e+09
		Contingencies	$c_g[mean \pm std]$	2.55e+04±1.46e+03	2.23e+04±2.81e+02	5.12e+05±5.17e+03
			$\sigma_i^P[min,max]$	[-1.24e+00,8.36e-01]	[-4.41e+00,4.62e+00]	[-4.30e+00,2.52e+00]
			$\sigma_i^Q[min,max]$	[-6.12e+00,5.11e-01]	[-3.80e+00, 8.28e-01]	[-2.48e+01,2.43e+01]
			violated lines $[mean \pm std]$	0±0	19±0	2.99e+00±3.08e-02
			$c_k^\sigma[mean \pm std]$	6.68e+08±1.34e+08	6.95e+09±5.87e+07	7.21e+09±3.02e+08
			c	3.3407e+08	7.0236e+09	7.2675e+09
	DP-SCOPF	Base case	c_g	3.6030e+04	2.2879e+04	5.3276e+05
			$\sigma_i^P[min,max]$	[-1.51e-05, 2.32e-05]	[-2.03e-01, 3.88e-02]	[-0.30e-03, 2.20e-03]
			$\sigma_i^Q[min,max]$	[-9.34e-05, 1.91e-13]	[-1.08e-01, 2.49e-01]	[- -1.11e-01, 1.35e-13]
			violated lines	0	0	0
			c^σ	2.1085e+02	1.2767e+06	4.8546e+05
			c	**3.6135e+04**	**6.6122e+05**	**7.7549e+05**
		Contingencies	$c_g[mean \pm std]$	3.55e+04± 1.86e+03	2.29e+04±1.81e+02	5.28e+05±5.98e+03
			$\sigma_i^P[min,max]$	[-6.50e-01,3.5e-01]	[-5.20e-01,3.62e-01]	[-1.01e+00,1.87e+00]
			$\sigma_i^Q[min,max]$	[-3.42e+00,6.45e-01]	[-1.09e+00,2.77e-01]	[-7.57e+00,4.97e+00]
			violated lines$[mean \pm std]$	0±0	1.01e+00±1.04e-01	1.00e+00±8.53e-02
			$c_k^\sigma[mean \pm std]$	6.69e+06±4.06e+07	3.88e+06±1.87e+07	3.15e+07±1.32e+08
			c	**3.3811e+06**	**2.6012e+06**	**1.6525e+07**

can solve contingencies with higher accuracy and the method performance is increased with the size of the network.

5.4.2.2   Centralized versus DP-SCOPF for Online Optimization

The base case is solved within 600 seconds and each contingency is solved within 2 seconds during the online optimization. Solving the problem for online case is more challenging compared to offline case. According to the Table 5.2, DP-SCOPF is capable of providing more accurate solutions for online optimization compared to the Centralized approach for all three networks. Lower combined metric c, soft constraint violation penalties (σ_i^P, σ_i^Q), and violated lines are observed with DP-SCOPF method. This demonstrates that the DP-SCOPF problem provides accurate results within a short time period, which is unable to achieve using traditional Centralized approach. The DP-SCOPF method provides improved results when the network size is increased.

5.5   Summary

In this study, a distributed and parallel security constrained optimal power flow (DP-SCOPF) algorithm is proposed to solve the SCOPF problem based upon a non-convex formulation. To enable the distributed and parallel properties, the network is clustered into multiple regions by considering the dependencies between the clusters. The clusters are created with the application of graph theory-based spectral clustering algorithm. The method can provide improved solutions for the online and offline optimization scenarios. Highly improved performance is observed for the networks with increased number of buses. Additionally, the method is capable of solving N-1 contingency scenarios with accepted level of accuracy and computation time, where the centralized approach is not capable of solving contingencies within the limited time period for larger networks.

Chapter 6

Conclusion

6.1 Introduction

Modern power system operation is susceptible to risks from both natural and human disruptions and attacks. Increasing integration of renewable energy sources such as solar and wind power into the electric power grid introduces additional challenges for real-time power system operation and control due to variability and uncertainty in generation. Moreover, extreme events such as natural disasters, unprecedented outages, and cyber-attacks introduce challenges in maintaining resilience of the power system.

6.2 Section Summaries

In this dissertation, solutions are presented to enhance two main system control center applications, automatic generation control (AGC) and security constrained optimal power flow (SCOPF). The methods improve the resilience of the smart grid under high penetration levels of variable PV power, cyber-attacks and unprecedented outages.

6.2.1 Optimal Automatic Generation Control (AGC)

AGC plays a vital role in maintaining frequency regulations of the power system, which needs to be effectively handled when there are uncertain and unexpected disturbances in the system. Multiple studied have carried out to obtain optimal AGC parameters for the conventional AGC,

including sequential, two-step tuning and distributed tuning approaches. The methods are tested on two multi-area power system with large integration of photovoltaic power (PV). The distributed approach enhanced the performance in all the inter-connected areas, hence improved overall power system performance.

6.2.2 Situational Intelligence for Smart Grid Resilience

Situational intelligence is the integration of historical and real-time data to implement near-future situational awareness. Predictive analytics plays an important role in smart grid. Accurate predictions of system dynamics can overcome the challenges presented by variability of PV power generation. Three PV power prediction models and a distributed solar irradiance prediction model for spatially and temporally distributed PV plants are developed with the application of artificial intelligence methods. Cellular computational based power system bus frequency prediction model is presented for predicting bus frequency in uncertain and variable PV power generation conditions. This is developed using a virtual synchrophasor network (VSN). It is shown that the prediction models provide better accuracy in predicting PV power and bus frequencies compared to state of-art persistence model. The prediction models are capable of providing multi-time step predictions with minimum computational complexity.

6.2.3 Resilient and Sustainable Tie-line Bias Control for a Power System in Uncertain Environments

An enhanced tie-line bias control method is proposed for a power system in uncertain environments by exploiting predictions. Predictions are introduced to overcome the response time of the AGC and governors of the system. Application of the prediction models in AGC operation provides enhanced tie-line bias control for different weather and load conditions. Furthermore, the VSN is capable of mitigating impact(s) of denial of service attacks on physical PMUs. The tie-line bias control performance is measured using NERC defined standard performance metrics (CPS1 and CPS2) and related metrics, which indicate this method can minimize the penalties introduced by NERC for maintaining steady state interconnection frequency.

6.2.4 Distributed and Parallel Security-Constrained Optimal Power Flow

A distributed and parallel security constrained optimal power flow (DP-SCOPF) algorithm is proposed to solve the SCOPF problem based upon a non-convex formulation. To enable the distributed and parallel properties, the power network is clustered into multiple regions by considering the dependencies between the clusters. The proposed method can provide improved solutions for the online and offline optimization scenarios. Highly improved performance is observed with the increased number of buses. Additionally, the method is capable of solving N-1 contingency scenarios with accepted level of accuracy and computation time, where the Centralized approach is not capable of solving contingencies within the limited time period for larger networks.

6.2.5 Impact of the Contributions

Optimal AGC results in proper power transfer between control areas with regulated system frequency. It is important to have SI for resilient operation and control of the power system under unexpected disruptions and attacks. The proposed prediction models provide situational intelligence for variable generations, variable loads and DoS attacks. The proposed tie-line bias control approach allow increased penetration of PV power in the power system. The control area reliability is increased by reducing penalties introduced by North American Electric Cooperation (NERC). The faster SCOPF problem solving approach can perform efficient online operation and offline planning of cost effective power dispatch. Overall, the contributions of this dissertation enhances smart grid operation resilience under high penetration levels of variable energy and cyber-physical disturbances.

6.3 Future Work

Following topics can be further investigated to provide additional improvements.

- Improve prediction model performance by expanding the input parameters of reservoir learning based networks to have cloud cover and relative humidity measures.

- Develop the CCN framework with the utilization of distributed and parallel computing capabilities.

- Analyze DoS attacks on both physical and virtual PMUs and developing mitigation strategies to address the challenges in DoS attacks in power systems.

- Improve the DP-SCOPF by determining a proper mechanism to decide the number of clusters and solve large power systems.

6.4   Summary

In this dissertation, an optimal AGC operation is achieved with a cellular parameter tuning method. The smart grid SI is strengthened by introducing accurate and efficient short term solar irradiance, PV power and Bus frequency prediction models. The prediction models are integrated to obtain enhanced tie-line bias control in uncertain environments. A distributed and parallel SCOPF (DP-SCOPF) method is introduced to obtain faster solutions to online operation and offline planning in control centers. Overall the contributions facilitates a resilient smart grid operation.

Appendices

Appendix A   Optimal Automatic Generation Control (AGC)

Table A.1: ACE PERFORMANCE ANALYSIS FOR SEQUENTIAL TUNING

		Area				
		1	2	3	4	5
Maximum Overshoot (MW)	Stage 1	179	102	53	-13	241
	Stage 2	181	102	24	39	240
	Stage 3	182	103	26	51	240
	Stage 4	179	102	27	54	240
	Stage 5	177	101	26	57	239
	Stage 6	168	101	26	55	237
Maximum Undershoot (MW)	Stage 1	-26	-38	-101	-215	-1
	Stage 2	-30	-40	-95	-207	-43
	Stage 3	-47	-41	-92	-209	-63
	Stage 4	-34	-39	-89	-208	-47
	Stage 5	-37	-33	-89	-208	-50
	Stage 6	-80	-35	-90	-207	-56
Settling Time (s)	Stage 1	30.17	39.97	203.4	66.08	65.64
	Stage 2	26.30	39.69	48.31	29.04	35.54
	Stage 3	38.32	40.09	56.35	37.15	56.98
	Stage 4	31.31	38.00	43.81	43.96	52.78
	Stage 5	35.94	40.22	44.21	44.29	52.31
	Stage 6	29.99	39.59	45.49	43.78	52.96

Table A.2: AGC PARAMETERS -INITIAL AND FINAL STAGES FOR SEQUENTIAL TUNING

		AGC Parameters	
		K_p	K_i
AGC-1	Stage 1	0.4847	1.3451
	Stage 6	0.0446	1.2577
AGC-2	Stage 1	0.0100	0.5215
	Stage 6	0.0182	0.6418
AGC-3	Stage 1	0.7651	1.7598
	Stage 6	0.4525	0.2488
AGC-4	Stage 1	1.7383	1.1820
	Stage 6	0.4525	0.2488
AGC-5	Stage 1	0.4987	1.8119
	Stage 6	0.4889	0.2914
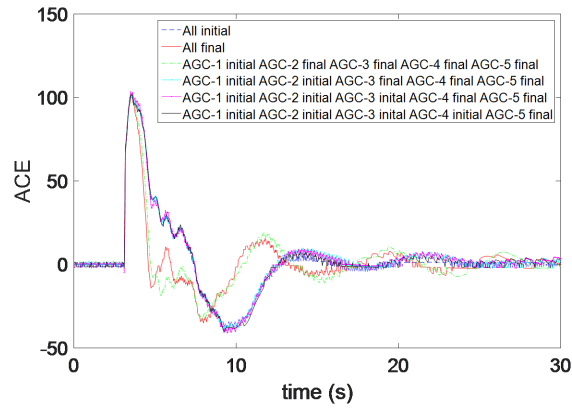
Figure A.1: AGC-3 response with initial and tuned parameters for 200 MW load increase at the Bus 42(Area 3).
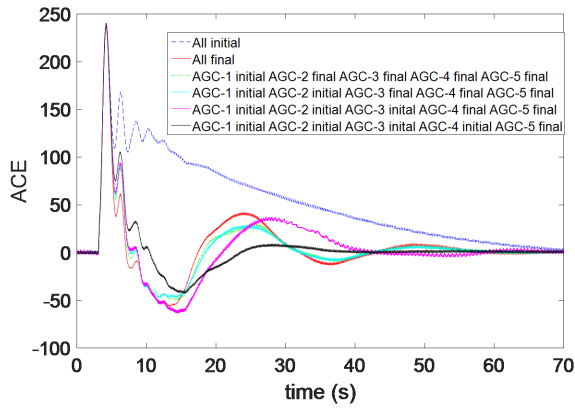
Figure A.2: AGC-4 response with initial and tuned parameters for 200 MW load increase at the Bus 52 (Area 4).
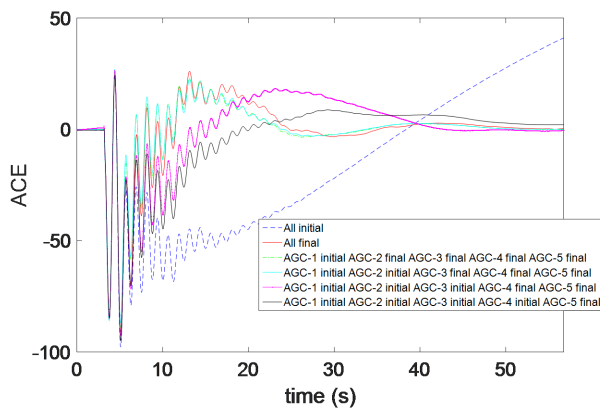
Figure A.3: AGC-5 response with initial and tuned parameters for 200 MW load increase at the Bus 52 (Area 5).

Appendix B   Resilient and Sustainable Tie-line Bias Control for a Power System in Uncertain Environments
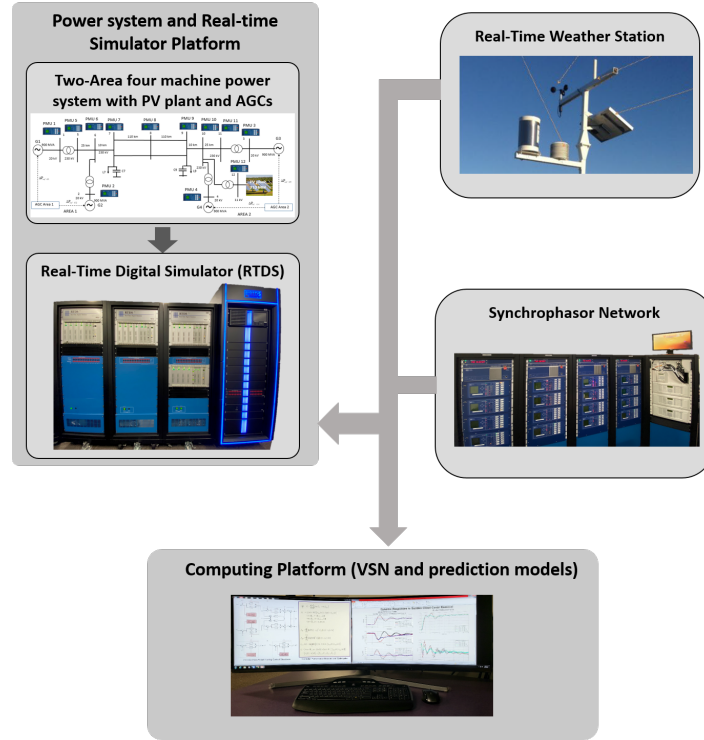
Figure B.1: Experimental setup for tie-line bias control study.

$$\Delta\omega \longrightarrow \boxed{K_{pss} \left(\frac{sT_{Wss}}{1+sT_{Wss}}\right)\left(\frac{1+sT_{pss1}}{1+sT_{pss2}}\right)\left(\frac{1+sT_{pss3}}{1+sT_{pss4}}\right)} \longrightarrow V_{pss}$$

Figure B.2: Power System Stabilizer (PSS).

Table B.1: AGC PARAMETERS.

	λ_R	T (s)	k	α_1	α_2
AGC-1	-20	0.5	0.007	0.5	0.5
AGC-2	-20	0.5	0.007	0.5	0.5

Appendix C   Security-Constrained Optimal Power Flow (SCOPF)

C.1   Power Flow Equations Related to (5.1)

$$p_e^o = g_e v_{i_e^o}{}^2 + (-g_e cos(\theta_{i_e^o} - \theta_{i_e^d}) - b_e sin(\theta_{i_e^o} - \theta_{i_e^d}))v_{i_e^o}v_{i_e^d} \quad \forall e \in E, \tag{1}$$

$$p_e^d = g_e v_{i_e^d}{}^2 + (-g_e cos(\theta_{i_e^d} - \theta_{i_e^o}) - b_e sin(\theta_{i_e^d} - \theta_{i_e^o}))v_{i_e^o}v_{i_e^d} \quad \forall e \in E, \tag{2}$$

$$p_f^o = (g_f/\tau_f^2 + g_f^M)v_{i_f^o}{}^2 + (-g_f/\tau_f cos(\theta_{i_f^o} - \theta_{i_f^d} - \theta_f) - \frac{b_f}{\tau_f} sin(\theta_{i_f^o} - \theta_{i_f^d} - \theta_f))v_{i_f^o}v_{i_f^d} \quad \forall f \in F, \tag{3}$$

$$p_f^d = (g_f)v_{i_f^d}{}^2 + (-g_f/\tau_f cos(\theta_{i_f^d} - \theta_{i_f^o} + \theta_f) - \frac{b_f}{\tau_f} sin(\theta_{i_f^d} - \theta_{i_f^o} - \theta_f))v_{i_f^o}v_{i_f^d} \quad \forall f \in F, \tag{4}$$

$$q_e^o = -(b_e + \frac{b_e^{CH}}{2})v_{i_e^o}{}^2 + (b_e cos(\theta_{i_e^o} - \theta_{i_e^d}) - g_e sin(\theta_{i_e^o} - \theta_{i_e^d}))v_{i_e^o}v_{i_e^d} \quad \forall e \in E, \tag{5}$$

$$q_e^d = -(b_e + \frac{b_e^{CH}}{2})v_{i_e^d}{}^2 + (b_e cos(\theta_{i_e^d} - \theta_{i_e^o}) - g_e sin(\theta_{i_e^d} - \theta_{i_e^o}))v_{i_e^o}v_{i_e^d} \quad \forall e \in E, \tag{6}$$

$$q_f^o = (b_f/\tau_f^2 + b_f^M)v_{i_f^o}{}^2 + (-b_f/\tau_f cos(\theta_{i_f^o} - \theta_{i_f^d} - \theta_f) - \frac{g_f}{\tau_f} sin(\theta_{i_f^o} - \theta_{i_f^d} - \theta_f))v_{i_f^o}v_{i_f^d} \quad \forall f \in F, \tag{7}$$

$$q_f^d = (b_f)v_{i_f^d}{}^2 + (-b_f/\tau_f cos(\theta_{i_f^d} - \theta_{i_f^o} + \theta_f) - \frac{g_f}{\tau_f} sin(\theta_{i_f^d} - \theta_{i_f^o} - \theta_f))v_{i_f^o}v_{i_f^d} \quad \forall f \in F, \tag{8}$$

Bibliography

[1] I. Jayawardene, Y. Wei, and G. K. Venayagamoorthy, "Optimized automatic generation control in a multi-area power system with particle swarm optimization," in *2017 IEEE Symposium Series on Computational Intelligence (SSCI)*, pp. 1–8, 2017.

[2] Y. Wei, I. Jayawardene, and G. K. Venayagamoorthy, "Optimal automatic generation controllers in a multi-area interconnected power system with utility-scale pv plants," *IET Smart Grid*, vol. 2, no. 4, pp. 581–593, 2019.

[3] I. Jayawardene and G. K. Venayagamoorthy, "Tuning of automatic generation control for enhanced power system operation," *SAIEE Africa Research Journal*, 2020. submitted to.

[4] I. Jayawardene, R. V. Kulkarni, and G. K. Venayagamoorthy, "Ci-based analytics for photovoltaic power predictions and tie-line bias control in smart grid," in *2018 IEEE Symposium Series on Computational Intelligence (SSCI)*, pp. 1626–1633, 2018.

[5] I. Jayawardene and G. K. Venayagamoorthy, "Comparison of echo state network and extreme learning machine for pv power prediction," in *2014 IEEE Symposium on Computational Intelligence Applications in Smart Grid (CIASG)*, pp. 1–8, 2014.

[6] I. Jayawardene and G. K. Venayagamoorthy, "Comparison of adaptive neuro-fuzzy inference systems and echo state networks for pv power prediction," *Procedia Computer Science*, vol. 53, pp. 92 – 102, 2015. INNS Conference on Big Data 2015 Program San Francisco, CA, USA 8-10 August 2015.

[7] I. Jayawardene and G. K. Venayagamoorthy, "Spatial predictions of solar irradiance for photovoltaic plants," in *2016 IEEE 43rd Photovoltaic Specialists Conference (PVSC)*, pp. 0267–0272, 2016.

[8] I. Jayawardene and G. K. Venayagamoorthy, "Cellular computational extreme learning machine network based frequency predictions in a power system," in *2017 International Joint Conference on Neural Networks (IJCNN)*, pp. 3377–3384, 2017.

[9] I. Jayawardene and G. K. Venayagamoorthy, "Reservoir based learning network for control of two-area power system with variable renewable generation," *Neurocomputing*, vol. 170, pp. 428 – 438, 2015.

[10] I. Jayawardene and G. K. Venayagamoorthy, "Resilient and sustainable tie-line bias control for a power system in uncertain environments," *IEEE Transactions on Emerging Topics in Computational Intelligence*, 2020.

[11] I. Jayawardene, P. Herath, and G. K. Venayagamoorthy, "A graph theory based clustering method for power system networks," in *Clemson Power System Conference (PSC) 2020*, 2020. Submitted.

[12] I. Jayawardene, P. Herath, and G. K. Venayagamoorthy, "A distributed and parallel approach based on clustering for security-constrained optimal power flow problem," *IEEE transactions on Industrial Engineering*, 2020. submitted to.

[13] G. K. Venayagamoorthy, ""situational awareness / situational intelligence system and method for analyzing, monitoring, predicting and controlling electric power systems," 2014. Clemson Patents. 584.

[14] B. Luitel and G. K. Venayagamoorthy, "Decentralized asynchronous learning in cellular neural networks," *IEEE Transactions on Neural Networks and Learning Systems*, pp. 1755–1766, 2012.

[15] Cybersecurity and Infrastructure Security Agency, "Critical Infrastructure Sectors." `https://www.cisa.gov/critical-infrastructure-sectors`. [Last visited: 10-November-2020].

[16] H. Noorazar, A. k. Srivastava, K. S. Sajan, and S. Pannala, "Data-driven operation of the resilient electric grid: A case of covid-19," 2020.

[17] B. L. Preston, S. N. Backhaus, M. Ewers, J. A. P. C. A. Silva-Monroy, J. E. Dagle, A. G. Tarditi, J. P. Looney, and J. Thomas J. King, "Resilience of the u.s. electricity system:a multi-hazard perspective," 2016.

[18] H. Chen, F. S. Bresler, M. E. Bryson, K. Seiler, and J. Monken, "Toward bulk power system resilience: Approaches for regional transmission operators," *IEEE Power and Energy Magazine*, vol. 18, no. 4, pp. 20–30, 2020.

[19] Y. Lin, Z. Bie, and A. Qiu, "A review of key strategies in realizing power system resilience," *Global Energy Interconnection*, vol. 1, no. 1, pp. 70 – 78, 2018.

[20] Z. Bie, Y. Lin, G. Li, and F. Li, "Battling the extreme: A study on the power system resilience," *Proceedings of the IEEE*, vol. 105, no. 7, pp. 1253–1266, 2017.

[21] Wanter Uja, "The Effects of Natural Disasters on Energy Infrastructure ." `https://law.lclark.edu/live/blogs/132-the-effects-of-natural-disasters-on-energy`. [Last visited: 10-November-2020].

[22] Rod Walton, "13 Years After: The Northeast Blackout of 2003 Changed Grid Industry, Still Causes Fear for Future ." `https://www.power-grid.com/2016/08/23/13-years-after-the-northeast-black-of-2003-changed-grid-industry-still-causes\protect\leavevmode@ifvmode\kern+.2777em\relax-fear-for-future/#gref`. [Last visited: 10-November-2020].

[23] Ilaria Grasso Macola, "The five worst cyber-attacks against the power industry since 2014." `https://www.power-technology.com/features/the-five-worst-cyberattacks-against-the-power-industry-since2014/`. [Last visited: 10-November-2020].

[24] A. Alireza, D.Meysam, and A. Farrokh, "Power system flexibility: an overview of emergence to evolution," *Journal of Modern Power Systems and Clean Energy*, vol. 7, pp. 987–1007, 2019.

[25] S. R. Sinsel, R. L. Riemke, and V. H. Hoffmann, "Challenges and solution technologies for the integration of variable renewable energy sources—a review," *Renewable Energy*, vol. 145, pp. 2271 – 2285, 2020.

[26] Solar Energy Industries Association: SEIA, "Solar Industry Research Data:Solar Industry Growing at a Record Pace."

[27] O. of ENERGY EFFICIENCY RENEWABLE ENERGY, "Solar Energy in the United States."

[28] Pacific Northwest National Laboratory, "Integrating Renewable Generation into Grid Operations: Four International Experiences ."

[29] M. M. L. Bird and D. Lew, "Integrating Variable Renewable Energy: Challenges and Solutions, National Renewable Energy Laboratory ."

[30] K. Schaber, F. Steinke, P. Mühlich, and T. Hamacher, "Parametric study of variable renewable energy integration in europe: Advantages and costs of transmission grid extensions," *Energy Policy*, vol. 42, pp. 498 – 508, 2012.

[31] NERC, "Frequency response and bias," 2019.

[32] C.Chen, K.Zhang, K.Yuan, and X.Teng, "Tie-line bias control applicability to load frequency control for multi-area interconnected power systems of complex topology," *Energies*, vol. 10, 2017.

[33] "Load frequency controllers considering renewable energy integration in power system," *Energy Reports*, vol. 5, pp. 436 – 453, 2019.

[34] K. Morison, Lei Wang, and P. Kundur, "Power system security assessment," *IEEE Power and Energy Magazine*, vol. 2, no. 5, pp. 30–39, 2004.

[35] "Synchrophasor technology and renewables integration: Naspi technical workshop," tech. rep., Department of Energy, 07 2014.

[36] X. Zhong, I. Jayawardene, G. K. Venayagamoorthy, and R. Brooks, "Denial of service attack on tie-line bias control in a power system with pv plant," *IEEE Transactions on Emerging Topics in Computational Intelligence*, vol. 1, no. 5, pp. 375–390, 2017.

[37] A. Monticelli, M. V. F. Pereira, and S. Granville, "Security-constrained optimal power flow with post-contingency corrective rescheduling," *IEEE Transactions on Power Systems*, vol. 2, no. 1, pp. 175–180, 1987.

[38] PNNL, "SCOPF Problem Formulation: Challenge 1: Grid Optimization Competition."

[39] "Strong np-hardness of ac power flows feasibility," *Operations Research Letters*, vol. 47, no. 6, pp. 494 – 501, 2019.

[40] M. Sacasqui and J. Luyo, "Automatic generation control of an equivalent multi-source electric power system using the decentralized nepsac controller," in *2018 IEEE International Conference on Automation/XXIII Congress of the Chilean Association of Automatic Control (ICA-ACCA)*, pp. 1–4, 2018.

[41] P. Arunagirinathan, Y. Wei, A. Arzani, and G. K. Venayagamoorthy, "Wide-area situational awareness based power system stabilizer tuning with utility scale pv integration," in *2018 Clemson University Power Systems Conference (PSC)*, pp. 1–8, 2018.

[42] Y. Wei, Lvying, Z. Yu, J. Hou, and G. K. Venayagamoorthy, "Agc asynchronous tuning for improving pv consumption in the energy imbalance market," in *2020 Clemson University Power Systems Conference (PSC)*, pp. 1–5, 2020.

[43] E. Ali, "Journal of king saud university - engineering sciences," *IEEE Transactions on Emerging Topics in Computational Intelligence*, vol. 11, no. 1, pp. 49–69, 1999.

[44] H. Luo, Z. Hu, H. Zhang, and H. Chen, "Coordinated active power control strategy for de-loaded wind turbines to improve regulation performance in agc," *IEEE Transactions on Power Systems*, vol. 34, no. 1, pp. 98–108, 2019.

[45] Y. Arya, "Agc performance enrichment of multi-source hydrothermal gas power systems using new optimized fofpid controller and redox flow batteries," *Energy*, vol. 127, pp. 704 – 715, 2017.

[46] Y. Arya and N. Kumar, "Optimal agc with redox flow batteries in multi-area restructured power systems," *Engineering Science and Technology, an International Journal*, vol. 19, no. 3, pp. 1145 – 1159, 2016.

[47] M. Pant, R. Thangaraj, and A. Abraham, *Particle Swarm Optimization: Performance Tuning and Empirical Analysis*, pp. 101–128. Berlin, Heidelberg: Springer Berlin Heidelberg, 2009.

[48] B. C. Bikash Pal, *Robust Control in Power Systems*, pp. XXVI, 190. Springer US, 2005.

[49] H. Yuan, R. S. Biswas1, J. Tan, Y, and Zhang, "Developing a reduced 240-bus wecc dynamic model for frequency response study of high renewable integration," pp. 1–8, 2019.

[50] "Smartgrid.gov," 2020.

[51] K. Ahn and D. Truong, "Online tuning fuzzy pid controller using robust extended kalman filter," *Journal of Process Control*, vol. 19, no. 6, pp. 1011–1023, 2016.

[52] A. Reisizadeh, A. Mokhtari, H. Hassani, and R. Pedarsani, "An exact quantized decentralized gradient descent algorithm," *IEEE Transactions on Signal Processing*, vol. 67, no. 19, pp. 4934–4947, 2009.

[53] "Compressed distributed gradient descent: Communication-efficient consensus over networks."

[54] B. Luitel and G. K. Venayagamoorthy, "Cellular computational networks—a scalable architecture for learning the dynamics of large networked systems," *Neural Networks*, vol. 50, pp. 120 – 123, 2014.

[55] Y. Wei, I. Jayawardene, and G. K. Venayagamoorthy, "Frequency prediction of synchronous generators in a multi-machine power system with a photovoltaic plant using a cellular computational network," in *2015 IEEE Symposium Series on Computational Intelligence*, pp. 673–678, 2015.

[56] C. Pathiravasam and G. K. Venayagamorthy, "Spatio-temporal characteristics based wind speed predictions," in *2016 IEEE International Conference on Information and Automation for Sustainability (ICIAfS)*, pp. 1–6, 2016.

[57] Y. Wei and G. K. Venayagamoorthy, "Cellular computational generalized neuron network for frequency situational intelligence in a multi-machine power system," *Neural Networks*, vol. 93, pp. 21 – 35, 2017.

[58] C. Godsil and G. Royle, *Algebraic Graph Theory: 207*. New York: Springer-Ver-lag, 2001.

[59] G. Tanaka, T. Yamane, J. B. Héroux, R. Nakane, N. Kanazawa, S. Takeda, H. Numata, D. Nakano, and A. Hirose, "Recent advances in physical reservoir computing: A review," *CoRR*, vol. abs/1808.04962, 2018.

[60] Guang-BinHuang, Qin-YuZhu, and Chee-KheongSiew, "Extreme learning machine: Theory and applications," *Neurocomputing*, vol. 70, no. 1, pp. 489 – 501, 2006. Neural Networks.

[61] Y. Ye, S. Squartini, and F. Piazza, "Online sequential extreme learning machine in nonstationary environments," *Neurocomputing*, vol. 116, pp. 94 – 101, 2013. Advanced Theory and Methodology in Intelligent Computing.

[62] H. Jaeger, "The echo state approach to analysing and training recurrent neural networks," GMD Report 148, GMD - German National Research Institute for Computer Science, 2001a.

[63] H. Jaeger, "Adaptive nonlinear system identification with echo state networks," in *Proceedings of the 15th International Conference on Neural Information Processing Systems*, NIPS'02, (Cambridge, MA, USA), p. 609–616, MIT Press, 2002.

[64] R. Ak, O. Fink, and E. Zio, "Two machine learning approaches for short-term wind speed time-series prediction," *IEEE Transactions on Neural Networks and Learning Systems*, vol. 27, no. 8, pp. 1734–1747, 2016.

[65] F. Rodríguez, A. Fleetwood, A. Galarza, and L. Fontán, "Predicting solar energy generation through artificial neural networks using weather forecasts for microgrid control," *Renewable Energy*, vol. 126, pp. 855 – 864, 2018.

[66] P.Bacher, H.Madsen, and H.Nielsen, "Online short-term solar power forecasting," *Solar Energy*, vol. 83, no. 10, pp. 1772 – 1783, 2009.

[67] A. Kusiak, H. Zheng, and Z. Song, "Short-term prediction of wind farm power: A data mining approach," *IEEE Transactions on Energy Conversion*, vol. 24, no. 1, pp. 125–136, 2009.

[68] A.Foley, P.Leahy, A.Marvuglia, and E.McKeogh, "Current methods and advances in forecasting of wind power generation," *Renewable Energy*, vol. 37, no. 1, pp. 1 – 8, 2012.

[69] A. Dobbs, T.Elgindy, B.Hodge, and A. Florita, "Short-term solar forecasting performance of popular machine learning algorithms," in *National Renewable Energy Laboratory (NREL), International Workshop on the Integration of Solar Power into Power Systems (Solar Integration Workshop), Berlin, Germany*, 2017.

[70] NREL, "Oahu solar measurement grid," 2019.

[71] C. Gallicchio, A. Micheli, and L. Pedrelli, "Comparison between DeepESNs and gated RNNs on multivariate time-series prediction," *arXiv e-prints*, p. arXiv:1812.11527, Dec. 2018.

[72] J. Dong, X. Ma, S. M. Djouadi, H. Li, and Y. Liu, "Frequency prediction of power systems in fnet based on state-space approach and uncertain basis functions," *IEEE Transactions on Power Systems*, vol. 29, no. 6, pp. 2602–2612, 2014.

[73] A. Routray, A. K. Pradhan, and K. P. Rao, "A novel kalman filter for frequency estimation of distorted signals in power systems," *IEEE Transactions on Instrumentation and Measurement*, vol. 51, no. 3, pp. 469–479, 2002.

[74] V. V. Terzija, M. B. Djuric, and B. D. Kovacevic, "Voltage phasor and local system frequency estimation using newton type algorithm," *IEEE Transactions on Power Delivery*, vol. 9, no. 3, pp. 1368–1374, 1994.

[75] L. L. Lai, W. L. Chan, C. T. Tse, and A. T. P. So, "Real-time frequency and harmonic evaluation using artificial neural networks," *IEEE Transactions on Power Delivery*, vol. 14, no. 1, pp. 52–59, 1999.

[76] Q. Bo, X. Wang, and K. Liu, "Minimum frequency prediction of power system after disturbance based on the v-support vector regression," in *2014 International Conference on Power System Technology*, pp. 614–619, 2014.

[77] Y. Wei and G. K. Venayagamoorthy, "A lite cellular generalized neuron network for frequency prediction of synchronous generators in a multimachine power system," in *2016 International Joint Conference on Neural Networks (IJCNN)*, pp. 3085–3092, 2016.

[78] H. Bevrani and T. Hiyama, *Intelligent Automatic Generation Control*. CRC Press, 2017.

[79] National Renewable Energy Laboratory (NREL), "GRID-FRIENDLY RENEWABLE EN-ERGY : Solar and Wind Participation in Automatic Generation Control Systems." `https://www.nrel.gov/docs/fy19osti/73866.pdf`. [Last visited: 25-June-2020].

[80] X. Zhang, Z. Xu, T. Yu, B. Yang, and H. Wang, "Optimal mileage based agc dispatch of a genco," *IEEE Transactions on Power Systems*, vol. 35, no. 4, pp. 2516–2526, 2020.

[81] L. Yin, S. Li, and H. Liu, "Lazy reinforcement learning for real-time generation control of parallel cyber–physical–social energy systems," *Engineering Applications of Artificial Intelligence*, vol. 88, p. 103380, 2020.

[82] X. Zhao, Z. Lin, B. Fu, L. He, and C. Li, "Research on the predictive optimal pid plus second order derivative method for agc of power system with high penetration of photovoltaic and wind power," *Journal of Electrical Engineering and Technology*, vol. 14, p. 1075–1086, 2019.

[83] H. Luo, Z. Hu, H. Zhang, and H. Chen, "Coordinated active power control strategy for deloaded wind turbines to improve regulation performance in agc," *IEEE Transactions on Power Systems*, vol. 34, no. 1, pp. 98–108, 2019.

[84] S. Alhalali, C. Nielsen, and R. El-Shatshat, "Mitigation of cyber-physical attacks in multi-area automatic generation control," *International Journal of Electrical Power and Energy Systems*, vol. 112, pp. 362 – 369, 2019.

[85] A. Arzani and G. K. Venayagamoorthy, "Computational approach to enhance performance of photovoltaic system inverters interfaced to utility grids," *IET Renewable Power Generation*, vol. 12, no. 1, pp. 112–124, 2018.

[86] "IEEE standard for synchrophasor data transfer for power systems," *IEEE Std C37.118.2-2011*, pp. 1–53, 2011.

[87] Wang Zhang, Yan Xu, Zhao Yang Dong, Yijia Wang, and Rui Zhang, "An efficient approach for robust scopf considering load and renewable power uncertainties," in *2016 Power Systems Computation Conference (PSCC)*, pp. 1–7, 2016.

[88] J. Mohammadi, G. Hug, and S. Kar, "Agent-based distributed security constrained optimal power flow," *IEEE Transactions on Smart Grid*, vol. 9, no. 2, pp. 1118–1130, 2018.

[89] D. Bienstock and A. Verma, "Strong np-hardness of ac power flows feasibility," *Operations Research Letters*, vol. 47, no. 6, pp. 494 – 501, 2019.

[90] O. R. Saavedra, "Solving the security constrained optimal power flow problem in a distributed computing environment," *IEE Proceedings - Generation, Transmission and Distribution*, vol. 143, no. 6, pp. 593–598, 1996.

[91] R. Madani, M. Ashraphijuo, and J. Lavaei, "Promises of conic relaxation for contingency-constrained optimal power flow problem," in *2014 52nd Annual Allerton Conference on Communication, Control, and Computing (Allerton)*, pp. 1064–1071, 2014.

[92] A. Venzke and S. Chatzivasileiadis, "Convex relaxations of security constrained ac optimal power flow under uncertainty," in *2018 Power Systems Computation Conference (PSCC)*, pp. 1–7, 2018.

[93] J. Kardoš, D. Kourounis, and O. Schenk, "Two-level parallel augmented schur complement interior-point algorithms for the solution of security constrained optimal power flow problems," *IEEE Transactions on Power Systems*, vol. 35, no. 2, pp. 1340–1350, 2020.

[94] J. Guo, G. Hug, and O. Tonguz, "Enabling distributed optimization in large-scale power systems," 05 2016.

[95] S. Mhanna, G. Verbič, and A. C. Chapman, "Adaptive admm for distributed ac optimal power flow," *IEEE Transactions on Power Systems*, vol. 34, no. 3, pp. 2025–2035, 2019.

[96] M. Velay, M. Vinyals, Y. Besanger, and N. Retiere, "Fully distributed security constrained optimal power flow with primary frequency control," *International Journal of Electrical Power Energy Systems*, vol. 110, pp. 536 – 547, 2019.

[97] R. S. Wibowo, T. P. Fathurrodli, O. Penangsang, and A. Soeprijanto, "Security constrained optimal power flow with facts devices using bender decomposition," in *TENCON 2014 - 2014 IEEE Region 10 Conference*, pp. 1–5, 2014.

[98] A. Monticelli, M. V. F. Pereira, and S. Granville, "Security-constrained optimal power flow with post-contingency corrective rescheduling," *IEEE Power Engineering Review*, vol. PER-7, no. 2, pp. 43–44, 1987.

[99] "Scopf problem formulation: Challenge 1: Grid optimization competition," 2019.

[100] M. Tomás-Rodríguez and S. P. Banks, *Linear Approximations to Nonlinear Dynamical Systems*, pp. 11–28. London: Springer London, 2010.

[101] J. Sun and L. Tesfatsion, "Dc optimal power flow formulation and solution using quadprogj," 04 2006.

[102] U. von Luxburg, "A tutorial on spectral clustering," *Statistics and Computing*, vol. 17, no. 4, pp. 395–416, 2007.

Iroshani Jayawardene: Iroshani is a Ph.D. candidate in Computer Engineering in the Holcombe Department of Electrical and Computer Engineering, Clemson University, Clemson, SC, USA. She received her B.Sc degree with first class honors specializing in Computer Science from University of Peradeniya, Sri Lanka in 2011. After working as a Software Engineer for three years, she joined the Real-Time Power and Intelligent Systems Laboratory as a Research Assistant. She was a Collaborative Researcher at NREL from October 2019 - March 2020. She was nominated as a finalist for best student paper award competition at IEEE 43rd PVSC, 2016. She was a recipient of the INNS Conference on Big Data student travel grant in 2015 and IEEE SSCI student travel grant in 2017. Her current research interests include smart grid, real-time power system data analytics and artificial intelligence.